ABSTRACT

EVALUATION OF PROTONS' MOST LIKELY PATHS IN INHOMOGENEOUS PHANTOMS FOR PROTON-COMPUTED TOMOGRAPHY

Kent Jiann Dar Wong, M.S.
Department of Physics
Northern Illinois University, 2009
Bela Erdelyi, Director

Proton-computed tomography (pCT) is a unique medical diagnostic tool that potentially allows us to image anatomical regions within a patient by eliminating the conversion function of Hounsfield CT Units and using the relative stopping power in proton therapy. This would subsequently remove relatively large uncertainties in the Bragg peak position, thereby more accurately locating the tumor. Furthermore, the high resolving power with less dosage and increased sparing of healthy tissues from radiation make pCT a more accurate and effective alternative to x-ray CT (xCT)-based proton therapy treatment planning.

The quality of a pCT image is largely determined by the spatial resolution and relative electron density resolution. This work explores the first aspect. The presence of multiple Coulomb scattering (MCS) physically worsens the spatial resolution and affects the ability to reconstruct the proton path. The goal of good spatial resolution is achieved by constructing the most likely path (MLP) formalism of the protons traversing through a phantom. This thesis assesses the analytical MLP, originally constructed in the case for the homogeneous water phantom, in cases for inhomogeneous phantoms consisting of air, bone, and water, and explores the use of Geant4 in simulating protons. The assessment is

done by computing and comparing how well the actual proton paths in the inhomogeneous phantoms are approximated with analytical MLP.

NORTHERN ILLINOIS UNIVERSITY
DEKALB, ILLINOIS

AUGUST 2009

EVALUATION OF PROTONS' MOST LIKELY PATHS IN INHOMOGENEOUS PHANTOMS FOR PROTON-COMPUTED TOMOGRAPHY

BY

KENT JIANN DAR WONG

A THESIS SUBMITTED TO THE GRADUATE SCHOOL

IN PARTIAL FULFILLMENT OF THE REQUIREMENTS

FOR THE DEGREE

MASTER OF SCIENCE

DEPARTMENT OF PHYSICS

Thesis Director:
Bela Erdelyi

ACKNOWLEDGEMENTS

The author would like to acknowledge and thank Professor Bela Erdelyi for his assistance and guidance in the preparation of this research and thesis paper. He would also like to thank Professor Reinhard Schulte from Loma Linda University Medical Center and University of Wollongong doctorate student Scott Penfold for providing the necessary resources and tools which made the research possible and the needed help. The author wishes to express his thanks to Professor George Coutrakon for making the pCT research collaboration between Northern Illinois University and Loma Linda possible and his participation in the thesis committee. He would like thank NIU student James Maloney for his help with the G4Beamline. Finally, he would like to express his thanks to Northern Illinois University and its Physics Department for the graduate assistantship and financial support provided to the author.

TABLE OF CONTENTS

Page

LIST OF TABLES

LIST OF FIGURES

Figure Page

Chapter 1

INTRODUCTION

Since the advent of proton therapy, it has become an effective tool in treating cancer and controlling its malignancy rate. Alongside there has been an increasing research interest in more supplementary effective diagnostic imaging tools for use in proton therapy treatment. This proton computed tomography (pCT) has been seen as a promising medical imaging tool and an alternative to the current X-ray-computed tomography (xCT) proton treatment planning. Prior to discussing the details of pCT, it is first important to provide an overview of radiation therapy and radiology which includes the development of particle therapy leading to proton radiotherapy (pRT). The issues and challenges posed in medical diagnosis of pRT shall be discussed as the foundation that has led to the innovation of pCT.

Radiation Therapy and Radiology

Radiation therapy (RT), also known as radiotherapy or radiation oncology, is a form of therapeutic treatment that utilizes ionizing radiation such as X-rays to treat tumors or cancerous tissues and prevent their malignant spread within the body. Radiology, however, emphasizes the application of medical imaging in treatment and diagnosis prior to RT. The history of RT and radiology and their known use can be traced back to Wilhelm Röntgen’s discovery of x-rays in 1895.

Common types of ionizing radiation sources for RT are photons, electrons, implanted or inserted radioisotopes (e.g., α, β, γ emitters) for brachytherapy (noninvasive radionuclides embedded in the patient), neutrons, pi-mesons, protons, and heavier charged ions such as ^{12}C and ^{20}Ne. Presently, RT treatment employing high-energy X-rays (or gamma rays) with electrons as their source is the most common technique; however, many countries still use ^{60}Co sources for treatment. [1]

Each source with its ionizing radiation produces different biological effects at the cellular level or at the molecular level of a DNA molecule. It is, however, not only the intrinsic properties of these aforementioned sources that result in different radiobiological effects, but it is also the amount of energy loss of the ionizing radiation (e.g., in keV or MeV) during its interaction with atoms and molecules of the cell, in the process causing ionization and excitation of the target's atomic electrons. The eventual effect is the alteration of the cellular structures, especially its DNA. This energy loss greatly contributes to the radiation dosage, and possibly death, of the cellular target. [2]

Besides choosing the right source, it is even more important to first diagnose a biological anomaly before subjecting a patient to the damaging effects of ionizing radiation, which would otherwise be dangerous. In radiology, the crucial task of imaging and identifying the anatomy is mainly achieved through common specialized imaging equipment. Instruments that are invariably used in many clinics include computed tomography, magnetic resonance, positron emission tomography, fluoroscopy, and ultrasonography. [3]

Types of Radiation Therapy

There are various forms of radiation therapy depending on the source of radiation and the means of delivering that particular radiation. These forms are categorized as external beam therapy, brachytherapy, and unsealed-source therapy. The last two form the principal methods of radioisotope therapy. The difference between them is based on their ability to specifically target their radionuclides onto the area under treatment. Brachytherapy uses sealed radioisotopes placed inside a hollow tube or applicator protecting the personnel from radiation exposure. These isotopes are more precisely placed near the affected area than unsealed isotopes which are systemically delivered and dispersed through infusion or oral ingestion. In brachytherapy and unsealed-source therapy, irradiation occurs *in vivo* when the source is internally embedded in the patient.

On the other hand, the radiation source is positioned externally to the patient in external beam therapy. Furthermore, this type of therapy can be further subdivided, based on applications and techniques, into conventional external beam radiotherapy, stereotactic radiotherapy (e.g., Cyberknife, Gamma Knife, and Novalis Tx), virtual simulation (e.g., 3-dimensional conformal radiotherapy, intensity-modulated radiotherapy, and image-guided radiotherapy), and particle therapy. The first three subdivisions refer to current treatments using photons in forms of X-rays and gamma rays. [4]

Types of Particle Therapy

Unlike the other forms of external beam radiotherapy, particle therapy typically utilizes beams of energetic protons, neutrons, and heavy ions. Although photons and electrons can be considered particles, they are not classified under this mode of therapy. Because it often uses hadrons as its source, it is sometimes referred to as hadron therapy. [5]

Hadrons are subatomic particles composed of quark constituents. The number and types of quarks further divide hadrons into baryons and mesons. Mesons consist of a quark and an anti-quark and display boson-like behavior, whereas the fermion-like baryons have three-quark composition such as neutrons and protons.

Hadron therapy is a type of radiation therapy which utilizes hadrons, particularly protons, neutrons, and heavy ions (carbon and neon), but the most common particle therapy uses protons. Figure 1 shows types of electromagnetic waves and the relative sizes of particles used in radiation therapy.

Proton Therapy

The idea of proton therapy was introduced by Harvard physicist and Fermilab founder Robert Wilson in the 1940s. He predicted that protons up to 300 MeV could be used to treat cancer, but the idea of devising an ideal dose delivery system of radiation was the motive which started proton therapy. This ideal radiation dose delivery system would deliver a defined uniform dose distribution within the target volume with no dosage within the tissue situated between the source and the target, thus sparing normal tissues from radiation damage. In reality, this unfeasible delivery system can be best achieved by delivering most of the radiation dose into the target volume with relatively little radiation damaging the surrounding healthy tissues. [1]

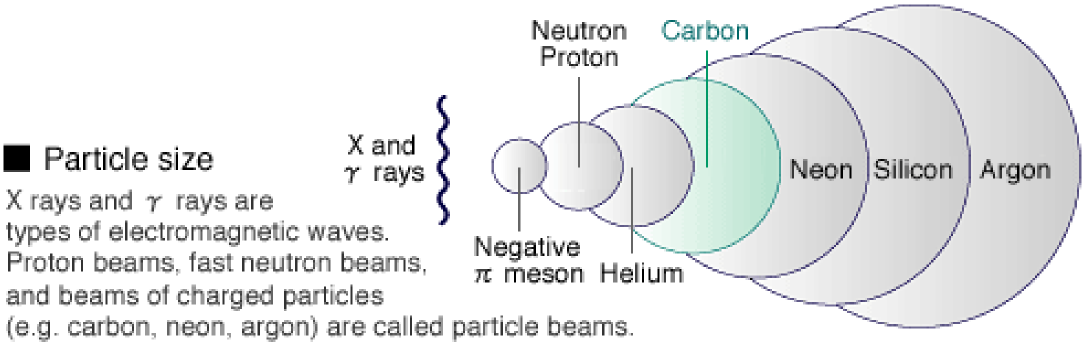

Figure 1: Different particles used as radiotherapy sources showing their relative sizes compared with other particles. Diagram was obtained from National Institute of Radiological Sciences. [6]

Delivery Systems for Protons

Producing a proton beam requires a high-energy delivery system such as accelerators that can project protons at high non-relativistic speeds (approximately 2/3 speed of light) enabling them to enter a patient and reach their target. Accelerators are the means of producing “high-energy” proton beams. Common types of these accelerators are circular in shape. Although many of them are able to deliver high-energy proton beams, they do have their limitations in their beam delivery capability.

Cyclotrons have constant magnetic field and RF frequency. The relativistic effects of the beam energy disturb the synchronization between the particle orbits and RF fields. Despite the disadvantage, cyclotrons can generate a continuous train of beam pulses and have large-area magnetic fields that confine the ions from zero energy to the extraction energy. For the uniform-field cyclotron, the gyrofrequency for non-relativistic protons is independent of the kinetic energy. Since the kinetic energy of protons is typically smaller than their rest energy, resonance between the orbital motion and accelerating electric field can be achieved. The protons are accelerated in the gap between the two D-shaped electrodes, at which an AC voltage is applied by an RF resonator. The two Ds are sandwiched between two opposite magnetic poles. Low-energy initial protons are continuously generated by the source at the cyclotron's center and are then accelerated to the opposite electrode by the positive half of the bipolar waveform of the RF cycle. In the opposite electrode, the protons follow a semi-circular orbit in the presence of vertical magnetic field before they are accelerated again in the gap with the polarity of the AC voltage reversed back to the original electrode. Small apertures in the gap limit the protons to a small range of phases in order to minimize the energy spread. After several crossings in the gap, the gyroradius and the kinetic energy increase until the protons are extracted. Figure 2 shows the layout of a uniform-field cyclotron. [7]

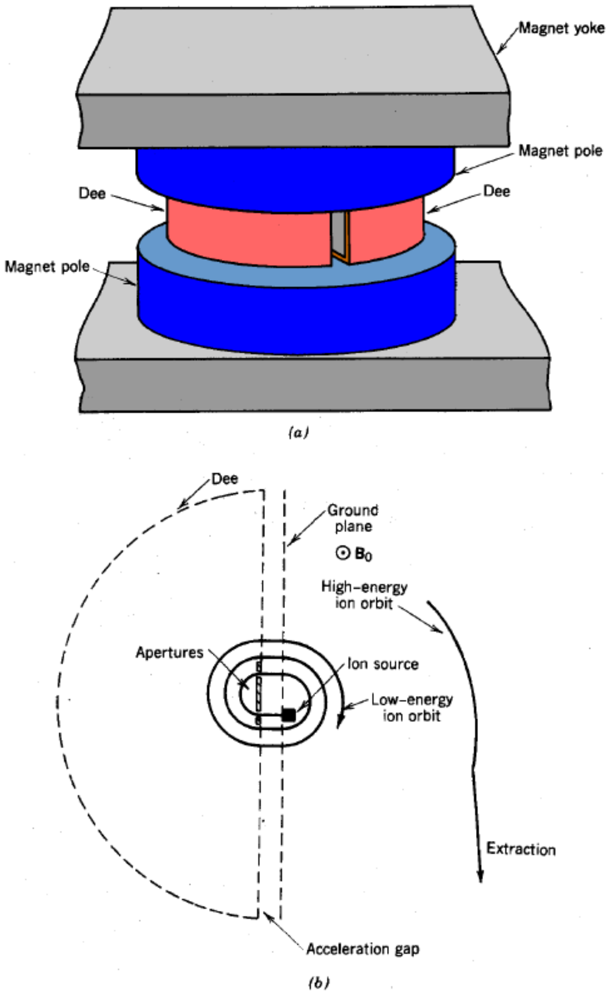

Figure 2: (a) The layout of a uniform-field cyclotron with 2 Dee electrodes and magnetic poles. (b) Overhead view of the proton acceleration region. A single left Dee aids in the injection and extraction of a proton.

In synchrotrons as shown in Figure 3, the magnitude of the magnetic field and the RF frequency are cycled. The focusing forces, the bending magnetic field, and RF frequency all vary independently from one another. This feature gives synchrotrons the ability to constantly maintain the oscillation periods of protons transverse to the propagation direction during acceleration, which avoids orbital resonances, and vary the magnetic field amplitude in order to preserve the orbital radius during acceleration. Unlike the cyclotron, the magnetic fields are located in the annulus of the synchrotron instead of its entire inner circle. Much higher beam energies can be generated. [7]

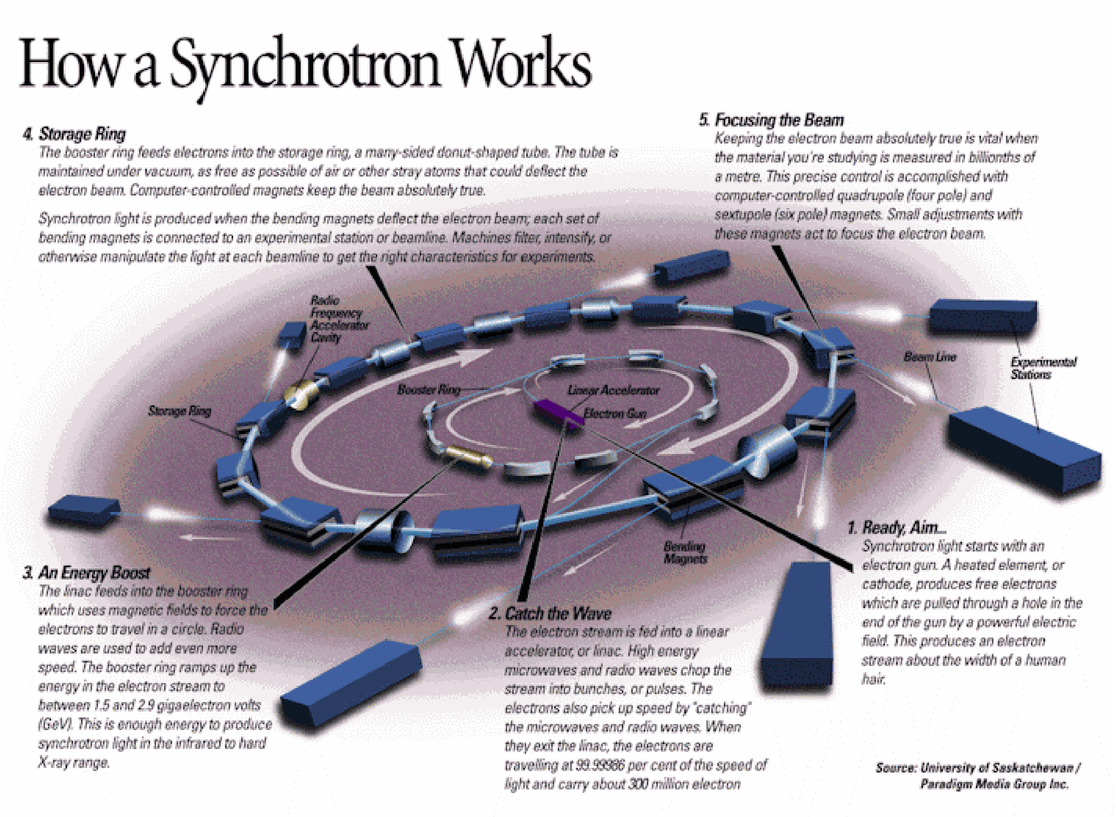

How a Synchrotron Works

4. Storage Ring
The booster ring feeds electrons into the storage ring, a many-sided donut-shaped tube. The tube is maintained under vacuum, as free as possible of air or other stray atoms that could deflect the electron beam. Computer-controlled magnets keep the beam absolutely true.

Synchrotron light is produced when the bending magnets deflect the electron beam; each set of bending magnets is connected to an experimental station or beamline. Machines filter, intensify, or otherwise manipulate the light at each beamline to get the right characteristics for experiments.

5. Focusing the Beam
Keeping the electron beam absolutely true is vital when the material you're studying is measured in billionths of a metre. This precise control is accomplished with computer-controlled quadrupole (four pole) and sextupole (six pole) magnets. Small adjustments with these magnets act to focus the electron beam.

3. An Energy Boost
The linac feeds into the booster ring which uses magnetic fields to force the electrons to travel in a circle. Radio waves are used to add even more speed. The booster ring ramps up the energy in the electron stream to between 1.5 and 2.9 gigaelectron volts (GeV). This is enough energy to produce synchrotron light in the infrared to hard X-ray range.

2. Catch the Wave
The electron stream is fed into a linear accelerator, or linac. High energy microwaves and radio waves chop the stream into bunches, or pulses. The electrons also pick up speed by "catching" the microwaves and radio waves. When they exit the linac, the electrons are travelling at 99.99986 per cent of the speed of light and carry about 300 million electron

1. Ready, Aim...
Synchrotron light starts with an electron gun. A heated element, or cathode, produces free electrons which are pulled through a hole in the end of the gun by a powerful electric field. This produces an electron stream about the width of a human hair.

Source: University of Saskatchewan / Paradigm Media Group Inc.

Figure 3: Layout of a typical synchrotron. [8]

Laser-induced plasma "wakefield" accelerators have been investigated as a possible compact and more cost-effective measure for delivering energy- and intensity-modulated proton beams for therapy. Pulsed lasers would accelerate the protons at high energy. A compact particle/energy selection and beam collimating system must be designed to counter the broad energy and angular distributions caused by the laser-accelerated protons for accurate beam delivery. Figure 4 is a schematic of the therapy setup using a wakefield accelerator. [9]

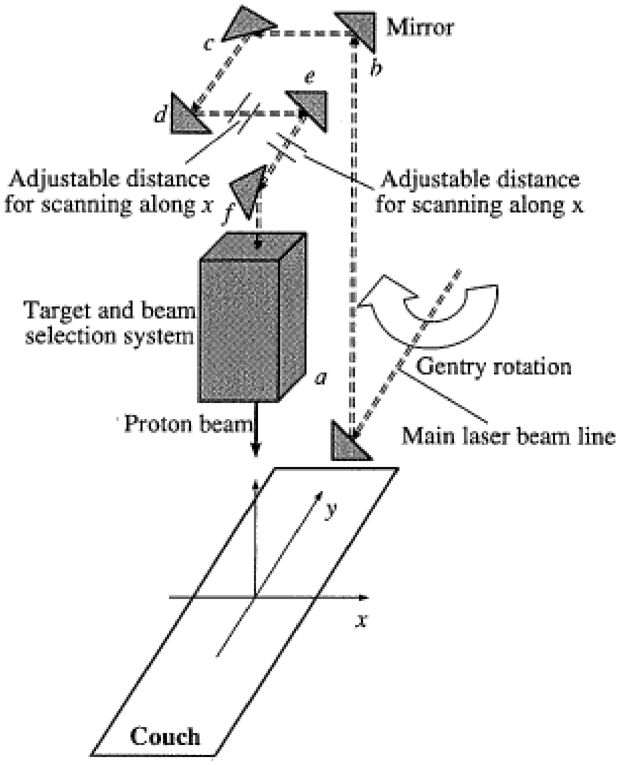

Figure 4: Schematic showing the treatment head of a conceptual laser-proton therapy system. [9]

Dielectric wall accelerators (DWA), in Figure 5, must achieve high gradients of electric fields on the order of 100 MV/m to accelerate a proton bunch. Conceptually, the dielectric lining at the side of the beam pipeline reduces the spatial overhead and allows the electric field on the dielectric wall to be predominant as the on-axis accelerating field. [10] The essential elements of DWA are their high-gradient vacuum insulators, high-bulk-breakdown strength dielectrics for pulse forming lines, and closing switches for high-gradient operation. [11]

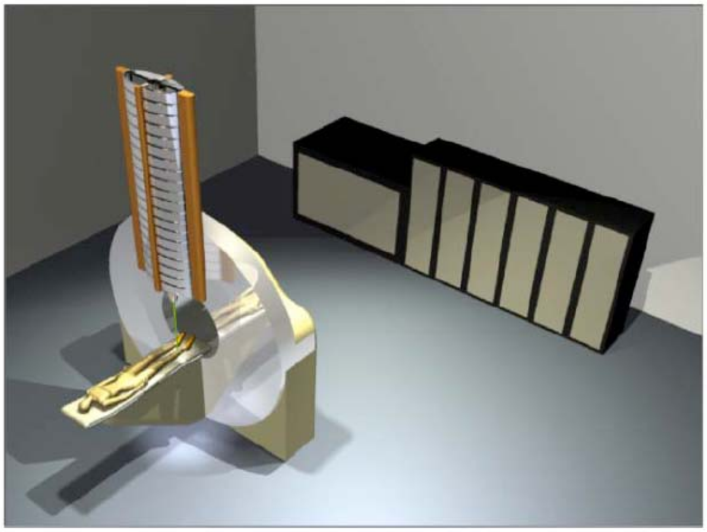

Figure 5: DWA compact proton therapy concept. A compact linac is mounted on a gantry and fit into a standard conventional linac vault. [11]

Fixed field alternating gradient (FFAG) accelerators display intermediary features between those of the cyclotrons and synchrotrons. Initially, they were weak focusing devices and were fixed-field accelerators like the cyclotrons but with the discovery of alternating gradient, 3D strong focusing became possible in the presence of uniform magnetic field. There is alternating gradient focusing in the transverse direction of the beam and phase focusing with radiofrequency acceleration in the longitudinal direction. Proton beam acceleration is accomplished by varying the frequency in the RF cavities with large field gradients. [12] The betatron oscillation frequency (tune) is held constant during acceleration to avoid resonance crossovers, which could result in beam losses, making the FFAG scaling because of strong focusing. Scaling FFAGs thus have no variations in betatron tunes with beam momentum – i.e., zero chromaticity. FFAGs have radial-shaped or spiral-shaped sectors, as shown in Figure 6. [13] But recently it has been suggested that non-scaling FFAGs with nonzero chromaticity would reduce the required orbit offsets during acceleration and the size of their aperture while maintaining the low cost of magnets used. Also, because of their fixed magnetic fields, strong focusing ability, and smaller aperture, non-scaling FFAGs would be advantageous for spot scanning, resulting in very low beam losses and better control of the beam. [14] Figure 7 is an example of an FFAG.

Fixed-Field Alternating-Gradient

- Spiral Sector FFAG
- Radial Sector FFAG

Figure 6: Schematic top view of an FFAG. The triplet lattice DFD allows strong focusing with minimal dispersion for the scaling FFAGs. (left) Spiral sector FFAG and (right) radial sector FFAG with the triplet lattice. [13]

Figure 7: Proof-of-principle FFAG (top). FDF dipole triplet with scaling gap (bottom left) and broad band accelerating cavity (bottom right). [15]

The Basics: Protons Interacting with Matter

Before any serious discussion about pRT and pCT can take place, it is important to discuss the properties that allow protons to be used both as a therapeutic and as an imaging tool. These properties can be described by the underlying principles of proton interaction with matter.

As protons traverse through matter, they experience energy loss, thereby depositing energy. This phenomenon lies in the Coulomb interaction mainly between protons and the orbiting electrons in the matter. The collision between these particles results in ionization and excitation of the atoms. These electrons from the now ionized atoms then further ionize neighboring atoms. In the process, the protons lose energy and are slightly scattered from these collisions. This interaction contributes to the mean energy loss, which is a significant factor in making pCT possible.

In the case of Coulomb interaction between protons and the atomic nuclei, the incident protons will experience a repulsive force as they pass close by the positively charged nucleus of the atom. Also because of the massive nuclei compared to the atomic electrons, the incident protons are scattered more during this interaction than during the proton-atomic electron collision; however, the angle of deflection is still very small. The angular deflections caused by these proton-nuclei interactions will exhibit statistical fluctuations, resulting in a net angular and radial deviation. This form of interaction is known as multiple Coulomb scattering (MCS).

Like the electrons, protons can experience a centripetal acceleration when they encounter the field of an atomic nucleus. The force field of the nucleus will deflect the proton's trajectory, changing its acceleration and causing an emission of Bremsstrahlung photons. However, the "likelihood of a Bremsstrahlung is roughly proportional to the inverse of the square of the particle mass." [1] Hence, the proton's Bremsstrahlung is less noticeable than the electron's and is the least significant of all the proton-matter interactions.

Protons may have interactions with the atomic nuclei, through the strong nuclear force. Two types of collisions may occur: elastic and non-elastic. In elastic interaction, the protons lose significant amount of energy and are usually deflected by several degrees, but the atomic nuclei are not fragmented. In contrary, the atomic nuclei can be broken apart, leaving behind a heavily ionized fragment at the site of the non-elastic interaction. The lighter ionized fragments are transported at high speeds away from the site. Here are respective examples of elastic and non-elastic nuclear interactions between a proton and an oxygen atom: $p+{}^{16}O \rightarrow p+{}^{16}O$ and $p+{}^{16}O \rightarrow p+{}^{15}N+p$.

In the case of water or human tissue, a significant fraction of the proton energy loss is due to non-elastic nuclear interactions with the target nuclei. That fraction is about 5% for 90 MeV proton, 10% for 140 MeV, and 20% for 240 MeV. [16]

Physical Interpretation of the Depth-Dose Distribution of the Proton Beam

As the protons reach their target volume, the dose deposited by the protons rises sharply near the end of their range, creating a Bragg peak as portrayed in the depth-dose distribution curve in Figure 8. Next we will clarify the meaning of stopping power, linear energy transfer (LET), and dose.

This quantity, $\frac{dE}{dx}$, is called the stopping power, which describes the amount of energy lost per unit length along the track of a particle. [17] The proton energy loss or the proton stopping power is expressed by an approximate version of the Bethe-Bloch formula at the low velocity limit:

$$\frac{dE}{dx} \alpha \frac{1}{v^2}(\frac{Z}{A})z^2, \tag{1}$$

where Z and A are the atomic and mass numbers of the target nucleus, respectively, and z is the charge number of the proton. [1] Near the end of its range, the proton velocity is close to zero; eventually, the proton comes to a stop and the dose drops to zero at the end of the range. Figure 9 shows the proton whose velocity v_A at position A is greater than v_B at position B. Stopping power, more accurately known as the mass stopping power, is the energy absorbed by the medium per-unit thickness x divided by the medium density ρ (i.e., $\frac{1}{\rho}\frac{dE}{dx}$). [17] It generally includes ionization events, delta rays, secondary protons from inelastic collisions, and other charged nuclei but excludes secondary neutrons. Ionization and Bremsstrahlung and delta rays are accounted for in the Bethe-Bloch, but the inelastic collisions are not.

Linear energy transfer (LET) is the restricted stopping power which has an energy exchange limit unlike the stopping power. Energies below the energy limit are included in the restricted stopping power calculation. If the energy limit approaches infinity, the LET is equal to the (unrestricted) stopping power. [17] Furthermore, the LET excludes the effects of Bremsstrahlung and delta rays (greater than 10 keV), which are secondary electrons that form their own track after being collided with initial electrons, because they are not locally absorbed. LET takes account of the energy locally deposited along the particle track, but the stopping power is the total energy lost by the particle. For protons and heavy charged particles, both are nearly equal. For fast electrons, LET does not include Bremsstrahlung or the delta rays. The unit for LET and stopping power is the same (i.e., $\frac{MeV \cdot cm^2}{g}$). [18]

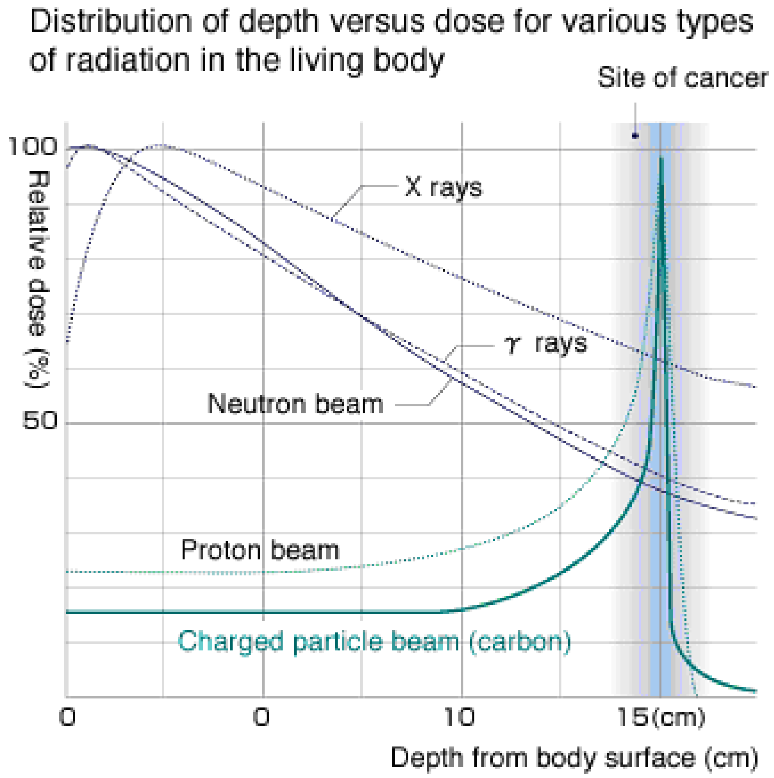

Figure 8: Depth-dose distribution curves of various types of radiation sources. This figure was obtained from the National Institute of Radiological Sciences. [6]

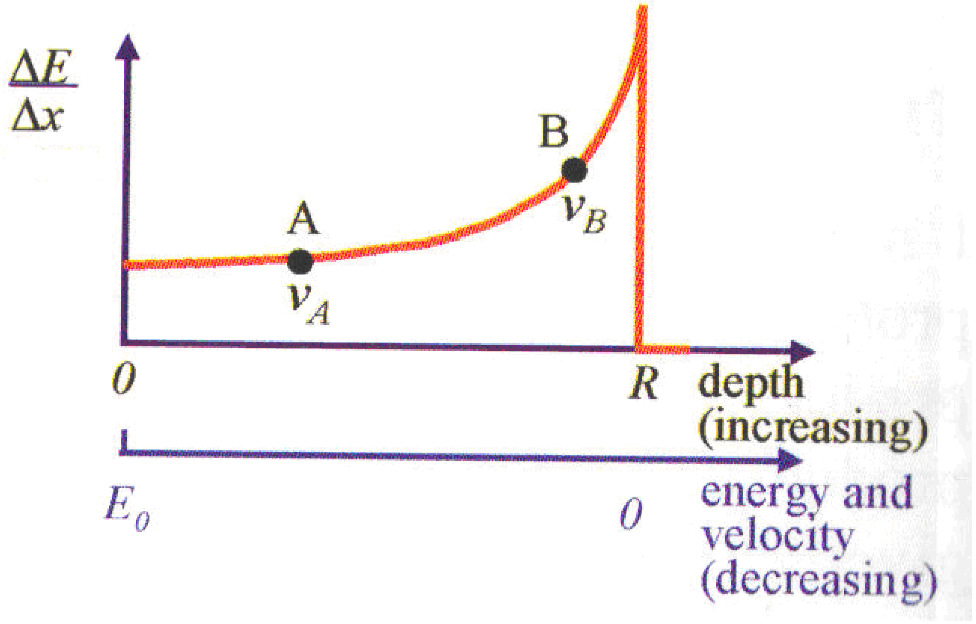

Figure 9: *R* indicates Range; $\frac{\Delta E}{\Delta x}$ is the stopping power. Bragg peak is the result of the Coulomb scattering of the protons from the atomic electrons. [1]

Proton dose is the proton fluence times the stopping power. Proton fluence is the number of mono-energetic protons crossing a unit area whose plane is perpendicular to the proton beam. The unit for dose is the energy absorbed by the unit mass of medium (i.e., $1 J/kg = 1 Gy$). [17]

After depositing most of their energy which contributes to the dosage, the resulting energy loss of the protons due to Coulomb interactions with atomic electrons causes a decrease in the proton velocity. This slow loss in proton energy is the reason for the Bragg peak formation (at the site of the tumor). A fraction of the proton's initial kinetic energy has been transferred to the atomic electrons via ionization.

In practice, the Bragg peak is hardly an infinitely sharp peak. The two effects that dull this peak are range straggling and energy spread. The cause of straggling is the result of statistical fluctuations in the ionization processes which cause a slight range extension in the penetration depth of the stopping protons. The energy spread is the result of different incident protons having different energies due to whatever energy profile is produced by the accelerator.

In both elastic and non-elastic cases, nuclear interactions between the protons and the atomic nuclei often induce significant energy losses of the incident protons and significant degree of angular scattering. Consequently, fewer incident protons will reach the end of their range. However, there are other events resulting from these nuclear interactions.

First, the primary incident protons are greatly scattered, and secondary protons, which are bombarded and knocked out by these primary protons, are further transported. These secondary protons with lower kinetic energy compared to the primary's will not surpass the primary protons' end of range; thus, a characteristic tail appears in the lateral dose distribution of the beam. (More on this in the section "Physics of pCT.")

Second, the heavily ionized fragments have a high stopping power that can locally deposit their dose close to the site of the nuclear interaction, preferably at the tumor site. This will thereby increase the relative biological effectiveness (RBE), which varies with LET, in that area. The RBE is the ratio of the dose of a standard reference radiation beam (normally 250 KV X-rays) to the dose of the experimental radiation beam to acquire the same biological response. Generally, a high RBE indicates increasing affliction induced onto a biological tissue. This implies that the dose of the experimental test beam – proton beam in this case – must be significantly lower than the dose of the reference beam to achieve a high RBE.

Last, neutrons and photons produced from these nuclear interactions largely escape the patient without undergoing further interaction, but they contribute relatively little to the dosage. After a large fraction of the proton's initial kinetic energy has been transferred to the secondary protons and heavily charged particles, its remaining energy is transferred to the neutrons and photons, allowing them to escape. By the end of the process, these incident protons are lost.

The blue curve in Figure 10 shows steady negative slope and the steep falloff, represented by nuclear interactions, and range straggling and beam energy spread, respectively. It represents the plot of proton fluence depth – i.e., relative number of protons crossing through an area at specific depth. The red curve is the plot of the dose-depth distribution. Most importantly, these plots are true for near mono-energetic protons.

Aside from the medium, the position of the Bragg peak depends on the initial energy of the beam. Higher beam energy will produce a greater range of the protons, whose Bragg peak will be located at greater penetration depth.

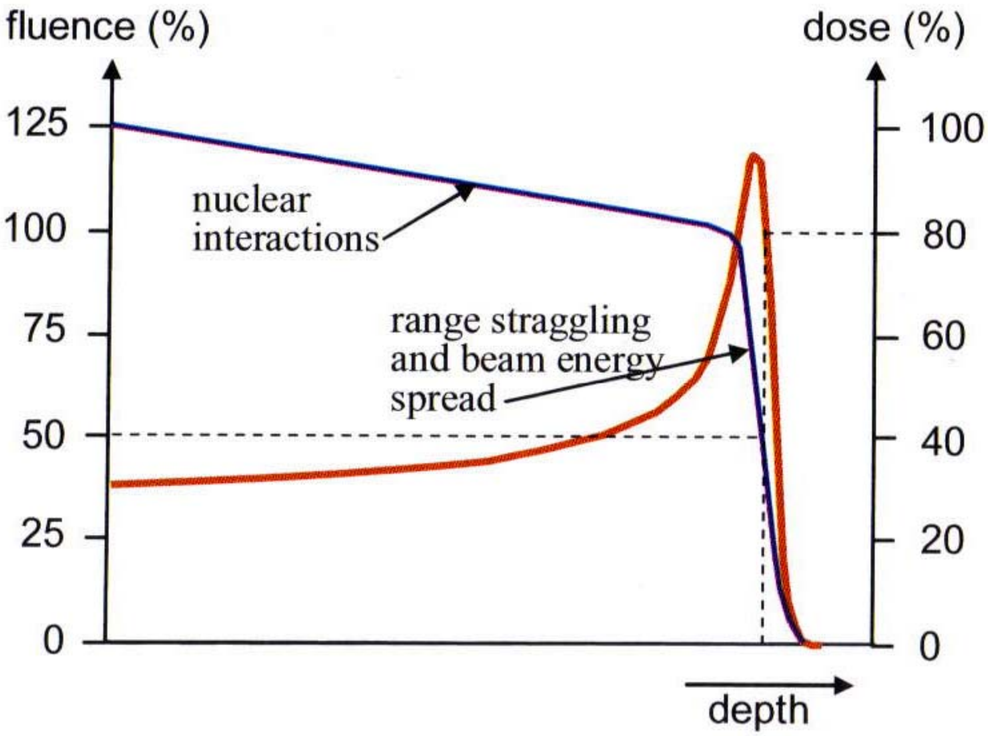

Figure 10: Schematic plot of proton fluence-depth (blue) and dose-depth (red) distributions of mono-energetic proton beam. Typically, the 80% dose on the falling edge of the Bragg peak and the 50% fluence share the same depth. The fluence is relatively scaled in such a way that the incident protons start out 25% more in order to establish correspondence between the fluence and dose. [1]

The range of protons is referred to as the *continuous slow-down approximation* (CSDA). It is a close approximation to the mean path length of a decelerating charged particle under the assumption that the rate of energy loss at every point along the particle track is equal to the total stopping power of that particle in the absence of energy-loss fluctuation – a product of the proton's Coulomb interaction with electrons. The CSDA is calculated by integrating the reciprocal of the total stopping power with respect to energy. [19]

Lower energy protons with shorter ranges have narrower Bragg peaks. Their range straggling and energy spread are more or less independent of the initial energy. The reason for this narrow Bragg peak is the relatively constant ratio between the width of the Bragg peak to the range of the protons for all initial energies. Therefore, greater energy protons with longer ranges have broader Bragg peaks.

Another characteristic of lower energy protons is their higher peak-plateau dose ratio (i.e., ratio of the dose at the tip of the Bragg-peak to the dose at “zero” depth or the surface). The narrower widths of the Bragg peaks have a higher peak, whereas Bragg peaks with broader widths have a lower peak because the amount of energy deposited, regardless of the initial proton energy, is more or less constant. That is, the area under each individual Bragg peak curve should be the same.

The distal falloff of the dose for lower energy protons is steeper than that of higher energy protons. Because of its higher peak-plateau dose ratio, the narrowing of the peak widths creates this “distal penumbra.” Hence, as the energy is reduced, the distal penumbra falls off more rapidly.

Figure 11 illustrates these points.

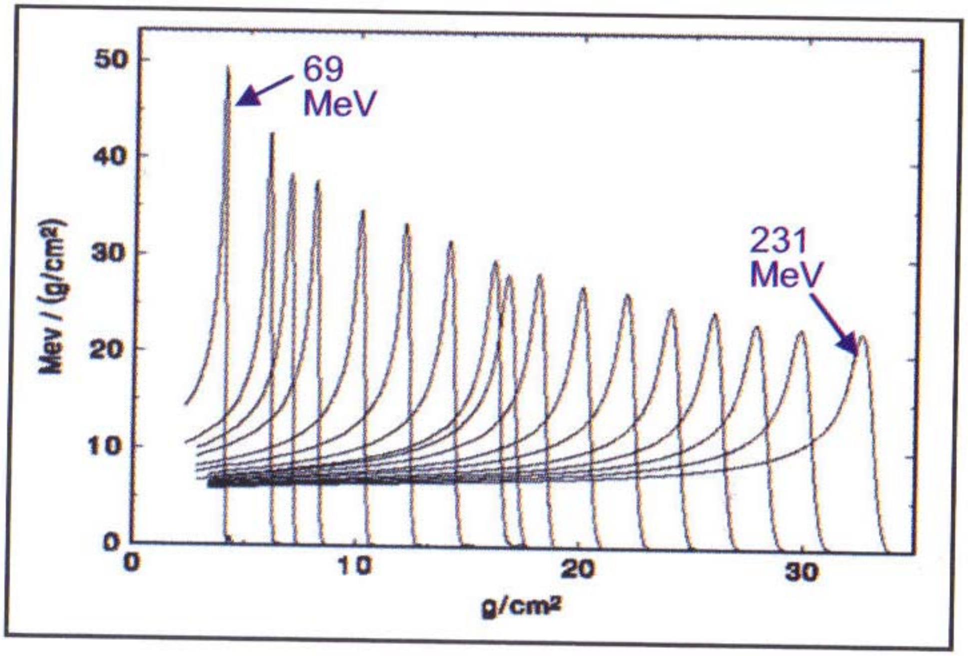

Figure 11: This dose-depth distribution shows that the lower 69 MeV proton energy beam has a higher peak-to-plateau dose ratio, shorter proton range, and narrower Bragg peak width than the 231 MeV. [1]

In many cases, the Bragg peak is often narrower – usually in several millimeters – than the size of the tumor undergoing irradiation. The tumor size can range from a couple of centimeters to more than 10 centimeters, and a method for applying high doses over the wide neoplastic region is needed. Using several differently weighted Bragg peaks to fix a relatively constant high dose at the entire target region has become a practical approach. The superimposition of these Bragg peaks at the distal region, where the tumor is located, form a spread-out Bragg peak as shown in Figure 12.

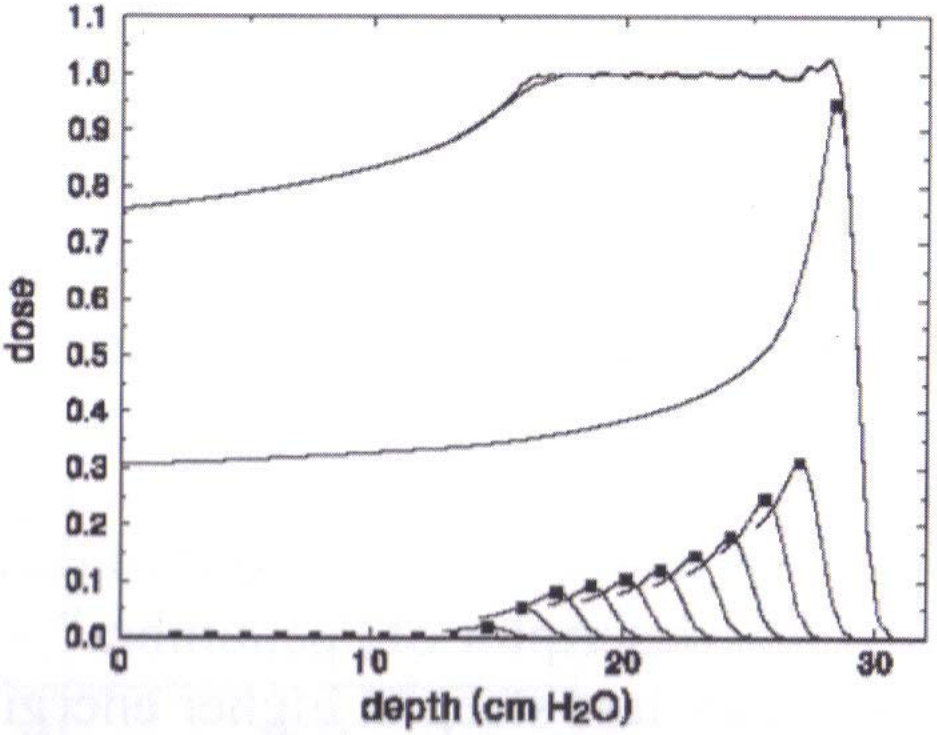

Figure 12: The top-most curve illustrates the spread-out Bragg peak composed of approximate mono-energetic proton beams (the low individual Bragg peaks) of lower energies and weights. The middle curve is the mono-energetic proton reference beam. [1]

Unfortunately, the disadvantage of this method is that the proximal dose at the entrance of the patient depends on the depth of the target location; protons needed to treat deep-seated tumors via spread-out lack the skin-sparing ability. Furthermore, the dose is inversely proportional to the square of the tumor distance from the proton source. By the time the protons arrive at the region, they lose their potency, and the distal dose received will be much less than the proximal dose at the skin. [1]

Physical Interpretation of the Dose-Lateral Displacement Distribution of the Proton Pencil Beam

Like the depth-dose distribution, the lateral dose distribution yields important information of the physical phenomena of the proton, but at its off-axis points. A pencil beam is used in proton therapy because its lateral size width, angular divergence, and energy spread are near infinitesimally small, making targeting more accurate. Nevertheless, multiple Coulomb scattering diminishes the height of the Bragg peak of the proton pencil beam. Instead, the MCS causes protons to spread out more laterally and with greater scattering at distal penetration depth. The dose amplitude near the end of range is low. Figure 13 shows these occurrences.

In the angular deviation distribution and lateral distribution of the pencil beam, their main section appears close to a Gaussian distribution. Near the end of the range, the standard deviation of the lateral distribution is roughly 2% of the range. As mentioned before, the lateral spread is less at the proximal depth than at the Bragg peak. The standard deviation at the proximal depth will be less than the 2% of the range. [1]

Although the main section of the angular and lateral distribution curves exhibits a near-Gaussian profile due to MCS's small angular deviations, the tails of these distribution curves are the result of few large angle scatterings, exhibiting non-Gaussian behavior. These tail ends are attributed primarily to the secondary protons' largely scattered angles from their nuclear interaction, not to the MCS. [1]

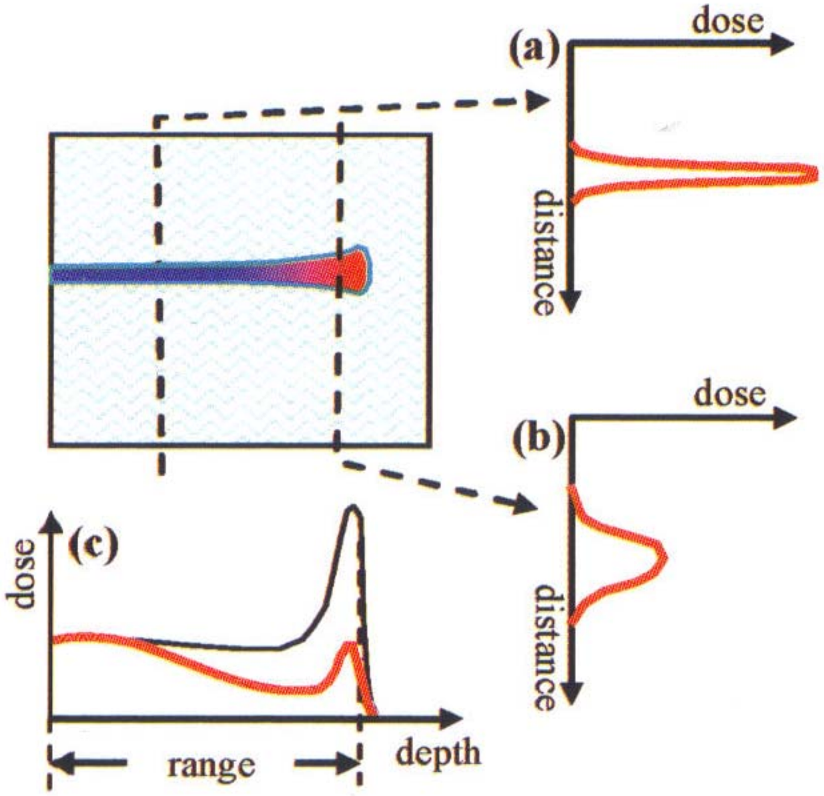

Figure 13: Dose-lateral (a and b) and dose-depth (c) distributions. The depth position of (a) is more proximal than the position of (b) and is displaying a greater dose amplitude with less lateral spread. Fewer MCS events occur at shorter ranges. [1]

As mentioned, the secondary particles produced by elastic and non-elastic nuclear interactions are the heavily charged nuclear fragments, secondary protons, and neutrons. Because the nuclear fragments travel a short distance away from the interaction site, they are not scattered and do not contribute to the lateral distribution and are thus independent to the tail ends. The scattered secondary protons, on the other hand, add to the tail end display. The neutrons largely escape from the patient without further interaction but contribute to low dose inside and outside of the beam. They have an unfortunate consequence of producing secondary cancer. [1]

Figure 14 is a diagram of three different scattering types, each having a distinct dose-lateral profile. As shown in profile, the scattered secondary protons contribute to the long tails of the distribution. The small angular deviations characterizing the MCS yield the greatest dose amplitude with the least lateral spread compared to plural/single Coulomb scattering and proton scattering, but as MCS becomes more frequent at greater depths, the dose amplitude starts to decrease and the lateral parameter spreads out more as shown in Figure 13.

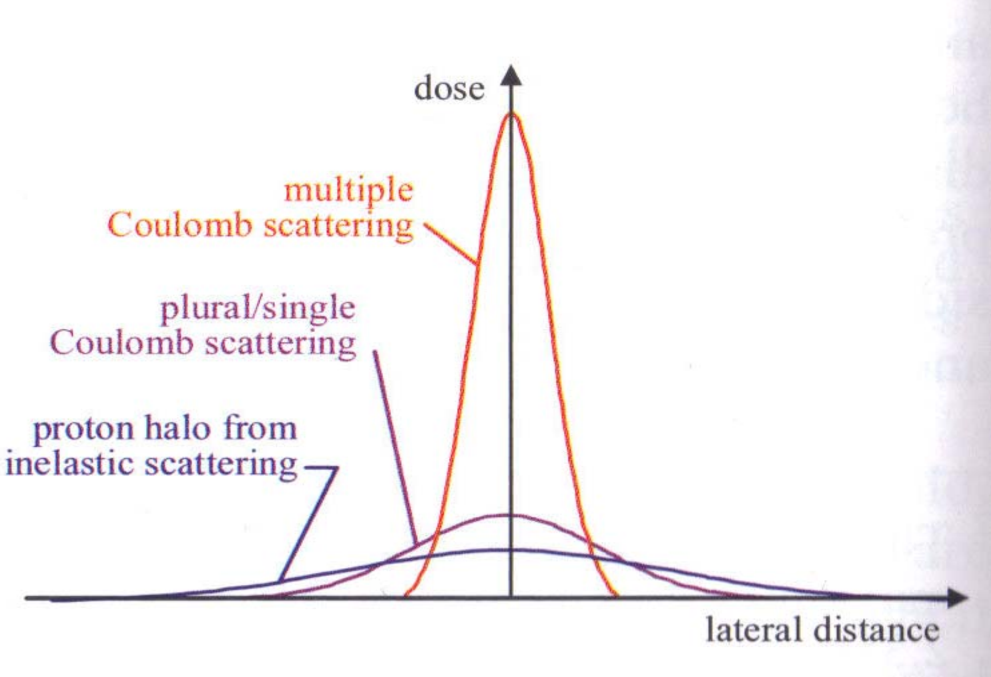

Figure 14: Multiple Coulomb scattering (red) has the smallest angular deflections with the largest number of collisions, making it appear the most Gaussian-like distribution. Plural/single Coulomb

scattering (purple) has a very few number of collisions or just one collision. Also, the extended tails signify energy loss of the primary proton; thus, inelastic scattering yields the greatest energy loss, followed by plural/single, and MCS. [1]

Proton-Computed Tomography (pCT)

Analogous to Robert Wilson's suggestion of proton therapy in the 1940s, the radiological aspect of using protons for imaging instead for only treating tumors was proposed by Allan Cormack in his Nobel Prize speech. He and his contemporary, Godfrey Hounsfield, shared the Nobel Prize for Physiology or Medicine in 1979 for their discovery of X-ray-computed tomography (xCT).

Cormack indicated that the required dose for proton scans is five to ten times less than that for X-ray scans in order to retrieve the same amount of information. In addition, the way protons are brought to rest with their Bragg peak formation and distal dose falloff is different from the stopping mechanism of X-ray photons which are scattered or absorbed. However, a much more expensive cyclotron would have to replace the X-ray scanner in order for pCT to work. [20]

Brief Introduction to xCT and Issues of Its Current Use in Proton Treatment Planning

Before discussing pCT in detail, we must first understand the use of xCT as an important imaging tool and its limitation in proton therapy, which has stirred up ideas for pCT.

Prior to xCT, X-ray radiographs were 2D graphic representations formed by superimposing images of tissues which lie within the photon path between the radiation source and the target. The 3D image representation could not be obtained. In the case of xCT, X-ray projection measurements are taken all around the patient's body; these subsequent measurements compute every point of the tissue within a 3D space via projection angles to a typical spatial resolution of less than 1 millimeter. These 2D cross sectional slices at each projection angle will then be superimposed to form the 3D image of the tissue. In this process, xCT reduces the chance of misidentifying tissues. Figure 15 is a schematic of positioning of the patient under a CT scanner.

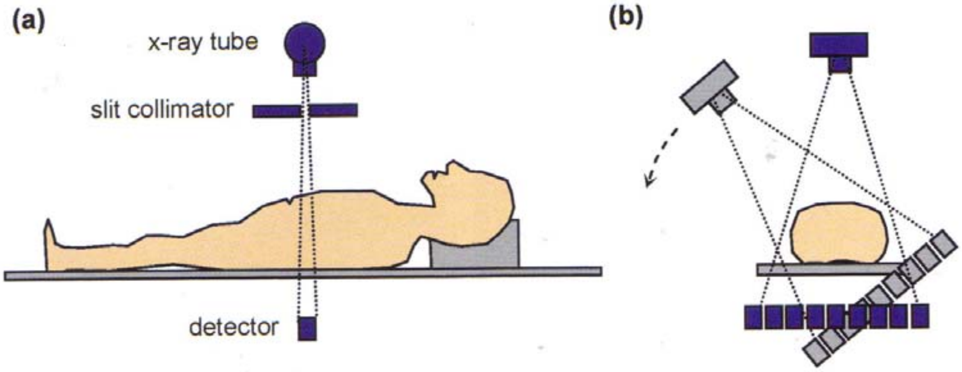

Figure 15: (a) Lateral view of patient lying in supine position with photon source. (b) Angular projection rotations of the photon source with respect to the isocenter – point in space through which central ray of the beam passes and point at the center of the tumor. [1]

The property measured in xCT is the ratio of the linear X-ray absorption coefficient of the tissue (or its attenuation coefficient) at a given point to the absorption coefficient of water. It is expressed in Hounsfield units (HU) with -1000 HU for air and 0 HU for water. [1] At each projection angle, CT iterative image reconstruction algorithms will take these HU measurements to deduce the X-ray absorption coefficient values for each voxel, as shown in Figure 16.

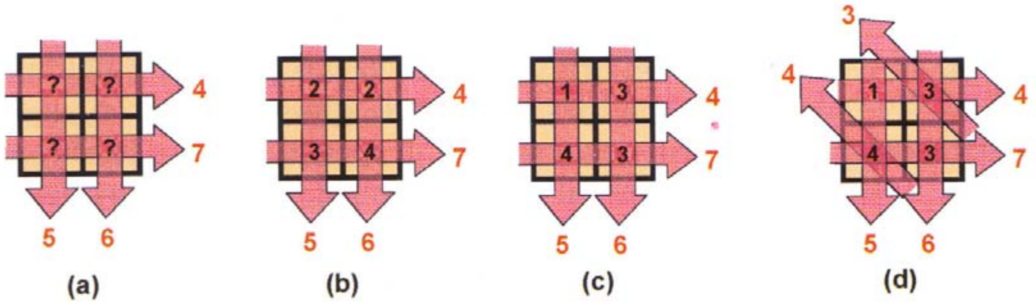

Figure 16: Measured HU values at the right and bottom margins of each 2x2 array in (a), (b), (c), and (d). Each pair of parallel rays is positioned at different angles. These arrays represent the same cross-sectional tissue. In this overly simplified reconstruction example, there are four voxels in each array. The values in these voxels are the absorption coefficients (or linear attenuation coefficients). All these numbers are in percentages. [1]

The different absorption coefficients correspond to different tissue densities, where denser materials can scatter or absorb a photon more. By doing so, this would help identify tissue types. The correlation between the coefficients and densities is based on Radon transforms of functions or objects – e.g., tumor – and evaluating the line integrals of attenuation coefficients along the photon's path, whose result is the total density along that entire line projection. Hence, in xCT, we are reconstructing the absorption or attenuation coefficients to indirectly identify tissues via their density. [21]

Presently, in proton therapy, proton dose calculations are performed by xCT, and patients are positioned with the aid of X-ray radiographs, since megavoltage or orthovoltage cone-beam CT is not yet widely performed in existing proton treatment centers. [22] However, there are disadvantages that xCT poses when it comes to diagnosing the tumor, which we will discuss later.

In terms of therapy, Figure 8 has shown that the dose of the X-rays is higher than the proton dose upon entering the patient. By the time the photon reaches the tumor, most of its energy will be deposited in the tissues along the photon path. The dose deposited by the photon on the tumor is much less than that deposited by the proton. Although Figure 17 shows the hardening of the 10 MeV photon beam near the zero depth, which makes the photon dose appear less than the 200 MeV proton dose, much more of the peach-colored regions show the unwanted dose delivered by the photons, effectively harming healthy tissues surrounding the target tumor region. [1] Beam hardening by adding filtration, such as beryllium absorber window, upstream enriches the beam with higher energy photons with greater penetration power; in other words, lower energy photons are filtered out, thus explaining the initial positive slope of the photon dose curve. [23]

Proton treatment plans are carried out by using the xCT data scan. As mentioned before, the xCT measures the HU that is then used to predict the linear absorption coefficient. Nevertheless, the present uncertainties of xCT-based proton treatment planning have resulted from the conversion of Hounsfield values to relative electron density values [24, 25]. The accuracy of this proton treatment planning is also limited due to the difference of physical interactions between photons and protons [26].

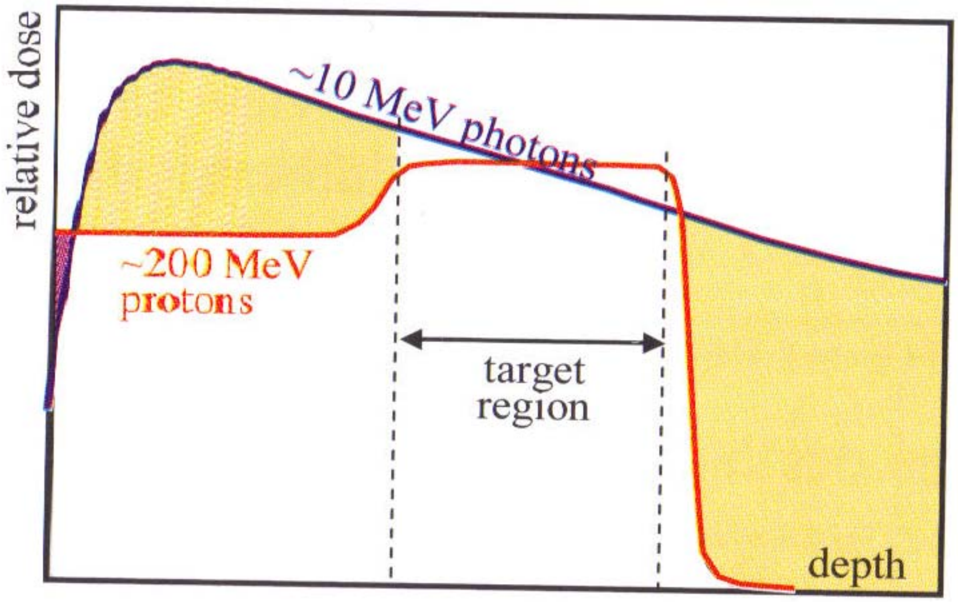

Figure 17: Peach-colored regions are the unwanted photon dose. The purple region is the area much spared from photon dose, but does not compensate much for the unwanted dose regions. The proton's Bragg peak falls off quickly, sparing the tissues behind the target region. [1]

Aside from these limitations due to inherent physical interaction differences between photons and protons, which we cannot rectify, certain corrections can be made to reduce these uncertainties. To guarantee a precise treatment and accurate targeting, we must obtain the "relationship between CT Hounsfield Units and electron densities (or proton stopping powers for proton radiotherapy), which is the basic input … for tissue heterogeneities." This relationship is the conversion function of the calibrated HU to the electron densities or the stopping powers. To determine the calibration of HU for a biological tissue (i.e., stoichiometric calibration), measurements are based on tissue-equivalent materials. [27] Figures 18 and 19 are the calibration curves for converting HU to stopping powers and then to electron densities.

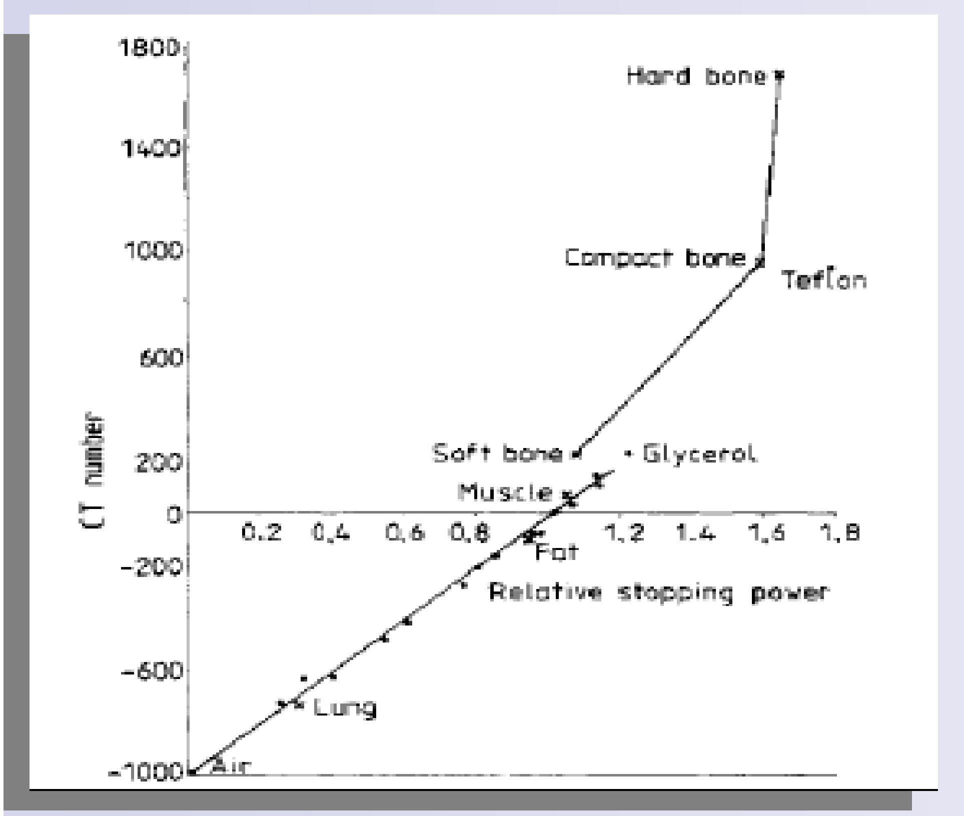

Figure 18: Conversion of HU numbers to relative stopping power for different materials. [28]

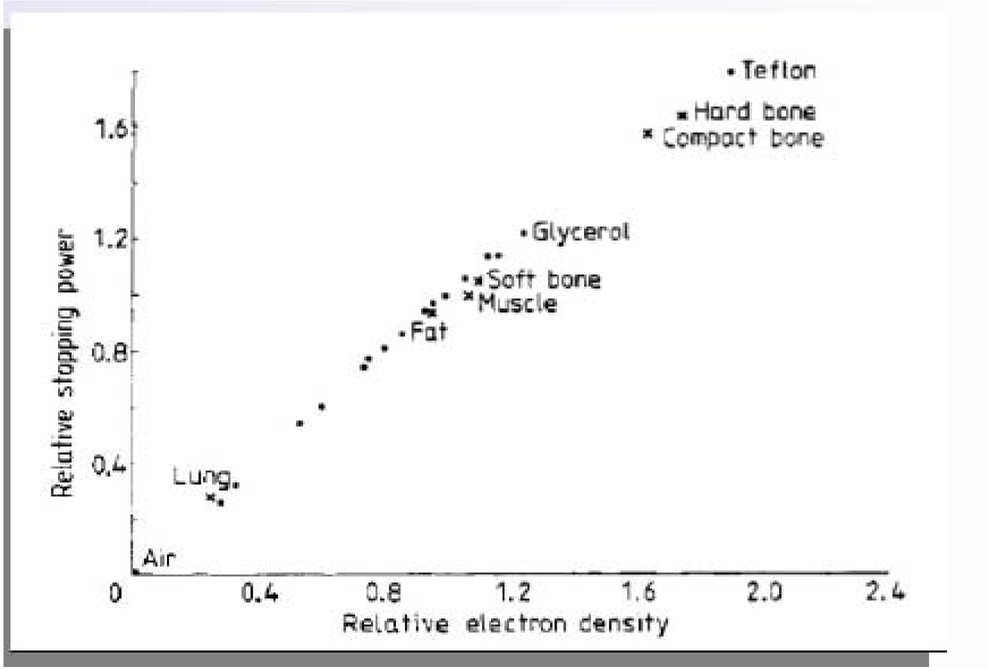

Figure 19: Converting stopping power to electron density for different anatomic materials. [28]

The magnitude of errors in converting HU to proton stopping powers is approximately 3%. [29] The resulting uncertainties of the HU conversion to relative electron density can have range errors from several millimeters up to more than 1 cm, depending on anatomical features. For example, the current proton range uncertainty in the brain is between 1 to 3 mm. [25]

The Need for pCT

Since Cormack's proposal of replacing photons with protons as a source for a more effective computed tomography, pCT has been increasingly studied as an alternative to xCT in terms of accurately predicting the Bragg peak location and imaging a target such as a tumor because relative electron density distributions can be directly measured with pCT. This makes pCT more suitable than conventional X-rays for the planning of proton radiation treatment. [20] With the current xCT-based proton treatment planning, proton therapy cannot be fully exploited because of the range uncertainties posed by the HU conversion. In order to minimize these uncertainties, the long-term goal for developing the capability of pCT instead of xCT becomes important. [25]

Mathematical Works Concerning pCT

Most of the earlier concepts of xCT, as described by Austrian mathematician Johann Radon, apply to pCT and serve as the basis for pCT image reconstruction but with some modifications to the equations, such as the line integrals, which take into account the differences in the physical interactions between photons and protons. But as CT imaging technology changes and becomes more sophisticated, precision imaging becomes more difficult to ascertain because of increasingly technical challenges, especially posed by reconstruction techniques. For example, imaging reconstruction methods become more complex in form; the algorithms used for xCT image reconstruction with the X-ray absorption coefficients have to be replaced by iterative algebraic reconstruction algorithms that require parallel computing for pCT.

Nevertheless, we will reference some past works, by Allan Cormack, Enrico Fermi, Leonárd Eyges, Gert Molière, Virgil Highland, and others, that started pCT theory, particularly the MCS.

Integral Transform Required for Computed Tomography

Tomography determines the total density of the object's internal structure by individually determining the densities of all possible line projections or paths passing through the object. Radon transform of an unknown object, expressed as a function *f*, is a set of total densities along different lines at different angles. It is also known as the X-ray projection. Mathematically, it is an integral transform, whose value on line *L* is defined to be the total density of *f* along *L*:

$$\int_L f(x)dx \,. \tag{2}$$

But the general form of the Radon transform is an operator *R* defined in the set of Lebesgue integrable functions *f* in an n-dimensional Euclidean space $\Re^n$. Given the angle of the X-ray projection, $\theta \in S^{n-1}$, where θ is an element of (n-1)-Sphere, and $s \in \Re$, where *s* is the real number distance of the projection line from the origin of the phantom, the value of the Radon transform of *f* on the hyperplane, $\langle \theta, x \rangle = s$, is

$$Rf(\theta, s) = \int_{\langle \theta, x \rangle = s} f(x)dx \,. \tag{3}$$

θ direction is a unit vector that denotes the direction made by the motion of the source detector and is orthogonal to the direction of the vector *x*, whose $\langle \theta, x \rangle = s$ shows a projection line perpendicular to the θ line at a distance *s* from the phantom's origin. In Figure 20, the projection line pointing from the source to the detector is perpendicular to θ. Figure 21 is a mathematical illustration of the unit Sphere and 2-Sphere in 2D and 3D Euclidean real space, respectively, and the projection line and projection plane a distance *p* from the origin.

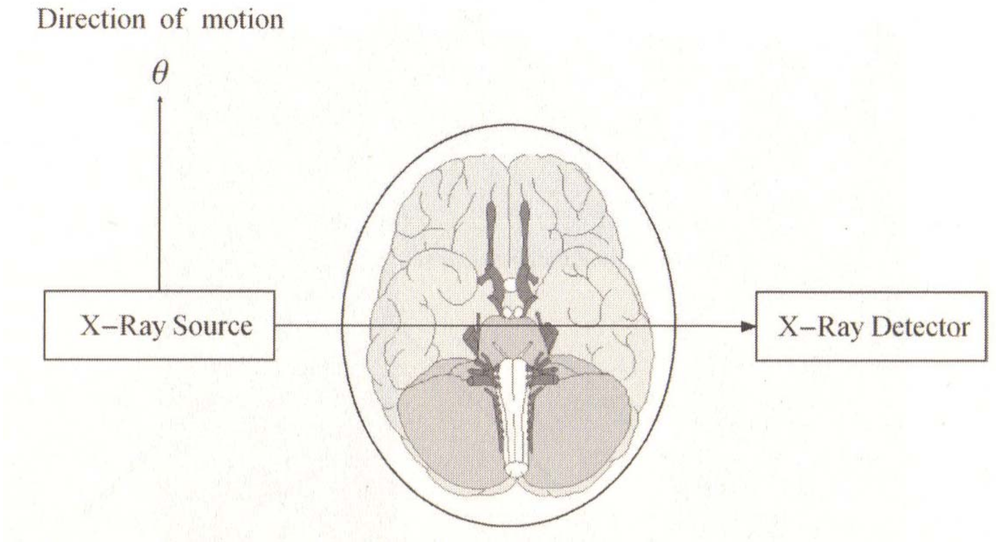

Figure 20: The ray between the source and detector is the projection line situated at a distance *s* (not shown) from the origin of (n-1)-Sphere.

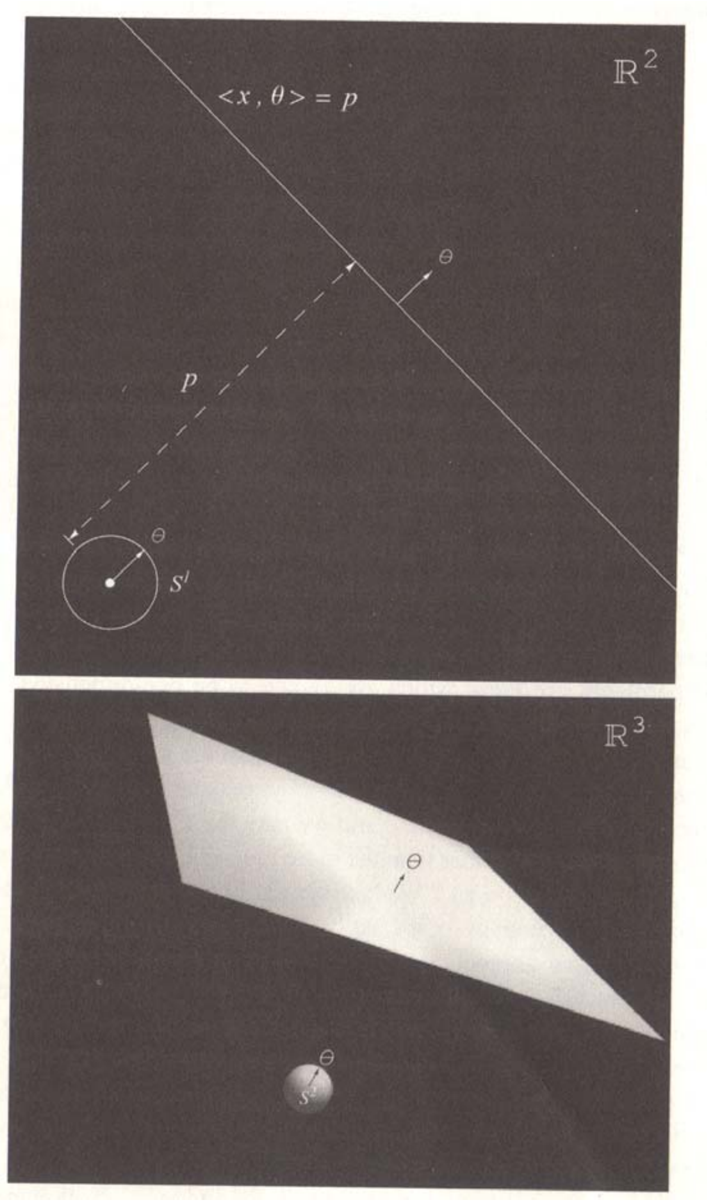

Figure 21: Direction of the unit vector θ as an element of *S* is always normal to the projection hyperplane (i.e. [top] projection line for S^1 and $\Re^2$ and [bottom] projection plane for S^2 and $\Re^3$).

The main method of reconstructing an unknown object such as a tumor is to use the total density values from its Radon transform and take the inverse of the transform for CT image scans. This process is called backprojection; however, taking the backprojection of the Radon transform of *f* almost always gives the Riesz potential that contributes to the errors in form of noises or artifacts, mathematically speaking. Thus the backprojection method cannot give the correct image reconstruction. But by first introducing filtering (i.e., filtered backprojection), we can eliminate these errors of each projection, and then convolution will average each filtered X-ray projection into the backprojection. Ultimately, our reconstructed image matches the original object with relatively fewer errors present. [21]

In the case of xCT, the *f* in the Radon transform is the linear absorption coefficient which varies with different points along the photon path *L*. This transform becomes a line integral, which is equal to the logarithmic ratio of the incident beam intensity to the attenuated beam intensity at a distance, *x*, from the reference point. Namely,

$$\ln\left(\frac{I_0}{I}\right) = \int_L f(x)dx\,. \tag{4}$$

The number of photons attenuates exponentially as they travel along *L*. [30]

For pCT, a slightly varied form of the Radon transform is used for image reconstruction since the protons do not travel along a straight line. We will discuss this more later on.

Theory of Coulomb Scattering

When a charged particle passes near a nucleus, it undergoes deflection from elastic scattering, which is caused by the same electric interaction between the charged particle and the Coulomb field of the nucleus. There are three types of scattering associated with the charged particle interacting with the Coulomb field: single, plural, and multiple. Single collisions are more likely to result in large angular deflections, whereas small angle deflections are caused by many collisions in multiple scattering.

Theory of multiple scattering can be treated very simply by statistical means. Starting with the differential scattering probability, [31]

$$\xi(\Theta)d\omega = 4N\frac{Z^2}{A}r_0^2\frac{\mu_e^2}{p^2\beta^2}\frac{d\omega}{\Theta^4}, \tag{5}$$

where N is the number of particles, Z atomic number, A atomic weight, $r_0 = 2.818\times10^{-13}$cm (classical electron radius), momentum p, velocity β, $d\omega$ solid angle, $\mu_e = 0.511MeV$ (electron rest energy), and Θ angle of deflection from its original direction, we calculate the mean square angle of scattering to be

$$<\theta^2>=\frac{1}{2}E_s^2\int_0^t\frac{dt'}{p^2\beta^2}, \tag{6}$$

where θ is the projection of the deflection and $E_s = \mu_e(4\pi\cdot137)^{1/2}$ is an energy constant. Given the material thickness t and assuming that energy loss is negligible, we can simplify our mean square angle of scattering:

$$<\theta^2>=\frac{1}{2}E_s^2\frac{t}{p^2\beta^2}. \tag{7}$$

Applying similar technique, our mean square displacement without energy loss is

$$<y^2>=\frac{1}{6}\frac{E_s^2}{p^2\beta^2}t^3=\frac{1}{3}t^2<\theta^2>. \tag{8}$$

Fermi arrived to the same answers for the mean square angle and mean square displacement by using a distribution function F instead of the differential scattering probability. Starting with the differential equation,

$$\frac{\partial F}{\partial t}=-\theta\frac{\partial F}{\partial y}+\frac{1}{w^2}\frac{\partial^2 F}{\partial\theta^2}\text{, where } w=\frac{2p\beta}{E_s} \tag{9}$$

he obtained the distribution function:

$$F(t,y,\theta)=\frac{\sqrt{3}w^2}{2\pi t^2}\exp\left[-w^2\left(\frac{\theta^2}{t}-\frac{3y\theta}{t^2}+\frac{3y^2}{t^3}\right)\right]. \tag{10}$$

By integrating F over y, one obtains an angular distribution irrespective to the lateral displacement:

$$\int_{-\infty}^{\infty}F(t,y,\theta)dy=\frac{w}{2\sqrt{\pi}t^{1/2}}\exp\left[-\frac{1}{4}\frac{w^2\theta^2}{t}\right]. \tag{11}$$

Similarly, by integrating the function over the angle, one obtains a lateral distribution irrespective to the angle:

$$\int_{-\infty}^{\infty}F(t,y,\theta)d\theta=\frac{\sqrt{3}w}{2\sqrt{\pi}t^{3/2}}\exp\left[-\frac{3}{4}\frac{w^2y^2}{t^3}\right]. \tag{12}$$

Since we have factored out energy loss and these distributions are Gaussian, we can find the variances for the angular and lateral, which will give us the mean square for each of the parameter. Hence,

$$\sigma_\theta^2=<\theta^2>=\frac{1}{2}E_s^2\frac{t}{p^2\beta^2}, \tag{13}$$

same as (7), and

$$\sigma_y^2 = <y^2> = \frac{1}{6}\frac{E_s^2}{p^2\beta^2}t^3 = \frac{1}{3}t^2 <\theta^2>, \tag{14}$$

same as (8). [31]

Eyges derived a different distribution function from the same differential equation (9) to take energy loss into account:

$$F(t,y,\theta) = \frac{1}{2\pi(B(t))^{1/2}}\exp(-\frac{\theta^2 A_2 - 2y\theta A_1 + y^2 A_0}{4A_0 B}), \tag{15}$$

where

$$B(t) = A_0 A_2 - A_1^2, \tag{16}$$

$$A_0(t) = \int_0^t \frac{d\eta}{W^2(\eta)}, \tag{17}$$

$$A_1(t) = \int_0^t \frac{(t-\eta)}{W^2(\eta)}d\eta, \tag{18}$$

$$A_2(t) = \int_0^t \frac{(t-\eta)^2}{W^2(\eta)}d\eta. \tag{19}$$

W has the same expression as w in Fermi's distribution, but momentum p and velocity β in W are no longer constants because of energy loss along the distance increment $d\eta$. Thus, we obtain the angular distribution independent to lateral displacement and lateral distribution independent to angle:

$$\int_{-\infty}^{\infty} F(t,y,\theta)dy = \frac{1}{2\sqrt{\pi A_0}}\exp[-\frac{\theta^2}{4A_0}] \tag{20}$$

and

$$\int_{-\infty}^{\infty} F(t, y, \theta) d\theta = \frac{1}{2\sqrt{\pi A_2}} \exp[-\frac{y^2}{4A_2}]. \tag{21}$$

If we then take the angular and lateral variances, we get

$$\sigma_\theta^2 = 2\, A_0 \tag{22}$$

and

$$\sigma_y^2 = 2\, A_2\,. \tag{23}$$

Unlike (13) and (14), the values of (22) and (23) depend on the change of the particle’s momentum and velocity. [32]

Correcting the Tail Ends of the Distribution

As we have seen in the previous section, we assumed the negligible energy loss effects of the MCS yield Gaussian distributions for the mean square angle of scattering and mean square lateral displacement. But in reality the angular distribution of the MCS has much larger tails than those of the Gaussian, because there are very few (single scattering) protons deflected at very large angles from atomic electrons contributing to small, negligible energy losses of the MCS.

Attempts to achieve a close Gaussian representation to the scattering angle distribution involved a maximum likelihood fit by truncating the large tail ends of the scattering curve. [33] A data set for measured angular distribution that reflects this scattering curve was fitted with Molière distribution and with Gaussian distribution. As expected both Molière and Gaussian perfectly to coincide with each other in the central, small-angle scattering region of the angular distribution. [34]

Highland introduced a logarithmic correction term to take the tail end distribution into account. The term added a correction to the standard deviation of the Gaussian distribution, which would delineate the Molière distribution that has the higher tail ends. It was not until recently that the Particle Data Group agreed that the Highland correction term for the standard deviation would be

$$\sigma(l,E) = \frac{13.6\,\frac{MeV}{c}}{\beta(E)p(E)}\sqrt{\frac{l}{X}}\left[1 + 0.038\ln\left(\frac{l}{X}\right)\right], \tag{24}$$

where E, β, and p are the energy, ratio of the proton speed to light speed, and proton momentum. X is the radiation length of the phantom, and l is the proton path length. [35]

Physics of pCT

The physics behind pCT is overall the same as the one mentioned for the previous proton therapy section. However, in this section we emphasize particular physical concepts that serve as the fundamentals of pCT and are important to its development.

The two main interactions that affect pCT the most are the Coulomb interaction with atomic electrons and Coulomb interaction with the positively charged nuclei. As the protons travel through matter, they lose most of their initial kinetic energy via inelastic collisions with atomic electrons, which result in ionizations or excitations of the atoms. Also during their traversal, they will elastically collide with the nuclei and be deflected, causing multiple small-angle scatterings with negligible energy loss.

When each of the several protons individually undergoes these interactions, there is a statistical distribution of the amount of energy loss and lateral and angular displacement of the proton from its incident direction. The collisions with electrons contribute to the energy loss of each proton traversing a bulk matter of given thickness, whereas the lateral and angular displacements are the effect of MCS between protons and the nuclei.

On some occasions, protons can undergo inelastic nuclear interactions, which further reduce proton transmission through the material. As mentioned, these protons mostly deposit their energy, contributing to the dose within the patient and nothing to the image formation. [22]

The amount of energy required to precisely position the Bragg peak at the tumor involves understanding the tissue density through which the protons will traverse. The compositions of human soft tissues are primarily atoms with relatively low atomic number Z and weight A. Their ratio Z/A varies little within the range of 0.5 and 0.55. Pronounced density differences are evident in compact bone tissue, which is 80% denser than muscle, and in adipose tissue, about 12% less dense than muscle. Otherwise, density differences between various soft tissues are in the order of a few percentages.

Using the NIST PSTAR database, 200 MeV protons have a CSDA range of 25.8 cm in an A150 tissue equivalent, shown in Figure 22, which can sufficiently penetrate an average adult skull; 250 MeV protons have a 37.7 cm range, a sizeable penetration depth for an adult trunk.

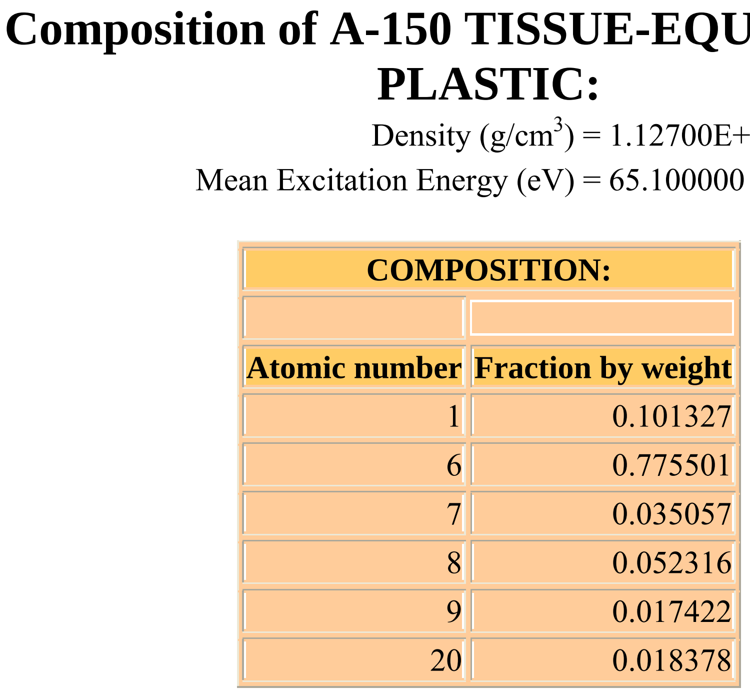

Composition of A-150 TISSUE-EQUIVALENT PLASTIC:

Density (g/cm^3) = 1.12700E+00

Mean Excitation Energy (eV) = 65.100000

COMPOSITION:	
Atomic number	**Fraction by weight**
1	0.101327
6	0.775501
7	0.035057
8	0.052316
9	0.017422
20	0.018378

Figure 22: Composition and its ratio that constitute this tissue-equivalent plastic commonly used for experimental microdosimetry. [36]

In pCT, the stopping power is the mean energy loss of protons per unit path length for protons with initial energies between 10 – 250 MeV. It is expressed by the Bethe-Bloch formula,

$$-\frac{dE(\mathbf{r})}{dx} = \eta_e(\mathbf{r}) S(I(\mathbf{r}), E(\mathbf{r})), \tag{25}$$

where η_e is the relative electron density with respect to water, $I(\mathbf{r})$ the mean excitation potential of the material, $E(\mathbf{r})$ proton energy, and S proton stopping power in water.

$$S(I(\mathbf{r}),E(\mathbf{r})) = K\frac{1}{\beta^2(E)}\left[\ln\left(\frac{2m_ec^2\beta^2(E)}{I(\mathbf{r})}\frac{1}{1-\beta^2(E)}\right) - \beta^2(E)\right], \qquad (26)$$

where m_e is the electron mass, β the proton velocity relative to the speed of light, and $K = 4\pi r_e^2 m_e c^2 \rho_{e,water} = 0.170 MeV/cm$. r_e is the classical electron radius of 2.818×10^{-13} cm, $m_ec^2 = 0.511MeV$ is the electron rest energy, and $\rho_{e,water} = 3.343\times10^{23} electrons/cm^3$ is the volume electron density of water. The stopping power is used to determine the mean energy of the incident protons after traveling a homogeneous water phantom. A more appropriate form d of the general Radon integral (2) for pCT,

$$d = \int_{E_{in}}^{E_{out}} \frac{1}{S(I,E)} dE, \qquad (27)$$

gives the layer thickness of the homogeneous water. It will later be shown that d is also the path integral of the relative volume electron density, which will exhibit a mathematical relationship between energy loss and electron density resolution. [22]

Unlike energy loss due to straggling, which will be discussed in the following section, the mean energy loss can be adjusted by changing the thickness or density of the medium or the initial beam energy.

In the proton Coulomb interaction with atomic electrons, the proton exhibits an energy distribution that can be described either by a Gaussian distribution if the energy loss does not exceed 20% of its initial energy or by a skewed non-Gaussian energy loss distribution with tail ends if the energy loss does exceed 20%.

Energy loss below 20% of the initial kinetic energy displays a Gaussian distribution curve fit if we assume the central limit theorem applies where the frequency of energy losses is large. According to Bohr's theory, the variance of this energy loss distribution is

$$\sigma_B^2(d) = \eta_e K \int_0^d \frac{1 - \frac{1}{2}\beta^2(E(E_{in}, x))}{1 - \beta^2(E(E_{in}, x))} dx\,, \tag{28}$$

where $E(E_{in}, x)$ is the mean energy of protons with different initial energies E_{in} given a path length x through the material. The first two moments of the distribution, $E_1 =< (E_{in} - E) >$ and $E_2 =< (E_{in} - E)^2 >$, are not zero. The second moment is the variance (4). Higher order moments are ignored.

For energy losses above 20% of incident energy, Tschalar's theory takes account of the higher order moment terms (i.e., $E_n =< (E_{in} - E)^n >$, where $n > 2$) that contribute to the skewed non-Gaussian distribution and its developing end tails. The variance of this energy loss distribution is expressed by a differential equation,

$$\frac{d}{dx}\sigma_T^2(x) = \kappa_2(x) - 2\left(\frac{d}{dE}\kappa_1(E(x))\right)\sigma_T^2 + \textit{higher order terms}, \tag{29}$$

where

$$\kappa_2 = \eta_e K \frac{1 - \frac{1}{2}\beta^2(E(E_{in}, x))}{1 - \beta^2(E(E_{in}, x))} \tag{30}$$

and $\kappa_1(E(x))$ is identical to (1). These *higher order terms* are higher order derivatives of $\kappa_1(E(x))$ with respect to energy. [22]

The thesis uses a fan beam of protons with initial energy of 200 MeV with mean energy losses greater than 40 MeV after their traversal in the material. For this case, Tschalar's theory provided a more accurate analytical estimate of the energy loss spread of a proton traversing a homogeneous water phantom than Bohr's. [22]

Aside from these equations describing the energy loss due to straggling, the physical meaning of straggling indicates that after the protons collide with the electrons, they randomly move in their continued paths. One proton may undergo more collisions and travel less far in its range than its counterparts before it completely stops. Consequently, there will be small variation in the proton ranges (or energy-loss variation in pCT), known as straggling. We ascribe the straggling to the statistical fluctuations represented by the tails of the skewed and Gaussian distribution curves. Last, it is important to note that energy-loss variation is the physical limiting factor of relative electron density resolution.

Within a given energy range for pCT, protons traversing through a material encounter multiple small-angle deflections (or MCS) due to proton-nuclei elastic collision. The nuclear potential of the material atoms causes the protons to scatter in this Coulomb interaction, leading to random macroscopic deviation from the protons' initial (entry) direction and initial (entry) lateral displacement. The resulting exit direction and exit lateral displacement are changed by a few degrees and up to a few millimeters respectively.

MCS is the physical limiting factor for the spatial resolution of imaging. It contributes a small, random increase in the proton path length in a given material thickness. [22]

The inelastic nuclear interactions of protons lead to an almost complete loss of the incident protons. The probability of these interactions becomes significant when the incident energy is above 100 MeV. The collided protons lose most their energy as the material thickness increases, and this energy contributes to the unwanted dosage in the patient.

The number of protons decreases exponentially along their traversed path. Using the CSDA range, the proton fluence can be expressed as

$$\Phi(x) = \Phi_0 \exp(-\kappa x)\,. \tag{31}$$

κ is the total inelastic macroscopic cross section of the protons in water.

Primary protons transfer a fraction of their initial kinetic energy to the secondary protons and occasionally to the heavily charged atoms. Incident protons with energy range from 100 – 250 MeV have a fractional range from 0.62 – 0.67 when colliding with an oxygen nuclei. The remaining initial energy is transferred to neutrons and photons, which do not contribute to additional patient dose. The heavily charged atoms deposit their dose while the secondary protons, mostly with kinetic energies less than 10 MeV, continue to travel. Some of these protons will leave the material and be used to reconstruct the image. [22]

Chapter 2

CONCEPTUAL MODEL OF pCT

pCT Setup

Before servicing pCT onto animate objects in clinical trials, a pCT experimental setup is necessary to assess its efficiency as a diagnostic imaging tool. The theory that the protons exhibit an approximate Gaussian distribution of their lateral and angular displacements and the energy loss due to straggling is less than the mean energy loss presumes the protons’ ability to image tissues.

In the design of a pCT scanner, a phantom serves as an object or a target which the protons image. The construction of a phantom involves engineering its material composition in order to imitate any body tissues of a patient such as air, bone, and water. For example, the polymethilmetacrylate-PMMA represents a tissue-equivalent homogeneous water phantom. [25]

An imaged phantom is placed between two silicon strip detectors (SSD) which measure the entry and exit positions and the entry and exit angles of individual protons. The incident proton beam may not necessarily be parallel upon hitting the first SSD. The SSD can also record the positions and directions of the protons travelling within the phantom. A calorimeter composed of a multi-array of crystal scintillators placed behind the rear SSD measures the proton exit energy and stops the proton from travelling farther. These scintillators will convert the proton-induced ionizations into scintillation light, which will be collected by photomultiplier tubes or photodiodes. The collection of light will produce an electrical readout and then be digitized by a computer cluster which will perform an image reconstruction using reconstruction algorithms. [26]

Figure 23 shows the pCT setup used at Loma Linda University Medical Center with the collaboration of University of California Santa Cruz Institute of Particle Physics, and Northern Illinois University. [24]

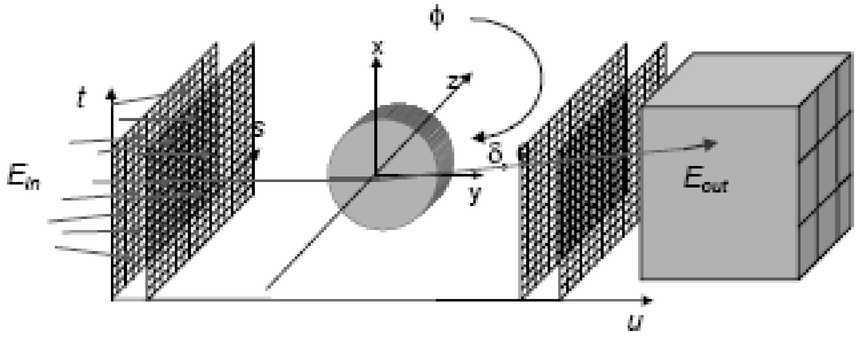

Figure 23: Schematic of the proposed pCT system. Protons with incident energy E_{in} are recorded individually in the detector reference system (*s, t, u*) as they traverse the imaged object from several different projection angles ϕ. Entry and exit positions and entry and exit angles are recorded by the detector planes as exit energy E_{out} by the scintillator arrays of the energy calorimeter. [26]

Figure 24 resembles our desired goal of this setup – the clinical use of pCT.

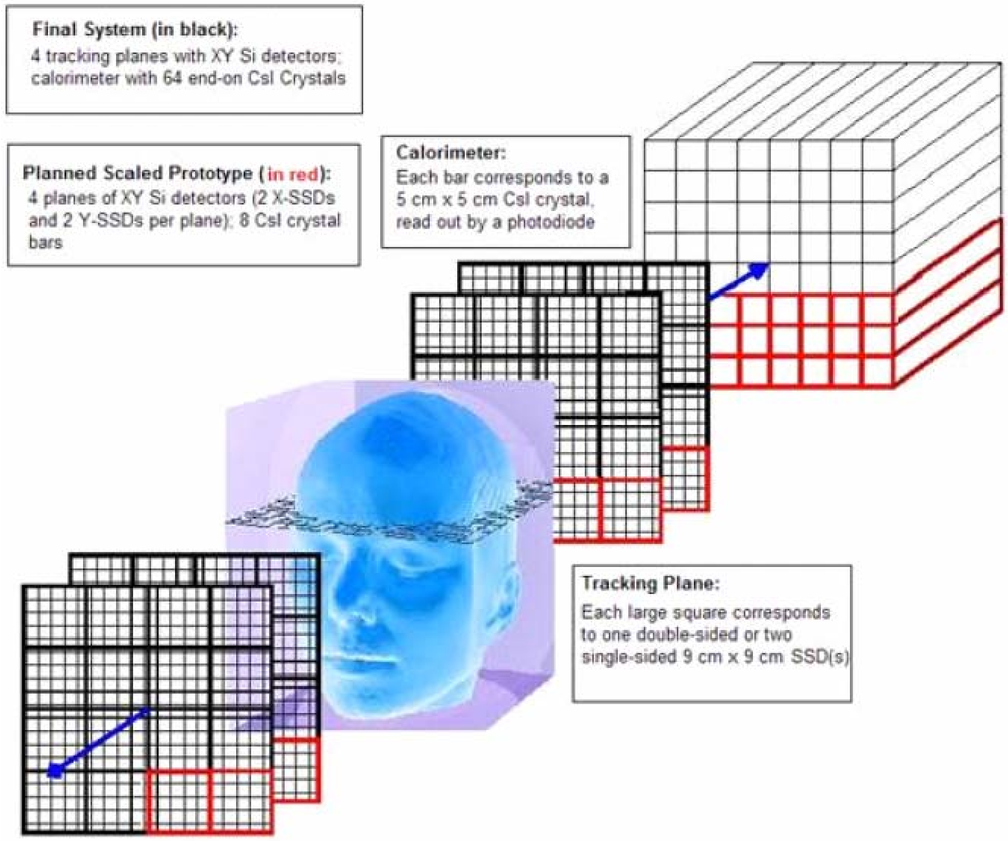

Figure 24: This picture includes a human head phantom for a pCT scanning system. Four planes of positive sensitive SSD (single-sided SSD) measure the position and direction of traversing protons. CsI crystal calorimeter measures the proton energy of the outgoing protons. For a complete scan, the SSDs and the calorimeter system rotate about the longitudinal axis of the patient at different projection angles. [24]

Specifications of Detectors

There are two principal types of silicon detectors that are used for tracking purposes: silicon strip detectors (SSD) and silicon pixel detectors (SPD). A double-sided SSD (D-SSD) and SPD are frequently used in tracking because of their 2-D position sensitivity. That is, each side of a detector can record the x- or y-coordinate position of an incident particle.

The advantages of using D-SSD are minimum readout channel numbers, minimum radiation length, and less than 50 ns of fast charge collection time. However, its disadvantages include the complex and expensive two-sided manufacturing process of each detector, the radiation softness of the detector due to its complex n-side structure, multi-hit ambiguity when two or more protons hit a detector simultaneously, and the required two polarities in readout electronics.

For the SPD, the 2-D position sensitivity, the single-sided process, no multi-hit ambiguity, and fast charge collection time of about 50 ns are some of its advantages in tracking. However, like the D-SSD, the large readout electronic channels, complicated bumper bonding between detector chip and readout electronics chip, the additional radiation length due to the readout chip, the limited position resolution by the minimum size of the bumper bonding pads, and the high overall cost pose certain disadvantages of using SPD for pCT.

Since the disadvantages of these two detectors make them less suitable for pCT tracking, a silicon stripixel detector (SSPD) has been fabricated in order to combine the advantages of the D-SSD and SPD but with the remaining disadvantage of a multi-hit ambiguity as that of D-SSD. Each SSPD pixel is divided by X- and Y-cell, which are respectively projected and read out by X and Y strips. These cells are interleaved with a maximum distance of less than 20 μm to effect the resulting charge sharing between the two cells for each proton hit. With 2-D position sensitivity and a simpler single-sided process, the SSPD has become suitable for pCT. [26]

Energy Detector

The important parameter of the proton exit energy affects the relative volume electron density resolution of pCT. Hence, the preponderance of a reliable energy detector contributes significantly to pCT image quality.

Because the proton stopping power, $\frac{dE}{dx}$, does not strongly depend on the proton energy, the position-sensitive SSPD cannot be used to measure the proton energy output via $\frac{dE}{dx}$ measurements. An indispensable separate calorimeter detects the energy output. With its crystal scintillator array, this calorimeter converts any ionization, induced by protons inelastically colliding with atomic electrons, to light. The result of using a calorimeter may determine the exit energy of a single proton to better than 1% accuracy. Table 1 shows the types of scintillators suitable for pCT.

The role of the photodiode is to convert light from the scintillator to current for electronic readout via photoelectron production. These photoelectrons contribute to the statistical uncertainty of the calorimeter energy output with an energy resolution of less than 1% for 200 MeV protons. A minimum of 10^4 photoelectrons is needed to achieve this resolution with adequate light yield, which can be obtained by the CsI, BGO, and LSO scintillators. Since photodiodes are less sensitive to magnetic fields than photomultiplier tubes, they are more preferable in pCT. [26]

Table 1

Characteristics of Crystal Scintillators Suitable for pCT Applications

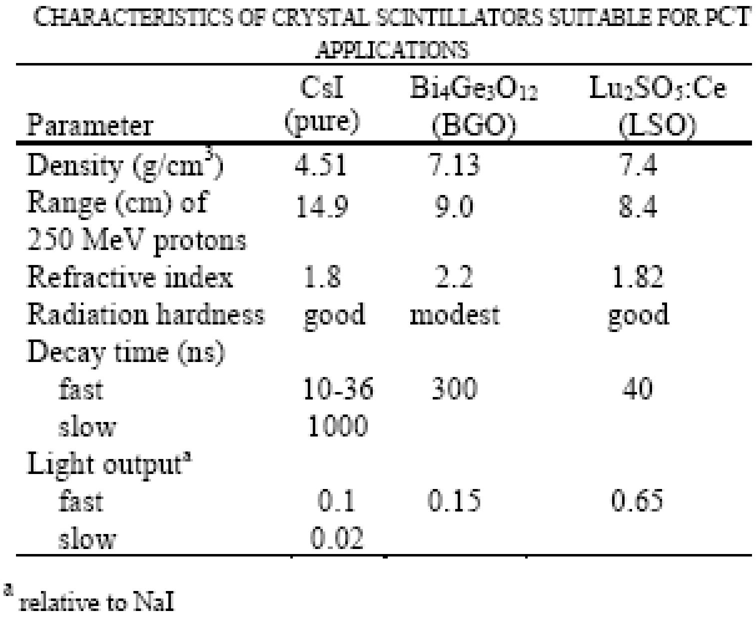

CHARACTERISTICS OF CRYSTAL SCINTILLATORS SUITABLE FOR PCT APPLICATIONS

Parameter	CsI (pure)	$Bi_4Ge_3O_{12}$ (BGO)	Lu_2SO_5:Ce (LSO)
Density (g/cm^3)	4.51	7.13	7.4
Range (cm) of 250 MeV protons	14.9	9.0	8.4
Refractive index	1.8	2.2	1.82
Radiation hardness	good	modest	good
Decay time (ns)			
fast	10-36	300	40
slow	1000		
Light output[a]			
fast	0.1	0.15	0.65
slow	0.02		

[a] relative to NaI

Proton’s Most Likely Path and Image Reconstruction of pCT

Achieving the goals of pCT revolves around the successful reconstructions of the most likely path or the maximum likelihood path (MLP) of protons traversing through a target and the subsequent electron density of the target which is used to delineate the target’s anatomic features via image representation. The significance of the MLP contributes much to improving the spatial resolution of pCT, which is physically affected by the MCS of protons. Although the MLP formalism has been proposed to suit the case of the homogeneous water phantom, simulations are needed to test this analytical MLP formula in cases of inhomogeneous phantoms, where water is not the only material present in the phantom. The methods of reconstructing the MLP and the electron density are complex in their scope. Ultimately, improving these two reconstructions produces a favorable outcome of our pCT image qualities. This thesis focuses only on the MLP reconstruction.

Reconstructing the Proton’s Most Likely Path for pCT

Accurately reconstructing each individual proton path in a phantom becomes important. The physical interaction of protons with matter is the main reason that makes exact reconstruction of individual proton paths nearly impossible. In addition, the vast number of protons (~10^8) required for pCT would make the computing time for path reconstruction great and quite impractical for clinical use. Despite these difficulties, the small angle scattering of the MCS makes the approximation of the MLP a possibility. Having a close-to-the-exact path reconstruction, if achieved, will render better spatial resolution which results in finer details of the anatomic structures being diagnostically imaged.

A method devised for reconstructing the MLP will be discussed later in the MLP formalism.

Reconstructing the Image for pCT

The process of reconstructing an image utilizes a relationship between the mean energy loss of the traversed protons and the line integral transform, whose origins in xCT were discussed in the "Physics of pCT" section.

In pCT the goal of this relationship is to obtain the line integral of the relative electron density and the electron density itself by integrating the reciprocal of the stopping power, starting from the Bethe-Bloch equation (26), in respect to the change in energy between the incident and the outgoing proton energy along the proton's path *L*, which is the MLP:

$$\int_{E_{in}}^{E_{out}} \frac{dE}{S(I_{water}, E)} = \int_L \eta_e(\mathbf{r})dl. \tag{32}$$

The spatially dependent mean excitation potential $I(\mathbf{r})$ from (26) has been replaced by the constant mean excitation potential of water, which is 75 eV. The right-hand side of (32) would be similar to the Radon transform if the MLP of the protons were straight and confined in a 2D plane.

The proton energy losses measured by the scintillator are converted into approximate line integrals of η_e. The reconstruction of density resolution can be carried out by the filtered backprojection algorithms for the first-order straight line approximation of (32). [22] But in the case of higher order nonlinear paths, algebraic reconstruction technique (ART) algorithms can reconstruct 3D electron density maps without using the conversion function. The maps can accurately predict the proton dose distribution within the patient. Spatial resolution by employing ART is much better than that by the transform methods like filtered backprojection because algebraic techniques can correct for the nonlinear paths in the density resolution and include "the *a priori* knowledge about the object to be reconstructed." The downside to ART and other iterative techniques is the enormous computation time. There have been continuing pCT studies that aim on shortening the reconstruction time with the production of an optimal image. Some investigations have been utilizing parallel computing to develop parallel-running iterative projection algorithms for fast reconstruction over multiple computer processors. These algorithms such as block-iterative component averaging and diagonally relaxed orthogonal projections have shown greater potential for quick optimal image building than the inherently sequential ART. [37] Unfortunately, we will not discuss the properties of the image reconstruction algorithms in detail, though they have become crucial for pCT.

Description of the MLP Formalism

In order to improve the spatial resolution of pCT, MLP formalisms have been developed to assume the entry and exit information consists of positional and angular parameters with respect to the object. Scanner designs use SSD to measure the position and direction of before and after the protons traverse the object. [26] Initially, a formula was derived for transmission proton radiography with the measured angle and positions of the proton trajectory. [38] Years later, the χ^2 estimator was introduced to solve the expressions for lateral displacement and direction that will minimize it by setting the χ^2 derivative to zero. The resulting lateral and angular deviation from the measured entry parameters will give proton MLP. [39] Afterwards a more flexible and compact matrix-based version of the χ^2-derived MLP formalism was developed by employing Bayesian statistics. These MLP formalisms are mathematically equivalent, and they assume uniform water density throughout the reconstruction volume. [40]

The analytical MLP, which assumes a homogeneous water phantom, is constructed from the MLP formalism and compared with the actual paths of Geant4 Monte Carlo simulated protons traversing different inhomogeneous phantoms consisting of slabs of air, bone, and water such as in Figure 25. The materials in the phantoms are representative of the inhomogeneities of the human body in terms of tissue-equivalent densities. The goal of this thesis is to quantitatively describe the typical inhomogeneities of the human body via simulated phantoms and their effect on the accuracy of the MLP formalism in order to test the validity of the analytical MLP, assumed for homogeneous water, under inhomogeneous conditions.

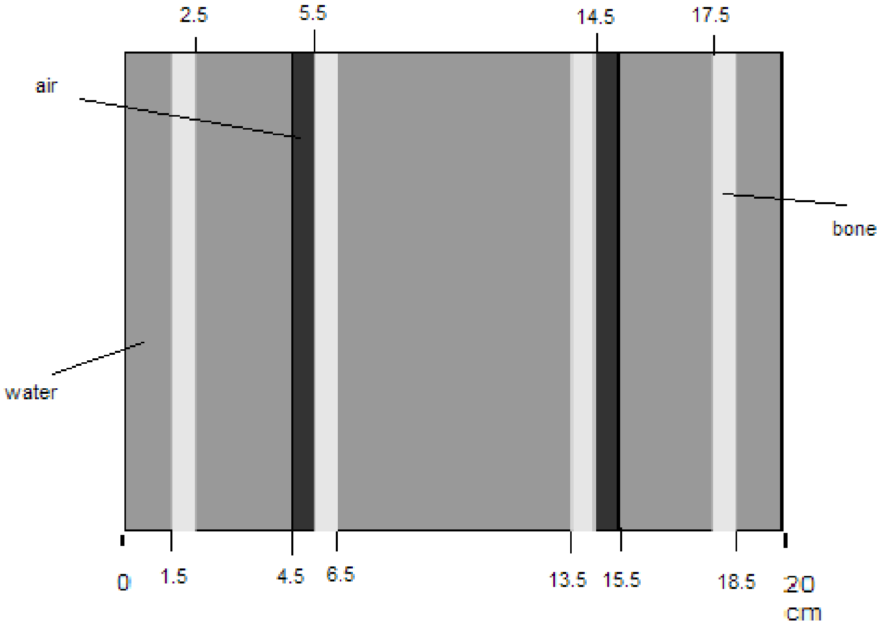

Figure 25: Inhomogeneous phantom with four 1 cm bone slabs (lightly shaded), two 1 cm air slabs (darkly shaded), and five intervening water slabs (intermediately shaded). [41]

Knowing the entry and exit lateral displacements – orthogonal to the horizontal depth position – and entry and exit directions, we can estimate lateral displacement and direction at any intermediate depth in the phantom. In reality, proton scattering will be 3D, but we can assume that the small angular deviation, with respect to the beam axis, is in one orthogonal plane and that in the other are two independent statistical processes. Hence we can derive our matrix-based 2D MLP in one plane such as the one shown in Figure 26.

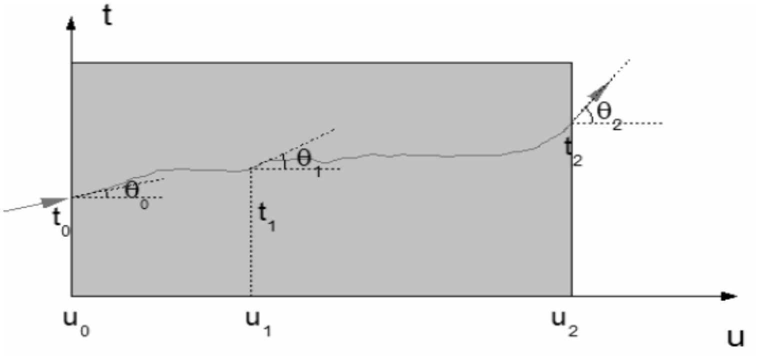

Figure 26: Geometry of a proton path through an object in the *t-u* plane. The *t-u* coordinate system is determined by the external silicon tracking detectors. A proton enters from the left with known lateral displacement and direction and exits the object after traversing a depth $u_2 - u_0$ with known exit location and angle. The lateral displacement t_1 and direction θ_1 at an intermediate depth u_1 are unknown, but its most likely values can be calculated using Bayes' law. The entirety of locations and directions inside the object yields the MLP in the *t-u* plane.

In the derivation, y_1 is a parameter vector of the lateral displacement t_1 and direction θ_1 at an intermediate depth u_1:

$$y_1 = \begin{pmatrix} t_1 \\ \theta_1 \end{pmatrix}. \tag{33}$$

Our 2D compact matrix-based MLP from the known displacements and directions is,

$$y_{MLP} = \left(\Sigma_1^{-1} + R_1^T \Sigma_2^{-1} R_1\right)^{-1} \left(\Sigma_1^{-1} R_0 y_0 + R_1^T \Sigma_2^{-1} y_2\right), \tag{34}$$

where

$$\Sigma_1 = \begin{pmatrix} \sigma_{t_1}^2 & \sigma_{t_1\theta_1}^2 \\ \sigma_{t_1\theta_1}^2 & \sigma_{\theta_1}^2 \end{pmatrix}, \tag{35}$$

$$\Sigma_2 = \begin{pmatrix} \sigma_{t_2}^2 & \sigma_{t_2\theta_2}^2 \\ \sigma_{t_2\theta_2}^2 & \sigma_{\theta_2}^2 \end{pmatrix}, \tag{36}$$

$$R_0 = \begin{pmatrix} 1 & u_1 - u_0 \\ 0 & 1 \end{pmatrix}, \tag{37}$$

$$R_1 = \begin{pmatrix} 1 & u_2 - u_1 \\ 0 & 1 \end{pmatrix}, \tag{38}$$

$$y_0 = \begin{pmatrix} t_0 \\ \theta_0 \end{pmatrix}, \tag{39}$$

and

$$y_2 = \begin{pmatrix} t_2 \\ \theta_2 \end{pmatrix}. \tag{40}$$

y_{MLP} is the trajectory $y_1 = \begin{pmatrix} t_1 \\ \theta_1 \end{pmatrix}$ that maximizes the posterior likelihood of the proton with lateral displacement t_1 and direction θ_1 at an intermediate depth u_1 given the known entry parameters y_0 at entry depth u_0 (set to 0 cm) and exit parameters y_2 at exit depth u_2 (set to 20 cm), as shown in Figure 26. Σ_1 and Σ_2 are variance-covariance scattering matrices defined at any depth from 0 to u_1 and u_1 to 20cm, respectively. These matrix elements of variances and covariances of t and θ are the following:

$$\sigma_{t_1}^2(u_1) = \Theta_0^2 \int_0^{u_1} \frac{(u_1 - u)^2}{\beta^2(u) p^2(u)} \frac{du}{X_0}, \tag{41}$$

$$\sigma_{\theta_1}^2(u_1) = \Theta_0^2 \int_0^{u_1} \frac{1}{\beta^2(u) p^2(u)} \frac{du}{X_0}, \tag{42}$$

$$\sigma^2_{t_1\theta_1}(u_1) = \Theta_0^2 \int_0^{u_1} \frac{u_1 - u}{\beta^2(u)p^2(u)} \frac{du}{X_0}, \tag{43}$$

$$\sigma^2_{t_2}(u_1, u_2) = \Theta_0^2 \int_{u_1}^{u_2} \frac{(u_2 - u)^2}{\beta^2(u)p^2(u)} \frac{du}{X_0}, \tag{44}$$

$$\sigma^2_{\theta_2}(u_1, u_2) = \Theta_0^2 \int_{u_1}^{u_2} \frac{1}{\beta^2(u)p^2(u)} \frac{du}{X_0}, \tag{45}$$

$$\sigma^2_{t_2\theta_2}(u_1, u_2) = \Theta_0^2 \int_{u_1}^{u_2} \frac{u_2 - u}{\beta^2(u)p^2(u)} \frac{du}{X_0}. \tag{46}$$

The constants in the integrals are Θ_0= 13.6 MeV/c and radiation length in water X_0= 36.1 cm. β is the proton's velocity relative to the speed of light, and p is its momentum. The first row, first column element of the error matrix

$$\varepsilon_{t_1\theta_1}(u_1) = 2(\Sigma_1^{-1} + R_1^T \Sigma_2^{-1} R_1)^{-1} \tag{47}$$

expresses the uncertainty in the lateral displacement at u_1.

For equations (41) to (46), a fifth-degree polynomial was fitted to the $\frac{1}{\beta^2(u)p^2(u)}$ term:

$$\frac{1}{\beta^2(u)p^2(u)} = a_0 + a_1 u + a_2 u^2 + a_3 u^3 + a_4 u^4 + a_5 u^5, \tag{48}$$

where the coefficients are [39]

$$a_0 = 7.457 \times 10^{-6} \frac{c^2}{MeV^2}, \tag{48a}$$

$$a_1 = 4.548 \times 10^{-7} \frac{c^2}{MeV^2 cm}, \tag{48b}$$

$$a_2 = -5.777 \times 10^{-8} \frac{c^2}{MeV^2 cm^2}, \tag{48c}$$

$$a_3 = 1.301 \times 10^{-8} \frac{c^2}{MeV^2 cm^3}, \tag{48d}$$

$$a_4 = -9.228 \times 10^{-10} \frac{c^2}{MeV^2 cm^4}, \tag{48e}$$

$$a_5 = 2.687 \times 10^{-11} \frac{c^2}{MeV^2 cm^5}. \tag{48f}$$

The Highland logarithmic correction factor was introduced in the later simulations, in Chapter 3, in which 12,000 random protons were selected out of 20,000. With the addition of the logarithmic term [35],

$$g(u) = \left(1 - 0.038 \ln X_0 + 0.038 \ln u\right)\left(1 - 0.038 \ln X_0 + 0.076 + 0.038 \ln u\right) \tag{49}$$

equations (41) to (46) have the term included in the integrand:

$$\sigma_{t_1}^2(u_1) = \Theta_0^2 \int_0^{u_1} \frac{g(u)(u_1 - u)^2}{\beta^2(u) p^2(u)} \frac{du}{X_0}, \tag{50}$$

$$\sigma_{\theta_1}^2(u_1) = \Theta_0^2 \int_0^{u_1} \frac{g(u)}{\beta^2(u) p^2(u)} \frac{du}{X_0}, \tag{51}$$

$$\sigma_{t_1\theta_1}^2(u_1) = \Theta_0^2 \int_0^{u_1} \frac{g(u)(u_1 - u)}{\beta^2(u) p^2(u)} \frac{du}{X_0}, \tag{52}$$

$$\sigma_{t_2}^2(u_1, u_2) = \Theta_0^2 \int_{u_1}^{u_2} \frac{g(u)(u_2 - u)^2}{\beta^2(u) p^2(u)} \frac{du}{X_0}, \tag{53}$$

$$\sigma_{\theta_2}^2(u_1, u_2) = \Theta_0^2 \int_{u_1}^{u_2} \frac{g(u)}{\beta^2(u) p^2(u)} \frac{du}{X_0}, \tag{54}$$

$$\sigma_{t_2\theta_2}^2(u_1, u_2) = \Theta_0^2 \int_{u_1}^{u_2} \frac{g(u)(u_2 - u)}{\beta^2(u) p^2(u)} \frac{du}{X_0}. \tag{55}$$

By adding the logarithmic factor, we want to observe its effects on the spatial resolution, thus the MCS, based on the simulation. We want to see whether the inclusion of the log term will make the MLP a better representation of the Geant4-generated physics data than its exclusion. It has been shown that numerical simulation with Geant4 agrees with measured data obtained from actual experiments within 0.1 mm with the same order of magnitude of spatial resolution. Simulated results have shown excellent agreement with the measured data. [42] Hence, we can use Geant4 to evaluate the validity of the log term. We assume the logarithmic term will shorten the computation time and be a better representation of the real physics.

Appendix C shows an example of a more appropriate mathematical form for computing these integrals using the fifth-degree polynomial fit via Mathematica v6.0.

For the purpose of describing our simulation method, the following plots and data of the Geant4 simulation have been taken from our earlier work. [41] The simulations from that work excluded the Highland factor.

Geant4 Simulation

The Geant4.9.1 Monte Carlo Toolkit is a platform for simulating particles through matter. Several various class libraries of high-energy physics that take physical proton interaction, beam parameters, geometry of phantom setup, and proton tracking into account are included in the simulation. These libraries in the form of header files are incorporated into the application source codes, which we use to construct phantoms with different materials through which protons pass. Geant4 pseudorandomly generates proton paths inside a constructed phantom whose proton angles and lateral displacements within the phantom and the exit energy are recorded. Examples of these header files and C++ source codes are in Appendix A and B for the _b_ab_ba_b_ (bone air-bone bone-air bone) phantom, shown in Figure 25. Each header file and its associated C++ source codes perform specific tasks that will collectively generate a simulation. These header files contain the class libraries of specific commands given in Geant4 that will imitate, in this case, a real proton beam experiment. The C++ source codes incorporate these library commands that govern these simulations and facilitate the user's manipulation of any simulation environment such as proton beam energy and dispersion, phantom geometry, phantom components, energy loss, etc. The header files are listed in Appendix A.

The simulation employs a uniform fan beam of 200 MeV mono-energetic protons incident on a 20 cm thick homogeneous equivalent water phantom shown in Figure 27. The initial fan beam spread was approximately $\pm 2.86^\circ$ resulting in a width of 16 cm at the 20 cm entry plane ($u_0 = 0$), from which the proton source was located 160 cm away. The maximum beam spread was $\pm 3.27^\circ$, whereas at the exit plane $u_2 =$ 20 cm the protons spanned the entire 20 cm width with exit directions ranging from $\pm 11.5^\circ$. Initially, 1,600 protons were randomly selected out of 19,995 histories generated from Geant4. A total of 127 histories were excluded from the sample because their exit energy and/or angle was outside a 3-sigma interval of the energy and angle of the protons from the same spatial bin. [41]

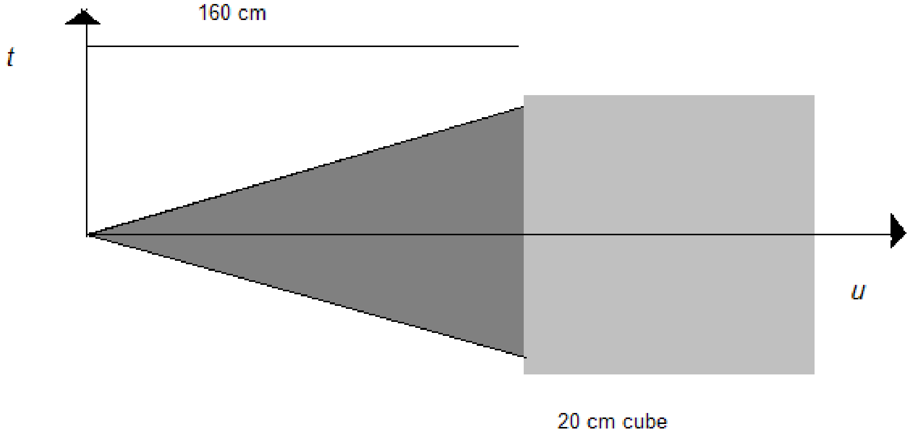

Figure 27: Proton source located 160 cm away from the entry plane of a 20 cm water cube has a spread of $\pm 2.86^{\circ}$. [41]

For each of the 1,600 protons, the 2D MLP was calculated using the formalism and the polynomial coefficients described above. In Figure 28, each MLP was subtracted from the simulated internal 3D proton track projected onto the *t*-*u* plane to obtain the individual MLP error as a function of depth.

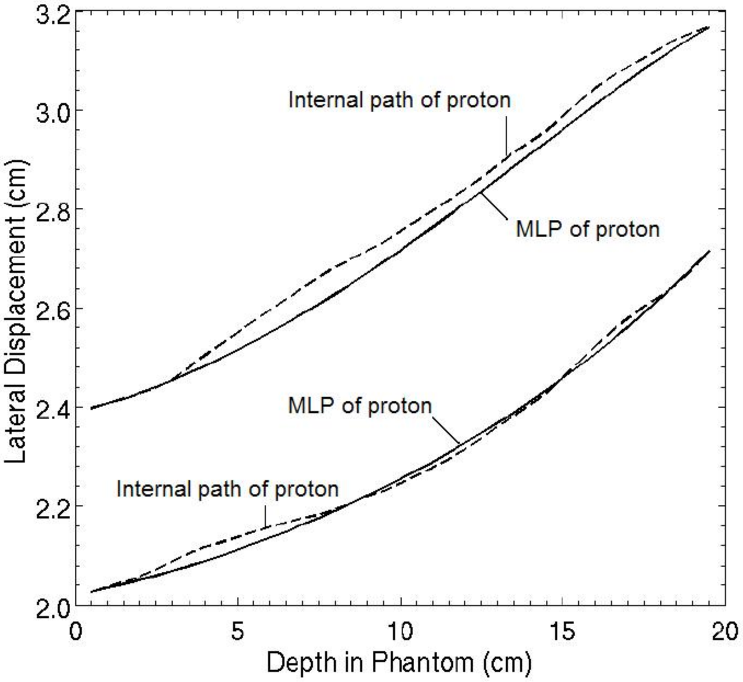

Figure 28: The MLPs and Geant4 internal paths of two simulated protons. MLP error is defined as the difference between the lateral displacement of the simulated path and the MLP of a proton traversing the 20 cm thick inhomogeneous phantom. [41]

Figure 29 shows the sample mean of MLP errors as the lower solid curve and its 95% confidence limits, as dashed lines, surrounding the mean for the inhomogeneous _b_ab_ba_b_ phantom (i.e., bone_air,bone_bone,air_bone; _ represents water slices). It also shows a pair of dotted curves representing the standard deviation or the root mean square (RMS) of the MLP errors as a function of depth in the inhomogeneous phantom and homogeneous water phantom. The RMS will evaluate the spatial resolution of our analytical MLP in the inhomogeneous phantom. A lower RMS value indicates less variability of the MLP errors and implies an improved, decreased spatial resolution, which means greater imaging accuracy. Hence the analytical MLP formalism would trace out more accurate proton paths in the inhomogeneous phantom.

The mean of the MLP errors statistically fluctuates around zero with no points lying outside the 95% confidence limit. When more protons are randomly sampled, the fluctuations become minimal. The 95% confidence limits estimate how accurately our sample mean of MLP errors with sample size *N* approximates the population mean of the Gaussian distribution, which has infinite number of samples. The 95% confidence limit is expressed as

$$SampleMean \pm 1.96\frac{\sigma}{\sqrt{N}}, \tag{56}$$

where σ is the standard deviation, which is also the root mean square (RMS). This formula explains that the population mean from the normal distribution has a 95% chance of falling within the range of $-1.96\frac{\sigma}{\sqrt{N}}$ and $+1.96\frac{\sigma}{\sqrt{N}}$ which surrounds the sample mean. If we use more protons and MLP errors as samples, that is if *N* increases, the sample mean becomes a closer approximation to the population mean. The range of the limits decreases, thus reducing statistical fluctuations.

In this case, for Figure 29, 1,600 random proton tracks and their MLPs were compared. The maximum mean MLP error (i.e., $SampleMean + 1.96\frac{\sigma}{\sqrt{N}}$) was 0.03 mm, and no sample mean error was significantly different from zero as indicated from the 95% confidence limits at any depth. This implies that the population mean is likely to be 0 mm. The standard deviations for the inhomogeneous _b_ab_ba_b_ and homogeneous water phantoms peaked at 0.6 mm and at 0.51 mm, respectively, at a depth of 12 cm. Therefore, the maximum RMS MLP error at this point was about 18% higher for the inhomogeneous than for the homogeneous water phantom. [41]

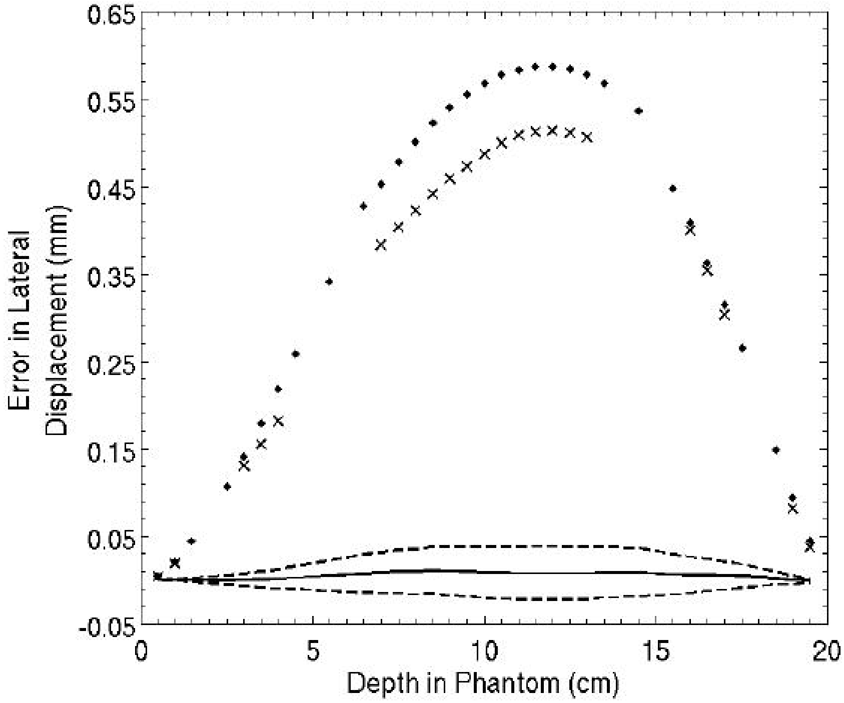

Figure 29: Mean of the MLP error shown as the lower solid line. Ninety-five percent confidence limits of the mean are displayed as the upper and lower dashed lines surrounding the mean. Upper dotted points correspond to the RMS MLP error of the inhomogeneous phantom and the lower x points to the RMS error of the homogeneous water. [41]

Figure 30 shows a G4Beamline simulation of the proton tracks through a water phantom. G4Beamline is "a particle tracking and simulation program based on the Geant4 Toolkit that is specifically designed to easily simulate beamlines and other systems using single-particle tracking." The primary advantage of this software is that the simulation does not require knowledge of the C++ programming codes and Geant4 Toolkit details while it uses the class libraries of the Geant4 Toolkit. [43]

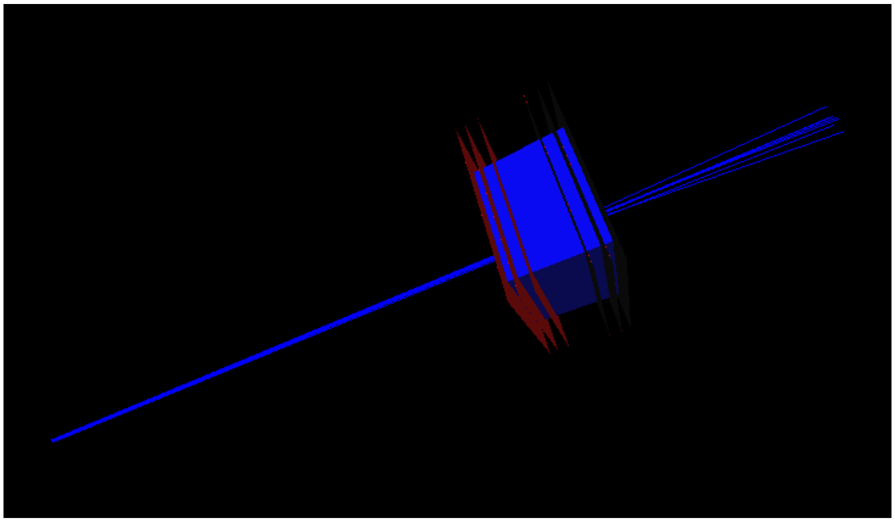

Figure 30: G4Beamline simulation of 10 proton tracks (blue), from a source at the left end, through homogeneous water cube phantom (also blue) with plane detectors (red) in a vacuum (black). Only seven protons made it through the phantom at the opposite side.

Chapter 3

RESULTS

All the simulations in this section were run with 20,000 incident protons with kinetic energy of 200 MeV. Each phantom was constructed based on different types of materials, namely air, bone and water, and their placements inside the phantom. The number of output protons varies dependent on the degree of scattering caused by the material density and thickness. We analyze the mean and the RMS of our MLP errors as a function of depth for each phantom. Appendix D contains an example source code of the mean and RMS analysis for the homogeneous water. In the process, we randomly selected 12,000 protons from the total output for most phantoms. We also computed the energy output distribution, lateral displacement, and angular distribution. An example source code is shown in Appendix E. All the simulations presented in this chapter were run with the Highland logarithmic term.

The water phantom in Figure 27 and the following constructed phantoms, Figures 31 to 62 (consisting of a water cube with material slices made of b=bone, a=air, _=water), were used in the simulation. In each caption under each phantom figure, the “position” depth refers to the location of the material slice’s center with respect to the phantom. For instance, in Figure 31, the center of the 1 cm thick air is placed at 2 cm depth of the phantom.

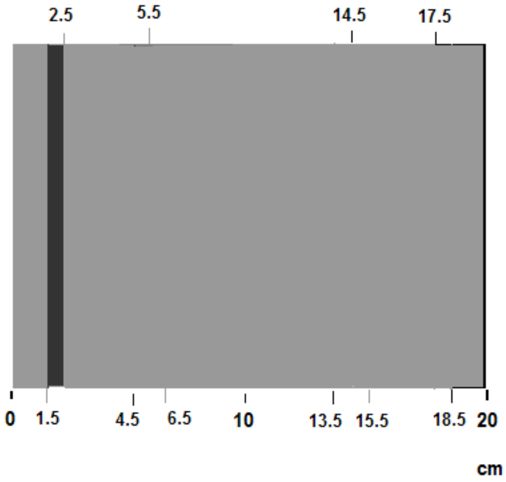

Figure 31: 1 cm thick air (black) at 2cm depth

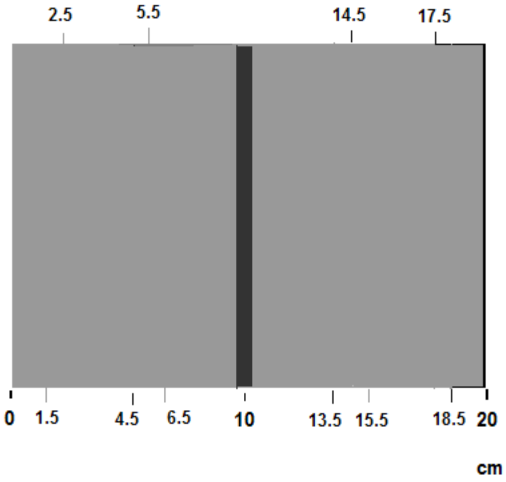

Figure 32: 1 cm thick air at 10cm depth

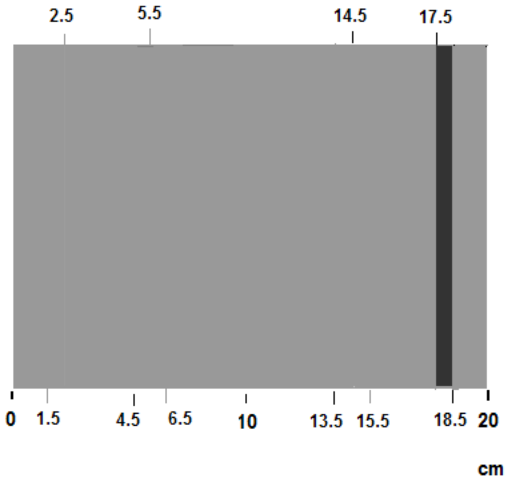

Figure 33: 1 cm thick air at 18cm depth

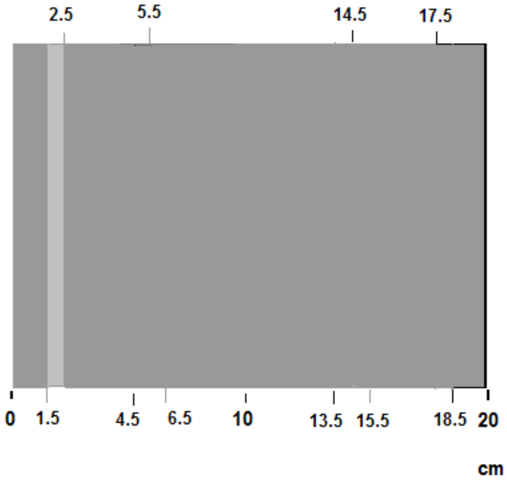

Figure 34: 1 cm thick bone (light gray) at 2cm depth

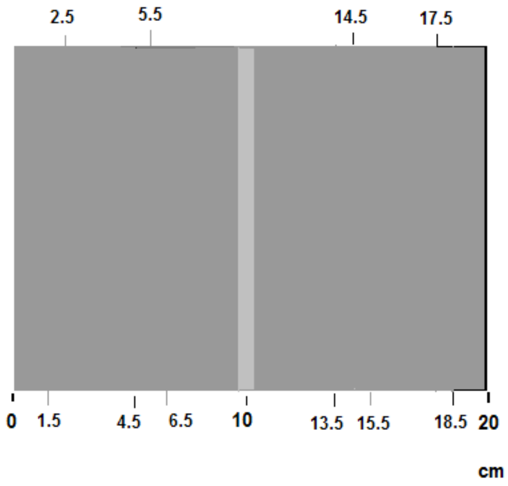

Figure 35: 1 cm thick bone at 10cm depth

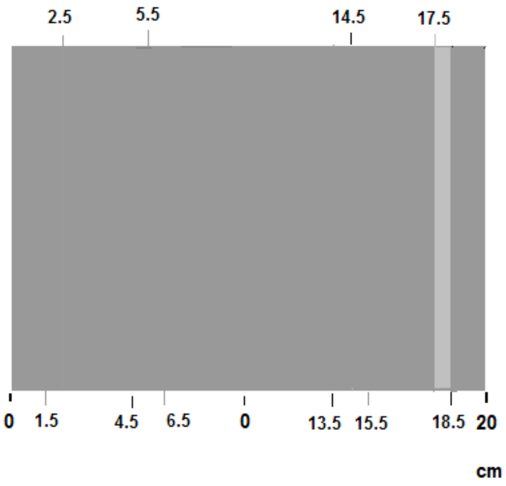

Figure 36: 1 cm thick bone at 18cm depth

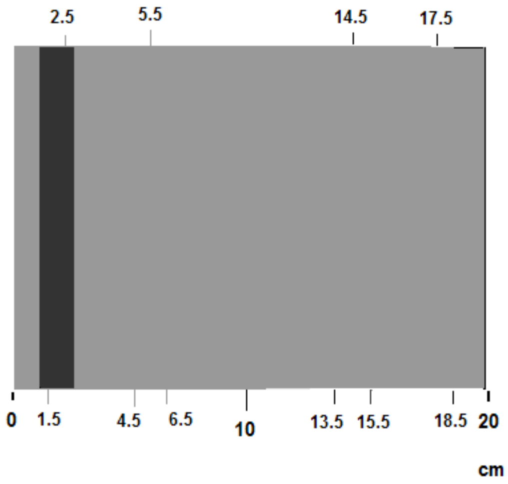

Figure 37: 2 cm thick air at 2cm depth

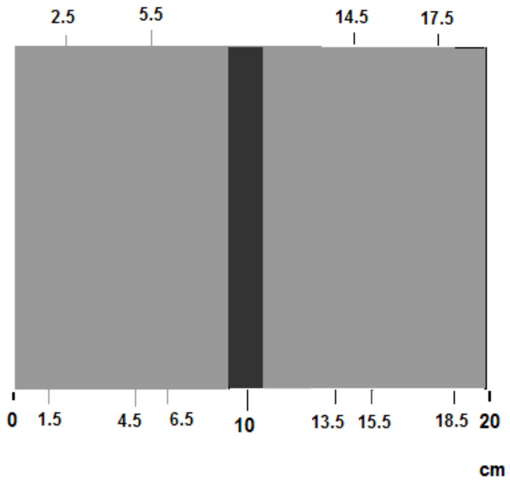

Figure 38: 2 cm thick air at 10cm depth

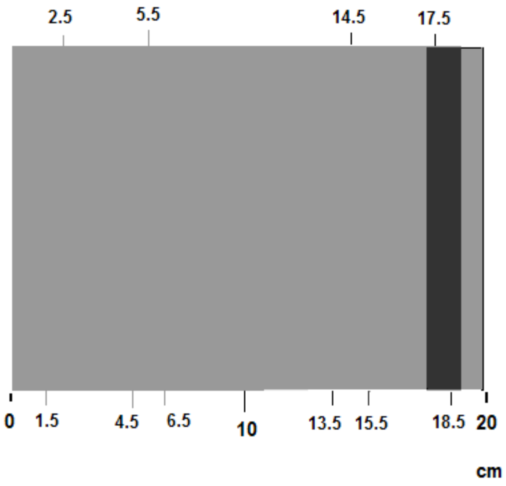

Figure 39: 2 cm thick air at 18cm depth

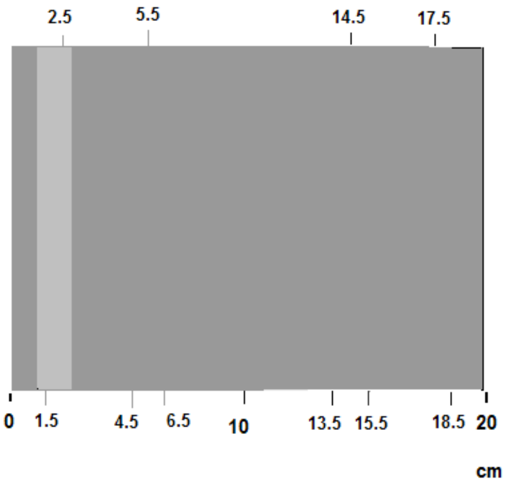

Figure 40: 2 cm thick bone at 2cm depth

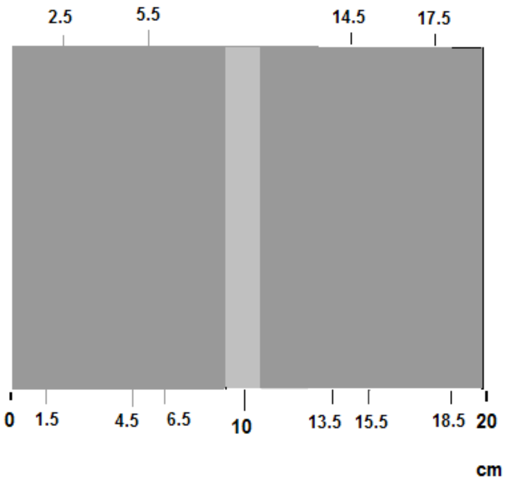

Figure 41: 2 cm thick bone at 10cm depth

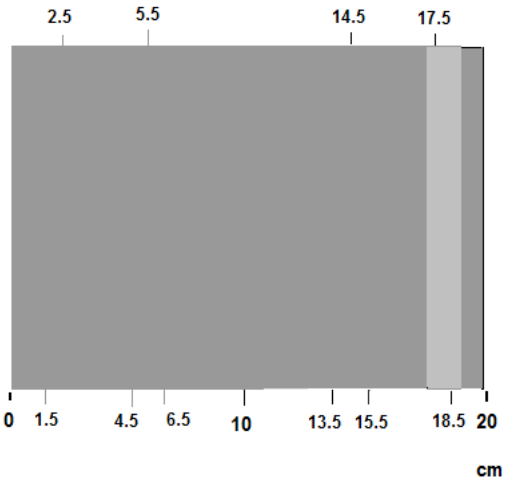

Figure 42: 2 cm thick bone at 18cm depth

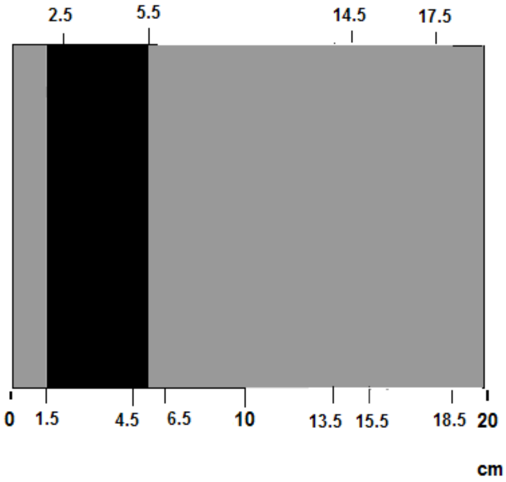

Figure 43: 4 cm thick air at 3.5cm depth

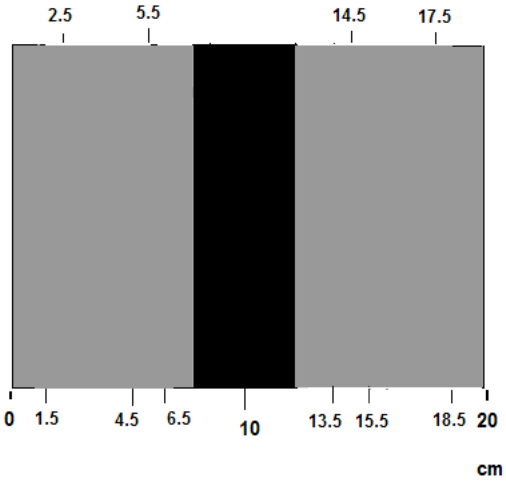

Figure 44: 4 cm thick air at 10cm depth

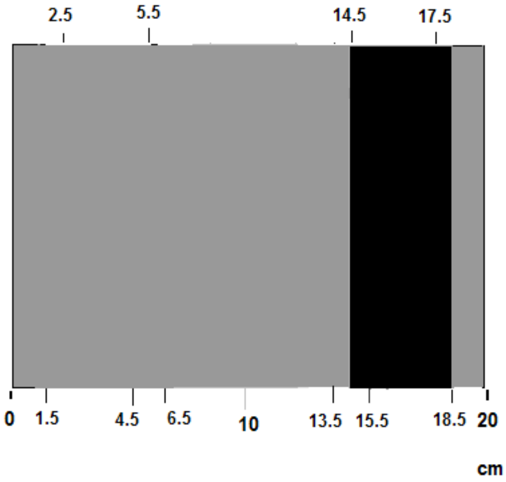

Figure 45: 4 cm thick air at 16.5 cm depth

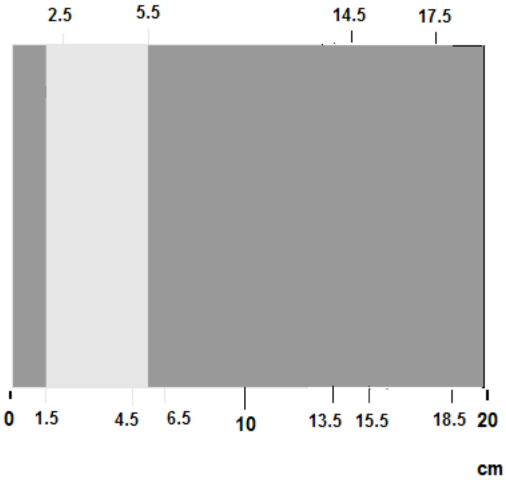

Figure 46: 4 cm thick bone at 3.5cm depth

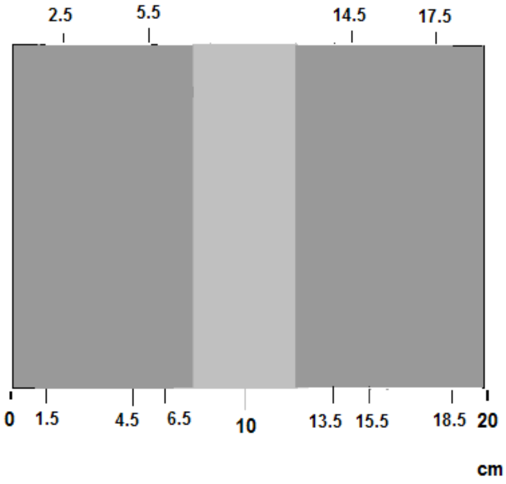

Figure 47: 4 cm thick bone at 10cm depth

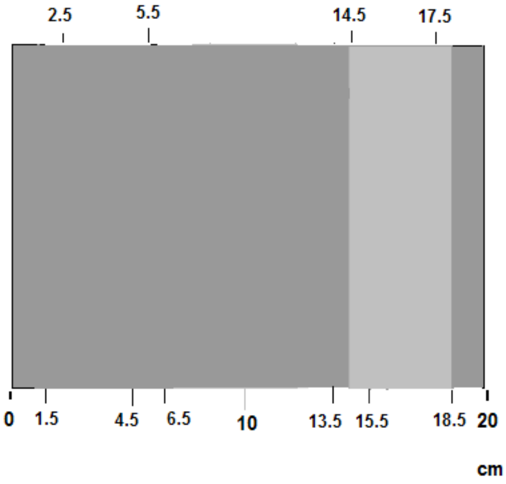

Figure 48: 4 cm thick bone at 16.5 cm depth

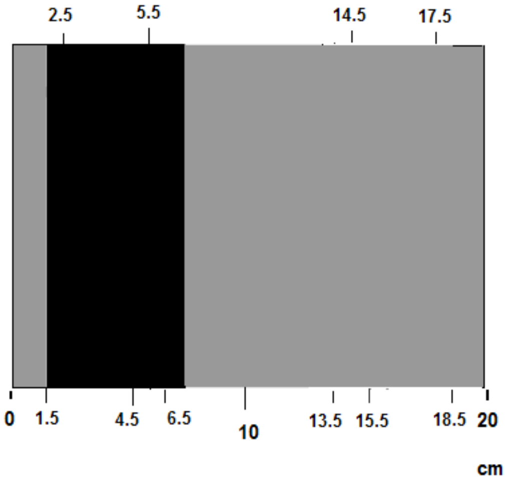

Figure 49: 6 cm thick air at 4.5cm depth

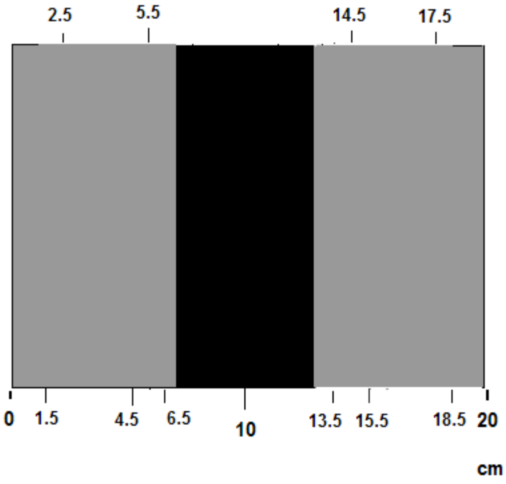

Figure 50: 6 cm thick air at 10cm depth

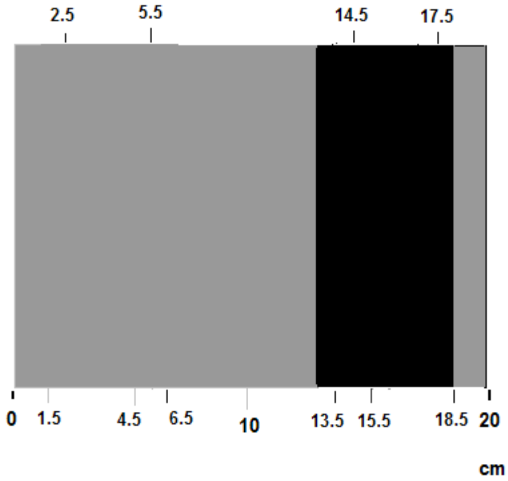

Figure 51: 6 cm thick air at 15.5cm depth

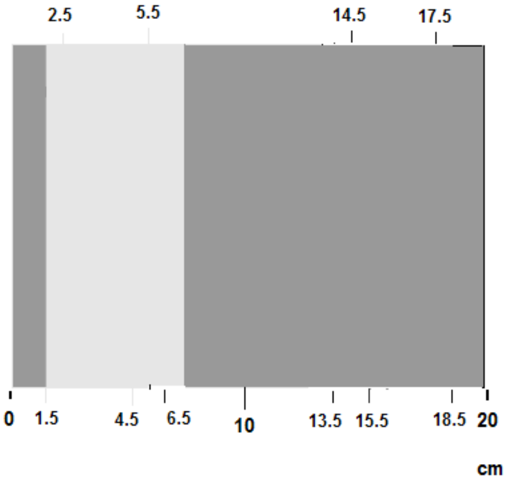

Figure 52: 6 cm thick bone at 4.5cm depth

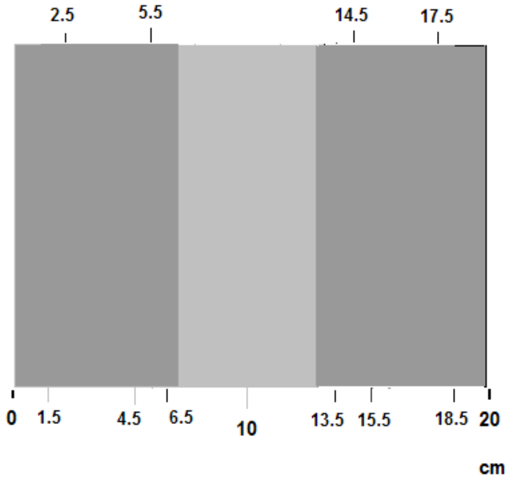

Figure 53: 6 cm thick bone at 10cm depth

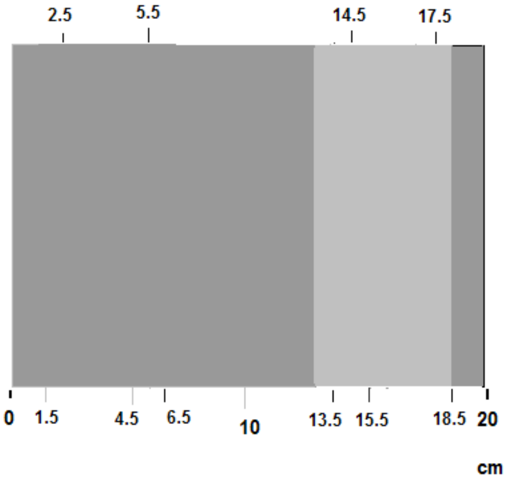

Figure 54: 6 cm thick bone at 15.5cm depth

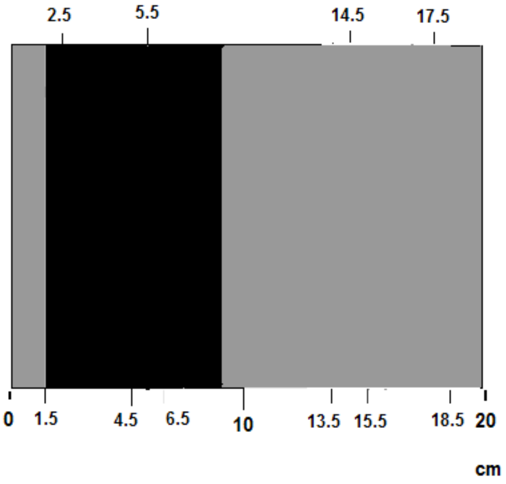

Figure 55: 8 cm thick air at 5.5cm depth

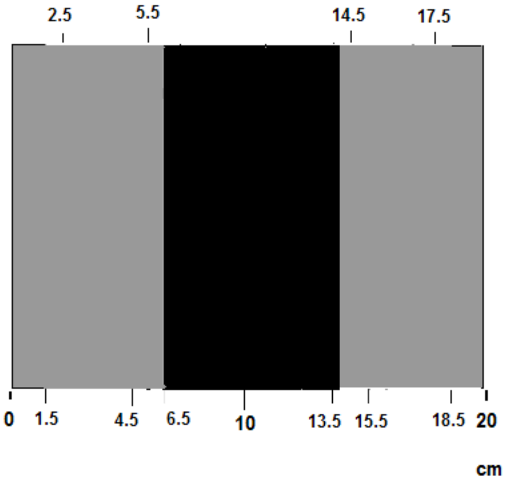

Figure 56: 8 cm thick air at 10cm depth

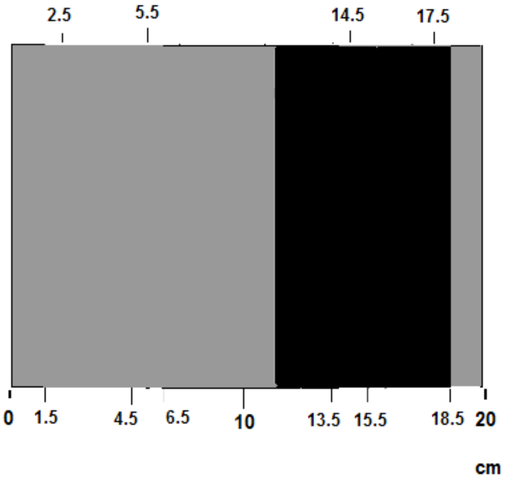

Figure 57: 8 cm thick air at 14.5cm depth

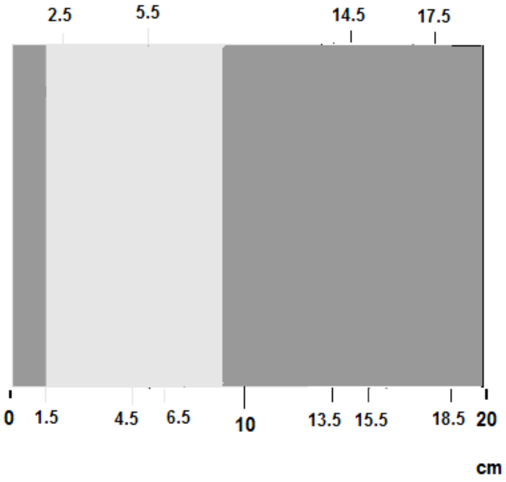

Figure 58: 8 cm thick bone at 5.5cm depth

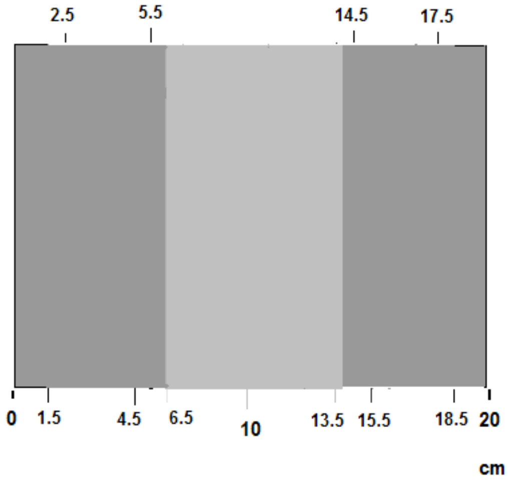

Figure 59: 8 cm thick bone at 10cm depth

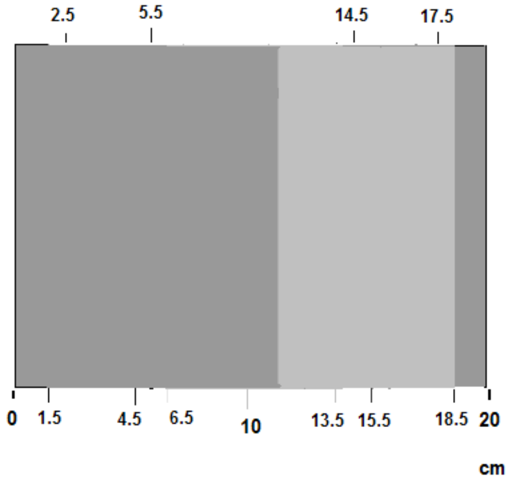

Figure 60: 8 cm thick bone at 14.5cm depth

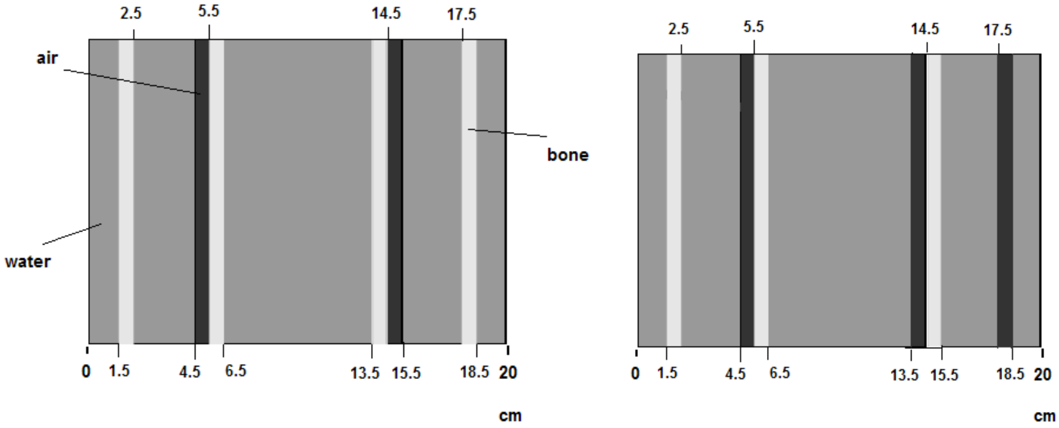

Figure 61: Profile of (left) _b_ab_ba_b_ phantom and (right) _b_ab_ab_a_ phantom. Each air or bone slice is 1 cm thick. The _b_ab_ba_b_ (b=bone; a=air, _=water) phantom has spatial and space-density symmetry. The _b_ab_ab_a_ phantom retains its spatial symmetry but loses its space-density symmetry because each slice has an opposite slice lying on the other side of the phantom's vertical mid-plane, which bisects the phantom into left and right halves (breaking space density symmetry). (left) The following "position" depths of the air slices (black) are 5 cm and 15 cm and of bone slices (lighter gray) are 2, 6, 14, and 18 cm. (right) Those of air slices are 5, 14, and 18 cm and of bone slices are 2, 6, and 15 cm.

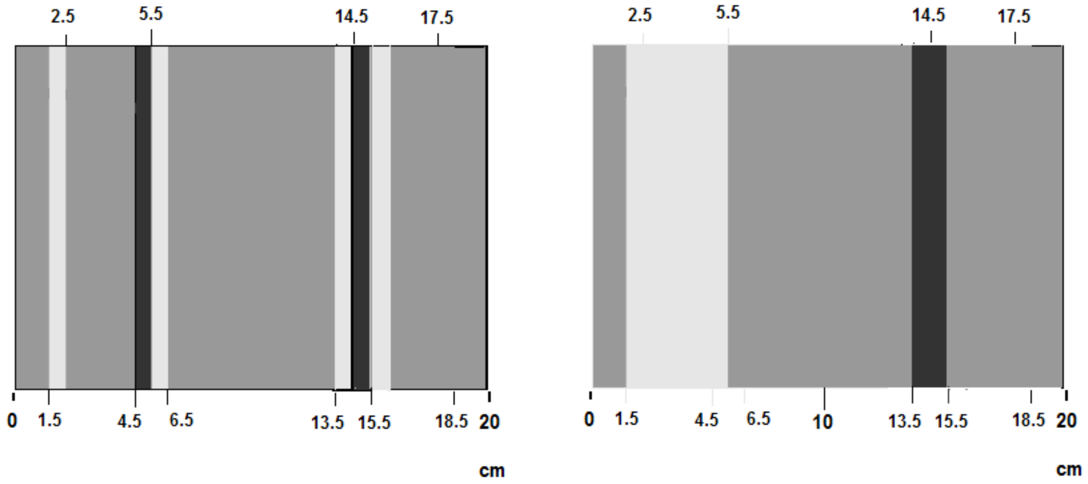

Figure 62: Profile of (left) _b_ab_bab_ phantom and (right) _bbbb_aa_ phantom. Each air or bone slice is 1 cm thick. The _b_ab_bab_ phantom loses its spatial symmetry because the right-most air slice is located at 15 cm depth, disrupting the left and right symmetry, but there are still two bone slices and one air slice in both the left and right halves, thus preserving space-density symmetry (breaking spatial symmetry). The _bbbb_aa_ phantom has left and right halves that are not alike in any way (breaking space density and spatial symmetry). (left) The following “position” depths of the air slices (black) are 5 cm and 15 cm and of bone slices (lighter gray) are 2, 6, 14, and 16 cm. (right) The center of the 2 cm thick air slice (black) is positioned at 14.5 cm depth and center of 4 cm thick bone slice (lighter gray) is at 3.5 cm depth.

All of the phantoms have displayed a near Gaussian distribution in their lateral displacements and angular directions. They share the common characteristic of the near Gaussian distribution profile for those two parameters and the exit energy. If we compare phantoms of the same material of different thicknesses, we can obtain the following for the 1 cm thick air and 8 cm thick air phantoms in Figure 63:

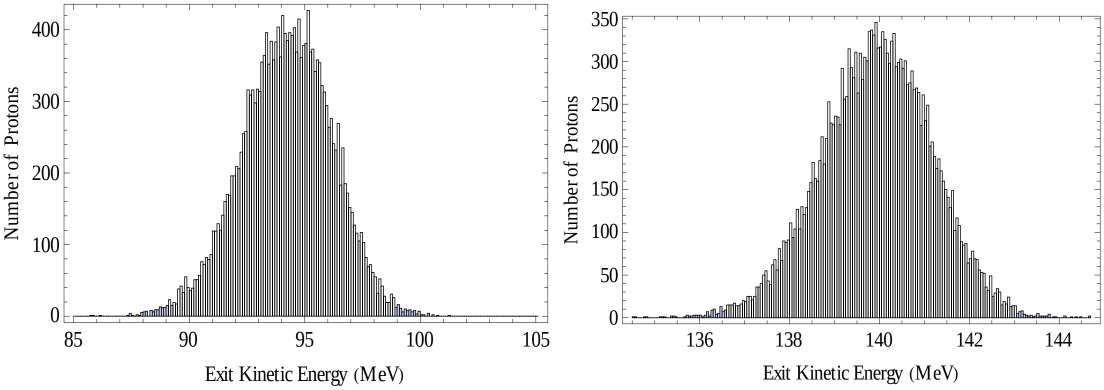

Figure 63: Histograms of proton exit energy distribution of (left) 1 cm thick air and (right) 8 cm thick air. The thicker 8 cm air has the higher mean exit energy of approximately 140 MeV, whereas the 1 cm has about 94 MeV. The thicker air has less obstruction to the protons' path; thereby, protons lose less kinetic energy in its phantom.

As the thickness of the air increases, the mean exit energy increases as well. The opposite is true for the bone because an increase in bone thickness results in greater inelastic collisions of the protons and the atomic electrons, thus a decrease in the mean exit energy. In Figure 64, the mean output energy for the 1 cm thick bone is about 80 MeV, whereas for the 8 cm thick bone it is close to 10 MeV. There is more energy loss due to straggling in the thicker bone, shown as the extending tail end.

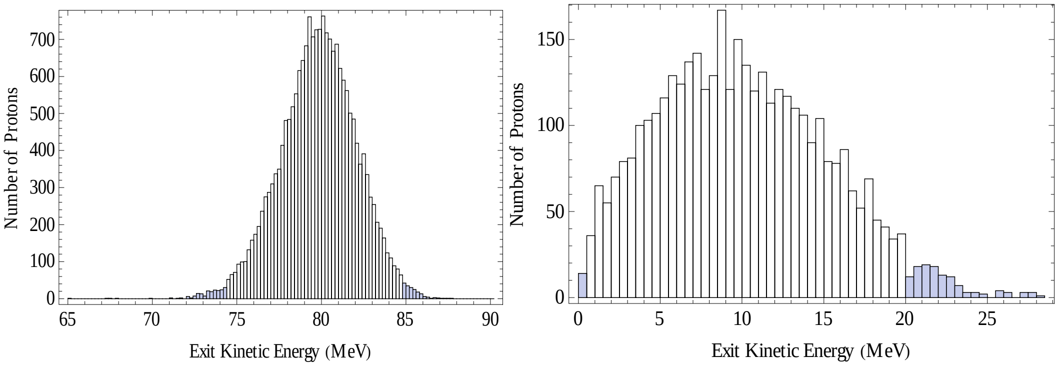

Figure 64: Histograms of proton exit energy distribution of (left) 1 cm thick bone and (right) 8 cm thick bone, which has a lower mean exit kinetic energy and a slightly higher end tail due to energy loss due to straggling.

In Figures 65-68, the lateral displacement and angular distributions have higher, narrower peaks for thicker air and thinner bone. Also their end tails are less noticeable because there are fewer scatterings. As mentioned in Chapter 1, the dose-lateral displacement distribution shows a shortened dose peak and broader lateral spread with increasing frequency of MCS as the proton beam travels deeper into the phantom. The number of protons represents the dose in Figure 13.

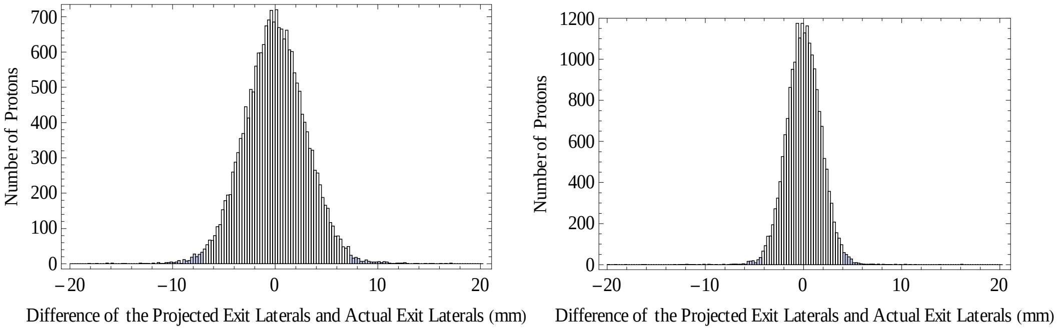

Figure 65: Histograms of proton lateral displacement distribution of (left) 1 cm thick air and (right) 8 cm thick air. The 8 cm thick air slice has a most number of protons (greatest dose) near the beam axis with the least lateral spread within the range of -10 mm and 10mm because the thicker air slab is the least dense with less material to scatter the protons.

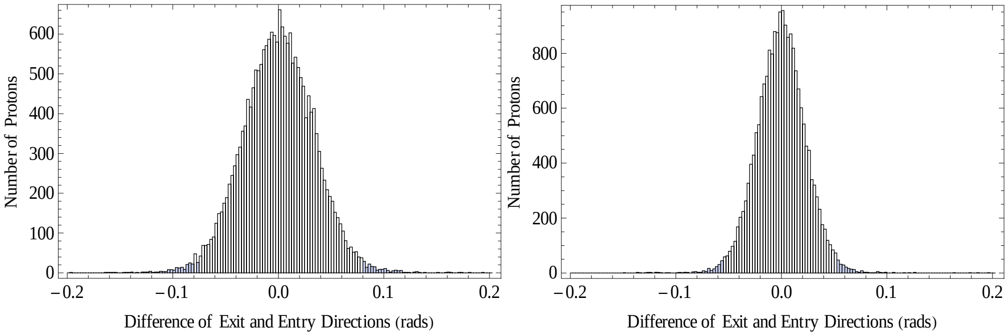

Figure 66: Histograms of proton angular distribution of (left) 1 cm thick air and (right) 8 cm thick air. Similar to the lateral displacement distribution, the thicker 8 cm air slice has the highest peak and the lowest angular spread because of fewer proton scatterings within the slice.

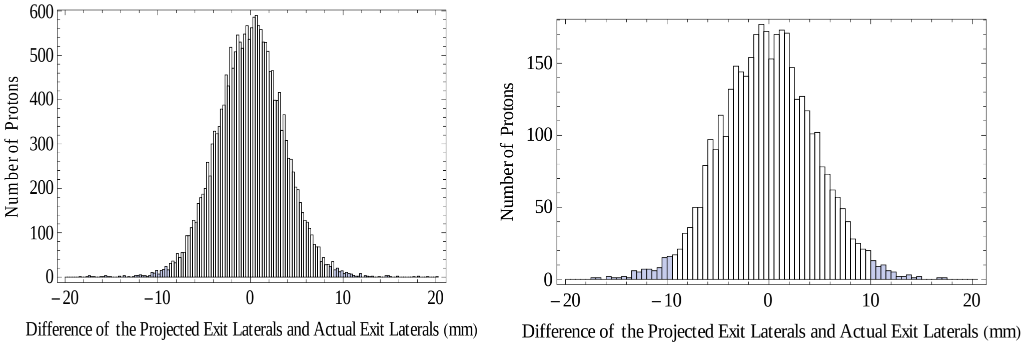

Figure 67: Histograms of proton lateral displacement distribution of (left) 1 cm thick bone and (right) 8 cm thick bone. The thicker 8 cm bone is denser than the 1 cm, thus scattering more protons and producing more lateral displacement spread.

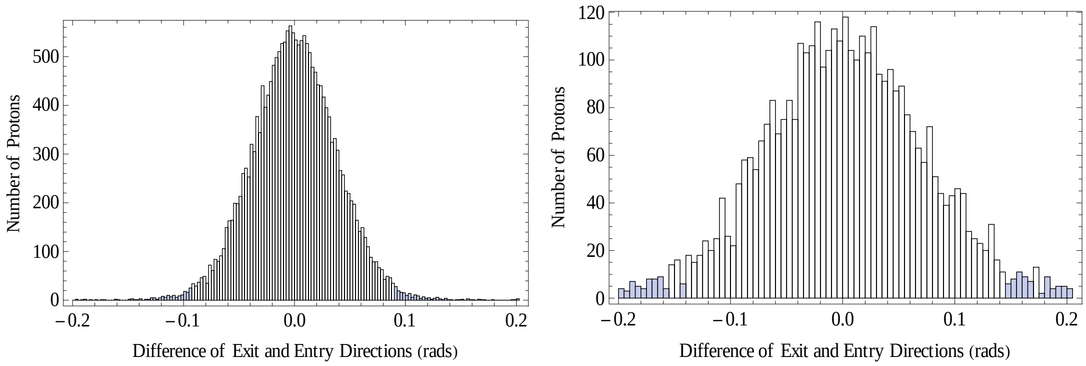

Figure 68: Histograms of proton angular distribution of (left) 1 cm thick bone and (right) 8 cm thick bone. Similar to the lateral displacement distribution, the thicker 8 cm bone slice has the lower peak and the greater angular spread because of several proton scatterings with greater angular deflections within the slice.

If a slice of a certain thickness is placed at any depth, the three distributions are more or less similar with no significant changes. The positioning of a slice with a specific thickness at any depth within a phantom does not significantly alter the profile of the lateral displacement, angular, and exit energy distributions.

The sample means of the MLP errors statistically fluctuate about zero, with no points lying outside the 95% confidence limit. When more protons are randomly sampled, the fluctuations become minimal, making the sample mean a reliable parameter that reflects the population mean of a normal distribution.

The RMS of the MLP errors for each phantom indicates the spatial resolution within 1 standard deviation envelope. The standard deviations of the MLP formalism that include and exclude the logarithmic term are compared to each other in each phantom when the energy loss condition is the same. Theoretically, the RMS traced out by the MLP with the log term (i.e., “Full” and “No loss”) is slightly less than the RMS by the MLP without the log term (i.e., “No log” and “No log + No loss”) if energy loss is either included or excluded, as shown in Figure 69. In the upper pair of curves, the top green “No log” plot is the RMS that excludes the log term but includes the energy loss, and the bottom blue “Full” plot includes both the log term and energy loss. If we exclude the energy loss as indicated in the lower pair, the top red “No log + No loss” plot excludes the log term while the bottom pink “No loss” plot includes it. Also energy loss increases the RMS since we see that the upper pair plots have a greater RMS by at least 0.19 mm. The MLP with the log term and no energy loss would decrease our RMS the most, thus improving the spatial resolution. (Note: Improving the spatial resolution means decreasing the RMS of the spatial resolution. It implies that there are fewer chances of error in delineating the tissue in question. A clearer image is obtained.)

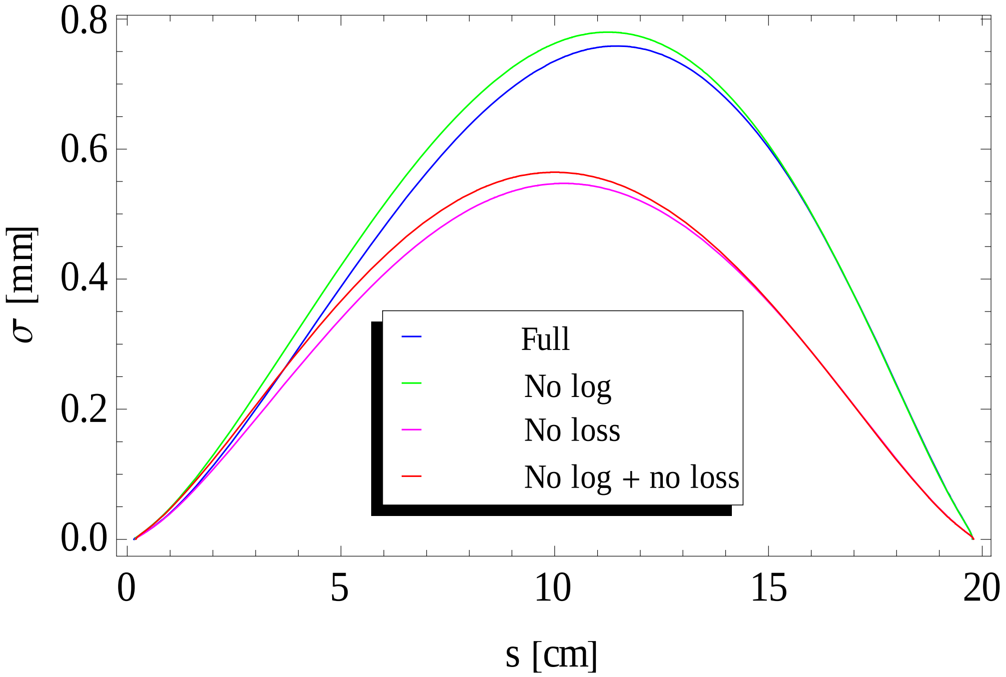

Figure 69: Four 1 standard deviation MLP error envelopes. σ is the standard deviation or the root mean square (RMS) in millimeters. Depth s is in centimeters. Full is the MLP formalism which includes the log term and energy loss. “No log” has energy loss, and “No loss” has log term. Approximations having the least to the greatest RMS: No loss, No log + no loss, Full, No log. [34]

In reality, when the physical interactions of the proton simulation are included, the MLP with the log may not have a lower RMS than the MLP without the log. Sometimes the difference of RMS between the two MLPs can be small, on the order of 0.0001 mm, and quite negligible. This is attributed to the MCS as the major source of statistical fluctuation. For example, in Figure 70 of the homogeneous water phantom, the maximum RMS of the MLP formalism without the log term is 0.6041 mm and the maximum RMS with the log term is 0.6037 mm; their RMS difference is approximately 0.0004 mm. The mean MLP error along every point of the depth is very close to zero. The respective minimum and maximum 95% confidence limits represented as dashed lines surrounding the mean are -0.007692 mm at 109.034 mm depth and 0.01544 mm at 129.95 mm depth for the plot without the log term and -0.006008 mm at 104.95 mm depth and 0.01776 mm at 134.135 mm depth for the plot with the log term.

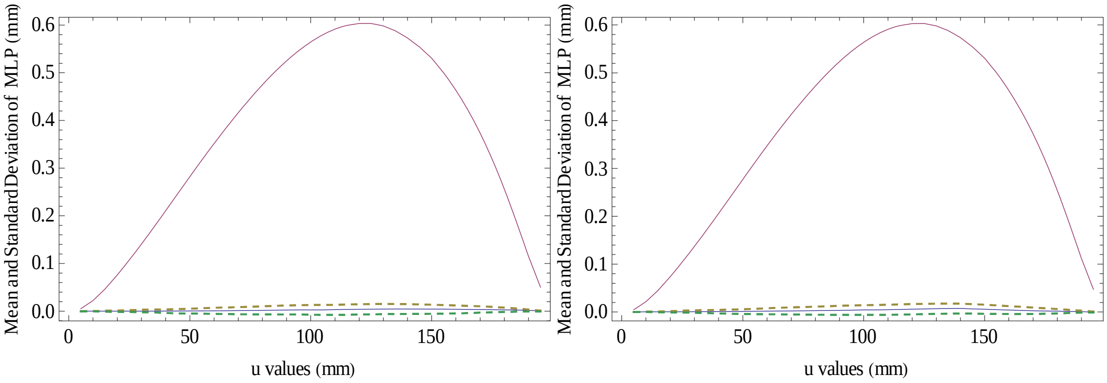

Figure 70: Plots of the mean and standard deviation (RMS) of the MLP errors for homogeneous water phantom supporting the theory. The larger solid curve in each plot is the RMS and the lower solid curve is the mean MLP error for each depth. The top and bottom dashed lines surrounding the mean are the 95% confidence limits. (Left) The maximum RMS without log is 0.6041 mm. (Right) Maximum RMS with log is 0.6037 mm.

But in Figure 71, the maximum RMS without the log term is 0.5257 mm, whereas the maximum RMS with the log term is 0.5373 mm; their RMS difference is about 0.0116 mm. This figure contradicts the theory that the RMS with the log term is less than the RMS without the log term. The MCS causes this contradiction. The respective minimum and maximum of the 95% confidence limits are -0.01151 mm at 118.897 mm depth and 0.007420 mm at 128.46 mm depth for the plot without the log term and -0.005796 mm at 163.04 mm depth and 0.01572 mm at 125.926 mm depth for the plot with the log term. The means of MLP errors for both plots are close to zero.

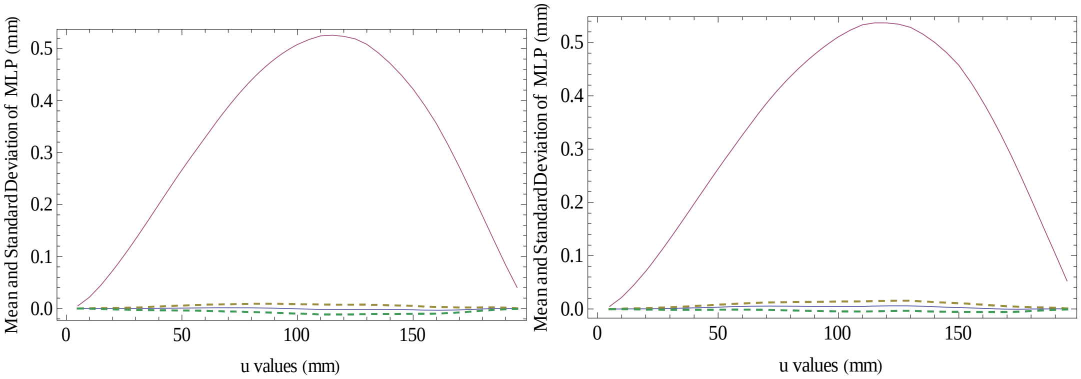

Figure 71: Plots of the mean and standard deviation (RMS) of the MLP errors for homogeneous water phantom contradicting the theory. (Left) The maximum RMS without the log term is 0.5257 mm. (Right) Maximum RMS with the log term is 0.5373 mm.

Next we compare the maximum RMS of each phantom's MLP with and without the log term and plot them in Figures 72 and 73. Each of the three points on a curve is a maximum RMS when its corresponding material slice's center is situated at a certain depth. The three points are the maximum RMS values for the slices located in the front, middle, and end of a phantom, but not simultaneous during simulation. For instance, the uppermost brown curve in both figures represents a movable 8 cm thick bone slice that was asynchronously positioned at 5.5, 10, and 14.5 cm depths during separate simulation. A maximum RMS value was obtained and compared for each of these positions.

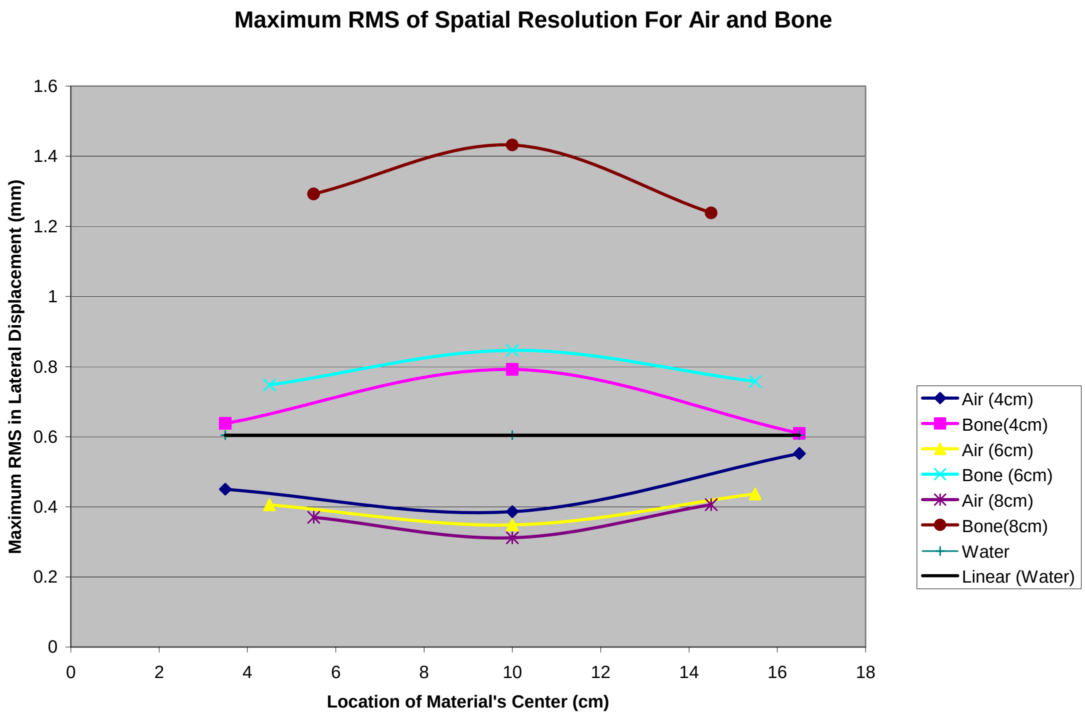

Figure 72: Comparing maximum RMS of MLP errors excluding the log term for phantoms with same slice positions.

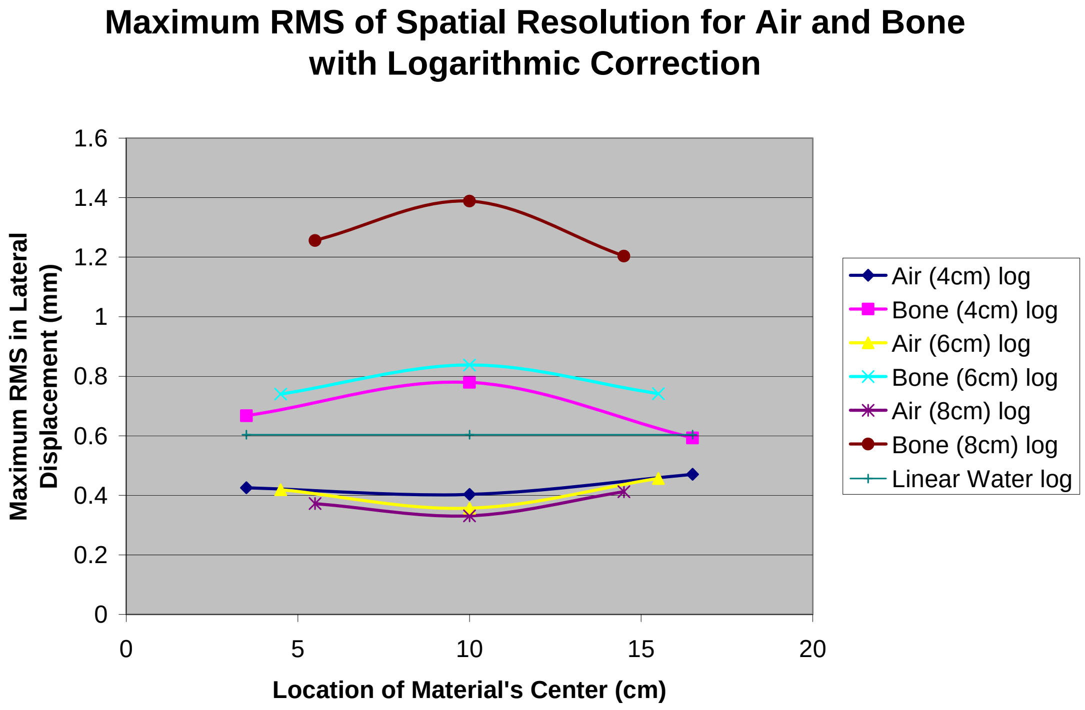

Figure 73: Comparing maximum RMS of MLP errors including the log term for phantoms with same slice positions.

In both cases, the material with the highest density and greatest thickness, such as bone, has the highest maximum RMS. Air with the lowest density and greatest thickness has the lowest maximum RMS. Water is the reference, whose RMS lies in between bone and air. The endpoints of each curve having the least deviation are determined by the physical constraints. Also the RMS with the log term for air is slightly higher than that without the log term. Table 2 shows the values of the maximum RMS based on Figures 72 and 73, starting with 4 cm air and bone slice to 8 cm. Water is the reference. Generally, the maximum RMS without the log term is greater than that with the log term for bone. However, the maximum RMS without the log term is less for air.

Table 2

Comparing the RMS Without and With the Log Term for Phantoms with the Same Material Type in the Same Position

Location of Center (cm)	RMS of Spatial Resolution (mm)		
	without log	with log	relative error
Air (4cm)			
3.5	0.450341	0.425423	0.055331
10	0.386048	0.403279	-0.04463
16.5	0.552318	0.470749	0.147685
Bone (4cm)			
3.5	0.637501	0.667488	-0.04704
10	0.79215	0.779397	0.016099
16.5	0.609508	0.592515	0.02788
Air (6cm)			
4.5	0.405921	0.418919	-0.03202
10	0.348313	0.356251	-0.02279
15.5	0.437023	0.45687	-0.04541
Bone (6cm)			
4.5	0.74753	0.740019	0.010048
10	0.846244	0.837918	0.009839
15.5	0.757628	0.741217	0.021661
Air (8cm)			
5.5	0.370114	0.372015	-0.00514
10	0.311598	0.330988	-0.06223
14.5	0.406446	0.41247	-0.01482
Bone(8cm)			
5.5	1.29237	1.25577	0.02832
10	1.43214	1.38831	0.030605
14.5	1.23833	1.20322	0.028353
Water			
3.5	0.604135	0.603737	0.000659
10	0.604135	0.603737	0.000659
16.5	0.604135	0.603737	0.000659

For more complex phantoms, we arranged the air and bone slices where we preserve the space-density/spatial symmetry (_b_ab_ba_b_ phantom), and then break the space-density symmetry (_b_ab_ab_a_), the spatial symmetry (_b_ab_bab_), and then both (_bbbb_aa_) in order see their distributions and RMS. All the phantoms except for _b_ab_ab_a_ have more or less the same mean energy loss with similar energy spread. But all their lateral displacement and angular distributions show no significant differences. Overall, disrupting the symmetry does not affect the distributions; thus the distributions are position independent. Also according to the integral, the relative electron density does not specify the location at which the MLP touches it as long as the density voxel is located somewhere on the MLP. Table 3 shows that the maximum RMS without the log term is consistently more than that without the log for complex phantoms.

Table 3

Comparing the RMS Without and With the Log Term for Complex Phantoms

	RMS of Spatial Resolution (mm)		Relative Error
	without log	with log	
b_ab_ba_b	0.618592	0.608108	0.016948
b_ab_bab	0.595944	0.567161	0.048298
b_ab_ab_a	0.530329	0.525371	0.009349
bbbb_aa	0.593643	0.574815	0.031716

Chapter 4

SUMMARY AND CONCLUSION

The importance of pCT is its ability to remove the uncertainty of the Bragg peak location perpetrated by the conversion function from HU to proton stopping power in xCT-based proton therapy treatment planning. pCT has the potential to directly utilize the proton stopping power inherent in proton therapy and convert it to relative electron density, as shown in equation (32). Determining this density becomes essential in improving the density image resolution of a tissue; however, the energy loss variation attributed to straggling physically limits the resolution. Another important aspect of pCT is the spatial resolution which is physically limited by multiple Coulomb scattering. As mentioned before, improving the spatial resolution means decreasing the RMS of the spatial resolution. It implies that there are fewer chances of error in delineating the tissue in question. A clearer and finer image is thus obtained. To quantitatively evaluate the spatial resolution, the proton's most likely path (maximum likelihood path) formalism is formulated.

This thesis has focused on the evaluation of the protons' analytical MLP, which was originally assumed for homogeneous water phantom, under inhomogeneous phantom conditions. Of comparable material thickness, the results show that phantoms with lower density material such as air have much lower RMS than the reference water and higher density material such as bone. Of the same air material, an increased thickness of an air slab has a much lower RMS than its thinner counterpart. But for the same bone material, an increased thickness of bone slab has a much higher RMS than its thinner counterpart. This concludes that the RMS is greatly affected by the density and since MCS is a large factor in the increased RMS of the spatial resolution, higher density materials have larger atomic number that causes these Coulomb scatterings of the primary protons.

We then tested the effect of the logarithmic term inclusion into the MLP formalism. By setting our RMS of water as the reference, we see that phantoms with lower density material compared to water generally have lower RMS without the log term than the one with the log term. However, phantoms with higher density have a higher RMS without the log term than the one with the log term. On our RMS plot, we see a negative concavity for the bone and a positive one for the air. The greatest deviation for each curve is usually situated about the middle of the phantom because the endpoints of each curve are physically constrained towards the interface between the watery environment and vacuum. The presence of the detectors physically constrains those endpoints. The negative concavity displayed by phantoms with higher density with or without the log term proves how the MCS and energy loss greatly worsens our spatial resolution (as high as 1.5 mm) for pCT. Although MCS is our major physical limiting factor for spatial resolution, the energy loss has an effect on the spatial resolution as well.

The logarithmic term which was derived empirically improved (that is decreased RMS) our spatial resolution for higher density phantoms. Although higher density can be a hindrance for improving spatial resolution, the log term has generally improved its spatial resolution by 3%. But in the case for lower density such as air, the log term can worsen the spatial resolution as high as 6%. Nevertheless, it is much more advantageous to have a lower density phantom. In reality though, lower density air tissues are not as abundant as higher density bone tissues. The reason there is a better agreement with Geant4 when keeping the log term for bone but not for air could be that the log term was originally derived in the case of water. The water density "factor," implicitly embedded in the derivation of the log term, may have improved the spatial resolution for bone and worsened it for air. Because air is much less dense than water, the log term assumed the air to have that water density "factor."

For our complex phantoms, which perhaps represent a human body more accurately than the phantoms with slices of a single material, we see that the logarithmic term has improved the spatial resolution as high as about 5%. The effect of bone has overridden the air's which allowed the log term to show an appreciable difference. The _b_ab_ab_a_ phantom shows the slightest improvement by 0.9%; this is due to an extra air slice and a deletion of a bone slice.

The water phantom shows almost a negligible percentage change of 0.066%. Seemingly, the logarithmic term does not significantly affect the spatial resolution for water.

Aside from the RMS, Chapter 3 shows histograms of the proton exit energy distribution where the bone slice with greater thickness exhibits lower mean exit energy with lower number of protons at its peak than the thinner bone slice. Also the tail ends of the greater thickness are more extensive due to energy loss straggling. For a thicker air slice, its mean exit energy is higher with less extension of the tail ends because of less straggling. This concludes that increased density increases the number of atomic electrons which cause energy loss straggling of the protons.

Likewise, the histograms of proton lateral displacement distribution demonstrate that increased density produces a greater lateral displacement spread but with a lower peak. The histograms of proton angular distribution also follow the same trend as those of the lateral displacement distribution. Primarily, greater lateral displacement and angular deflection are contributed by the increasing presence of nuclei as density increases.

Last, the analytical MLP must be customized to specific density settings in a phantom. More sophisticated MLP algorithms would need to be developed in order to assume not just water-equivalent phantoms but other various materials including the extreme cases for air and bone. These algorithms would need to take inhomogeneities of the phantoms into account.

In summary, for homogeneous water phantoms the best we can hope for is around ~0.5 mm spatial resolution. The results show that for realistic human tissues, where we do not expect large deviations on average from the density of water, the analytical MLP is good enough. However, for cases where there is an abundance of high-density material in the tissue, the analytical MLP may not be accurate enough. The boundary between acceptable and not acceptable is between 6 cm to 8 cm thick compact bone. Also, in general the log correction makes the MLP a better representation of the actual physics, but there are exceptions. Overall, the log term should be kept.

REFERENCES

1. Goitein, M. (2008). Radiation Oncology: A Physicist's-Eye View. New York, NY: Springer Science + Business Media,LLC.

2. Saha, G.B. (2006). Physics and Radiobiology of Nuclear Medicine (3rd Edition). New York, NY: Springer Science + Business Media, Inc.

3. Gurley, L.T. and Callaway, W.J. (1986). Introduction to Radiologic Technology (2nd Edition). St. Louis, MO: Multi-Media Publishing Inc.

4. Williams, J.R. and Thwaites, D.I. (1993). Radiotherapy Physics in Practice. Oxford: Oxford University Press.

5. Introduction: Particle Therapy. http://www.medical.siemens.com/webapp/wcs/stores/servlet/CategoryDisplay~q_catalogId~e_-11~a_categoryId~e_1011214~a_catTree~e_100010,1008643,1009404,1011214~a_langId~e_-11~a_storeId~e_10001.htm#pt

6. National Institute of Radiological Sciences. http://www.nirs.go.jp/ENG/research/charged_particle/index.shtml

7. Humphries, S., Jr. (1999). Principles of Charged Particle Acceleration. Albuquerque, NM: Field Precision.

8. Layout of a Typical Synchrotron. http://geographyfieldwork.com/SynchrotronWorks.htm

9. Ma, C.-M., Veltchev, I., Fourkal, E., Li, J.S., Luo, W., Fan, J., Lin, T. and Pollack, A. (2006). Development of a Laser-Driven Proton Accelerator for Cancer Therapy. *Laser Physics, 16* (4), pp.1-8.

10. Nelson, S.D., Poole, B.R. and Caporaso, G.J. (2007). Electromagnetic Simulations of Linear Proton Accelerator Structures Using Dielectric Wall Accelerators. *Proceedings of PAC07*. Albuquerque, NM.

11. Caporaso, George J., Sampayan, S., Chen, Y-J., Blackfield, D., Harris, J., Hawkins, S., Holmes, S., Krogh, M., Nelson, S., Nunnally, W., Paul, A., Poole, B., Rhodes, M., Sanders, D., Selenes, K., Sullivan, J., Wang, L. and Watson, J. (2007). High Gradient Induction Accelerator. *Proceedings of PAC07*. Albuquerque, NM.

12. Mori, Y. (2005). Developments of FFAG Accelerator. High Energy Accelerator Research Organization (KEK).

13. Ruggiero, A.G. (2009). Non-Scaling FFAG Cyclotrons. Hadron Beam Therapy of Cancer, Erice, Sicily, Italy.

14. Trbojevic, D. and Ruggiero, A.G. (2005). Design of a Non-Scaling FFAG Accelerator for Proton Therapy. Cyclotron Conference 2004, Tokyo.

15. Méot, F. (2004). Fixed Field Alternating Gradient Synchrotrons. CARE/HHH Workshop, CERN.

16. Seltzer, S.M. (1993). An Assessment of the Role of Charged Secondaries from Nonelastic Nuclear Interactions by Therapy Proton Beams in Water. National Institute of Standards and Technology Report NISTIR 5221.

17. Johns, H.E. and Cunningham, J.B. (1983). The Physics of Radiation (4th Edition) Springfield, IL: Charles C. Thomas.

18. 7.2.3 Linear Energy Transfer. http://www.med.harvard.edu/JPNM/physics/nmltd/radprin/sect7/7.2/7_2.3.html

19. CSDA Range. http://physics.nist.gov/PhysRefData/Star/Text/appendix.html

20. Cormack, A.M. (1979). Early Two-Dimensional Reconstruction and Recent Topics Stemming from It. *Nobel Lectures, Physiology or Medicine 1971-1980,* Singapore: World Scientific Publishing Co.

21. Markoe, A. (2006). Analytic Tomography. New York, NY: Cambridge University Press.

22. Schulte, R.W., Bashkirov, V., Klock, M.C. Loss, Li, T., Wroe, A.J., Evseev, I., Williams, D.C. and Satogata, T. (2005). Density Resolution of Proton Computed Tomography. *Medical Physics, 32*, pp. 1035-1046.

23. Khan, F.M. (2003). The Physics of Radiation Therapy (3rd Edition). Philadelphia, PA: Lippincott Williams & Wilkins.

24. Erdelyi, B., Wong, K., Schulte, R., Bashkirov, V., Coutrakon, G. and Sadrozinski, H. (2008). The Northern Illinois University, Loma Linda University Medical Center, and Santa Cruz Institute for Particle Physics Collaboration on Proton Computed Tomography. PTCOG 47, Jacksonville, FL.

25. Bruzzi, M., Blumenkrantz, N., Feldt, J., Heimann, J., Sadrozinski, H F.-W., Seiden, A., Williams, D.C., Bashkirov, V., Schulte, R., Menichelli, D., Scaringella, M., Cirrone, G.A. Pablo, Cuttone, G., Randazzo, N., Sipala, V. and Lo Presti, D. (2007). Prototype Tracking Studies for Proton CT. *IEEE Transactions On Nuclear Science, 54(1)*, pp. 1-6.

26. Schulte, R., Bashkirov, V., Li, T., Liang, J.Z., Mueller, K., Heimann, J., Johnson, L.R., Keeney, B., Sadrozinski, H F-W., Seiden, A., Williams, D.C., Zhang, L., Li, Z., Peggs, S., Satogata, T. and Woody, C. (2004). Design of a Proton Computed Tomography System for Applications in Proton Radiation Therapy. *IEEE Trans. Nucl. Sci., 51*, pp. 866-872.

27. Schneider, U., Pedroni, E. and Lomax, A. (1996). The Calibration of CT Hounsfield Units for Radiotherapy Treatment Planning. *Phys. Med. Biol., 41*, pp. 111-124.

28. Mustafa A. A. and Jackson D. F. (1983). The Relation Between x-Ray CT Numbers and Charged Particle Stopping Powers and Its Significance for Radiotherapy Treatment Planning. *Phys. Med. Biol., 28*, pp. 169-176.

29. Penfold, S.N., Schulte, R.W., Bashkirov, V. and Rosenfeld, A.B. (2008). Progress with the Proton Computed Tomography Development Project. MMD-IPCT Conference, Wollongong, Australia.

30. Cormack, A.M. (1963). Representation of a Function by Its Line Integrals, with Some Radiological Applications. *Journal of Applied Physics, 34(9)*, pp. 2723-2727.

31. Rossi, B. and Greisen, K. (1941). Cosmic-Ray Theory. *Reviews of Modern Physics, 13,* pp. 262-268.

32. Eyges, L. (1948). Multiple Scattering with Energy Loss. *Phys. Rev. 74,* pp. 1534-1535.

33. Lynch, G.R. and Dahl, O.I. (1991). Approximations to Multiple Coulomb Scattering. *Nuclear Instruments and Methods in Physics Research, B58,* pp. 6-10.

34. Gottschalk, B., Koehler, A.M., Schneider, R.J., Sisterson, J.M. and Wagner, M.S. (1992). Multiple Coulomb Scattering of 160 MeV Protons. *Nuclear Instruments and Methods in Physics Research, B74,* pp. 467-490.

35. Erdelyi, B. (2009). Generalization of the Most Likely Path Formalism for Proton Computed Tomography. *Physics in Medicine and Biology,* under review.

36. Composition of A-150 Tissue-Equivalent Plastic.
http://physics.nist.gov/cgi-bin/Star/compos.pl?matno=099

37. Penfold, S.N., Schulte, R.W., Censor, Y., Bashkirov, V., McAllister, S., Schubert, K.E. and Rosenfeld, A.B. (2008). Block-Iterative and String-Averaging Projection Algorithms in Proton Computed Tomography Image Reconstruction. *The Huangguoshu International Interdisciplinary Conference on Biomedical Mathematics – Promising Directions in Imaging, Therapy Planning and Inverse Problems*.

38. Schneider, U. and Pedroni, E. (1994). Multiple Coulomb Scattering and Spatial Resolution in Proton Radiography. *Medical Physics, 21,* pp. 1657-1663.

39. Williams, D.C. (2004). The Most Likely Path of an Energetic Charged Particle Through a Uniform Medium. *Phys. Med. Biol., 49,* pp. 2899-2911.

40. Schulte, R.W., Penfold, S.N., Tafas, J.T. and Schubert, K.E. (2008). A Maximum Likelihood Proton Path Formalism for Application in Proton Computed Tomography. *Medical Physics, 35*, pp. 4849-4856.

41. Wong, K., Erdelyi, B., Schulte, R., Bashkirov, V., Coutrakon, G., Sadrozinski, H., Penfold, S. and Rosenfeld, A. (2009) The Effect of Tissue Inhomogeneities on the Accuracy of Proton Path Reconstruction for Proton Computed Tomography. *AIP Conference Proceedings*, *1099*, pp. 476-480.

42. Cirrone, G.A., Cuttone, G., Candiano, G., Di Rosa, F., Lo Nigro, S., Lo Presti, D., Randazzo, N., Sipala, V., Bruzzi, M. Menichelli, D., Scaringella, M., Bashkirov, V., Williams, R.D., Sadrozinski, H.F.W., Heimann, J., Feldt, J., Blumenkrantz, N., Talamonti, C. and Schulte, R. (2007). Monte Carlo Studies of a Proton Computed Tomography System. *IEEE Transactions on Nuclear Sci.*, *54*(5), pp. 1487-1491.

43. G4BeamlineUsersGuide.pdf by Tom Roberts- FermiLab and Muons, Inc..
http://www.muonsinc.com/tiki-index.php?page=G4beamline

APPENDIX A

ALL HEADER FILE SOURCE CODES FOR THE _B_AB_BA_B_ PHANTOM

PhysicsList.hh

```
//
// PhysicsList
//
// This is just a copy (mostly) from novice example 2
//
#ifndef PhysicsList_hh
#define PhysicsList_hh
#include "G4VUserPhysicsList.hh"
#include "globals.hh"
class PhysicsList: public G4VUserPhysicsList
{
public:
PhysicsList();
protected:
// Construct particle and physics
virtual void ConstructParticle();
virtual void ConstructProcess();
//
virtual void SetCuts();
protected:
// these methods Construct particles
virtual void ConstructBosons();
virtual void ConstructLeptons();
protected:
// these methods Construct physics processes and register them
virtual void ConstructGeneral();
virtual void ConstructPhotonProcess();
virtual void ConstructElectronProcess();
virtual void ConstructPositronProcess();
virtual void ConstructHadEMProcess();
virtual void ConstructHadNuclearProcess();
virtual void ConstructIonInelasticProcess();
};
#endif
```

PrimaryGeneratorAction.hh

```
#ifndef PrimaryGeneratorAction_hh
#define PrimaryGeneratorAction_hh 1
//as this user defined class is derived from a geant4 base class, we need to include the
//class definition
#include "G4VUserPrimaryGeneratorAction.hh"
//this class is used to specify details of each particle, referred to as a 'generator'
class G4ParticleGun;
class G4Event;
//geant4 class which represents an event, ie. particle history
//the primary generator action class is used to specify how each primary particle is
//generated
class PrimaryGeneratorAction : public G4VUserPrimaryGeneratorAction {
public:
PrimaryGeneratorAction();
```

```
~PrimaryGeneratorAction();
//you must define this method, it is called by the G4RunManager
//run manager passes the pointer to an event object, it will be given attributes from the
//Particle Gun
void GeneratePrimaries(G4Event*);
private:
//private member of this class, a pointer to an object of another class
G4ParticleGun* gun;
};
#endif
```

AirDetector.hh

```
//
// AirDetector
//
#ifndef AirDetector_hh
#define AirDetector_hh
#include "G4VSensitiveDetector.hh"
class AirDetector : public G4VSensitiveDetector
{
public:
AirDetector();
void Initialize(G4HCofThisEvent* );
virtual void EndOfEvent( G4HCofThisEvent* );
protected:
//
// Called by geant4 for a particle traveling through
// the associated geometric object
//
G4bool ProcessHits( G4Step *step, G4TouchableHistory* );
G4double lateral_in[2];
G4double lateral_out[2];
G4double horizontal_in[2];
G4double horizontal_out[2];
G4double direction_in[2];
G4double direction_out[2];
G4double flag[2];
};
#endif
```

BoneDetector.hh

```
//
// BoneDetector
//
#ifndef BoneDetector_hh
#define BoneDetector_hh
#include "G4VSensitiveDetector.hh"
class BoneDetector : public G4VSensitiveDetector
```

```
{
public:
BoneDetector();
void Initialize(G4HCofThisEvent* );
virtual void EndOfEvent( G4HCofThisEvent* );
protected:
//
// Called by geant4 for a particle traveling through
// the associated geometric object
//
G4bool ProcessHits( G4Step *step, G4TouchableHistory* );
G4double lateral_in[4];
G4double lateral_out[4];
G4double horizontal_in[4];
G4double horizontal_out[4];
G4double direction_in[4];
G4double direction_out[4];
G4double flag[4];
};
#endif
```

WaterDetector.hh

```
//
// WaterDetector
//
#ifndef WaterDetector_hh
#define WaterDetector_hh
#include "G4VSensitiveDetector.hh"
class WaterDetector : public G4VSensitiveDetector
{
public:
WaterDetector();
void Initialize(G4HCofThisEvent* );
virtual void EndOfEvent( G4HCofThisEvent* );
protected:
//
// Called by geant4 for a particle traveling through
// the associated geometric object
//
G4bool ProcessHits( G4Step *step, G4TouchableHistory* );
G4double lateral[23];
G4double horizontal[23];
G4double direction[23];
G4double flag[23];
};
#endif
```

ExternalDetector.hh

```
//
// ExternalDetector
//
#ifndef ExternalDetector_hh
#define ExternalDetector_hh
#include "G4VSensitiveDetector.hh"
class ExternalDetector : public G4VSensitiveDetector
{
public:
ExternalDetector();
virtual void EndOfEvent( G4HCofThisEvent* );
virtual void Initialize( G4HCofThisEvent* );
protected:
//
// Called by geant4 for a particle traveling through
// the associated geometric object
//
G4bool ProcessHits( G4Step *step, G4TouchableHistory* );
G4double position[2], direction[2];
G4double energy;
G4int flag;
};
#endif
```

DetectorConstruction.hh

```
//preprocessor directives to prevent multiple includes of the same file
#ifndef DetectorConstruction_H
#define DetectorConstruction_H 1
//preprocessor directive to include the header file for the base class
#include "G4VUserDetectorConstruction.hh"
//class declaration, we don't need to tell the compiler how big it is, yet
class G4VPhysicalVolume;
//this is the user defined class that inherits behaviour from the virtual base class of the
//geant4 toolkit
class DetectorConstruction : public G4VUserDetectorConstruction{
public:
//declare the constructor for this class
DetectorConstruction();
//declare the destructor of this class
~DetectorConstruction();
//the one method that MUST be defined in this class, it is called "Construct", takes no
//arguments, and returns a pointer to an object of type G4VPhysicalVolume
G4VPhysicalVolume* Construct();
};
#endif
```

EventAction.hh

```
#ifndef EventAction_h
#define EventAction_h 1
#include "G4UserEventAction.hh"
#include "globals.hh"
class EventAction : public G4UserEventAction
{
public:
EventAction();
~EventAction();
public:
void BeginOfEventAction(const G4Event*);
void EndOfEventAction(const G4Event*);
void ExternalDetectorEvent(G4double [],G4double [],G4double);
void WaterDetectorEvent(G4double [],G4double [], G4double []);
void BoneDetectorEvent(G4double [],G4double [],G4double [],G4double [],G4double
[],G4double []);
void AirDetectorEvent(G4double [],G4double [],G4double [],G4double [],G4double
[],G4double []);
protected:
G4double Pos[2], Dir[2];
G4double lateral[33], horizontal[33];
G4double Eout;
G4double water_hor[23];
G4double air_hor_in[2];
G4double air_hor_out[2];
G4double bone_hor_in[4];
G4double bone_hor_out[4];
G4double water_lat[23];
G4double air_lat_in[2];
G4double air_lat_out[2];
G4double bone_lat_in[4];
G4double bone_lat_out[4];
G4double water_dir[23];
G4double air_dir_in[2];
G4double air_dir_out[2];
G4double bone_dir_in[4];
G4double bone_dir_out[4];
G4double direction[33];
int i;
};
#endif
```

APPENDIX B

SOME C++ SOURCE CODE FILES FOR THE _B_AB_BA_B_ PHANTOM

AirDetector.cc

```
//
// AirDetector
//
// Detector to measure the proton properties in the bone slices.
//
#include "AirDetector.hh"

#include "G4VTouchable.hh"
#include "G4Step.hh"
#include "G4StepPoint.hh"
#include "G4VPhysicalVolume.hh"

#include "EventAction.hh"
#include "G4EventManager.hh"

//
// Constructor
//
AirDetector::AirDetector()
   : G4VSensitiveDetector( "AirDetector" )
{;}

//
// Initialize
//
void AirDetector::Initialize(G4HCofThisEvent*)
{
   //
   // Initialize our flag array
   //
   for (int i=0;i<2;i++){
           flag[i]=0;
           lateral_in[i]=0;
           horizontal_in[i]=0;
           lateral_out[i]=0;
           horizontal_out[i]=0;
           direction_in[i]=0;
           direction_out[i]=0;
   }
}

//
// EndofEvent
//
void AirDetector::EndOfEvent( G4HCofThisEvent* )
{
   //
   // Pass information to EventAction
   //
   EventAction*        anEvent        =        (EventAction*)(G4EventManager::GetEventManager()-
>GetUserEventAction());
```

```
    anEvent-
>AirDetectorEvent(lateral_in,horizontal_in,lateral_out,horizontal_out,direction_in,direction_out);
}

//
// Process hits
//
G4bool AirDetector::ProcessHits( G4Step *step, G4TouchableHistory * )
{
    if (step->GetTrack()->GetTrackID() == 1){
        //
              // Fetch entrance point
              //
              const G4StepPoint *inPoint = step->GetPreStepPoint();

              //
              // Get the detector number
              //
              const G4VTouchable *touchable = inPoint->GetTouchable();
              G4int detector = touchable->GetCopyNumber();

              //
              // Check if 1st step in sensitive volume
              //
        if(flag[detector] == 0){
                  //
                  // Get position
                  //
                  lateral_in[detector] = inPoint->GetPosition().x() / mm;
                  horizontal_in[detector] = inPoint->GetPosition().z() / mm;

                  //
                  // Get direction, w.r.t z
                  //
                  direction_in[detector]          =          inPoint->GetMomentumDirection().x()/inPoint-
>GetMomentumDirection().z();

                  flag[detector]=1;
              }

              //
              // Fetch exit point
              //
              const G4StepPoint *outPoint = step->GetPostStepPoint();

              //
              // Get position
              //
              lateral_out[detector] = outPoint->GetPosition().x() / mm;
              horizontal_out[detector] = outPoint->GetPosition().z() / mm;

              //
              // Get direction, w.r.t z
              //
```

```
        direction_out[detector]     =     outPoint->GetMomentumDirection().x()/outPoint-
>GetMomentumDirection().z();
  }

  return true;
}
```

BoneDetector.cc

```
//
// BoneDetector
//
// Detector to measure the proton properties in the bone slices.
//
#include "BoneDetector.hh"

#include "G4VTouchable.hh"
#include "G4Step.hh"
#include "G4StepPoint.hh"
#include "G4VPhysicalVolume.hh"

#include "EventAction.hh"
#include "G4EventManager.hh"


//
// Constructor
//
BoneDetector::BoneDetector()
  : G4VSensitiveDetector( "BoneDetector" )
{;}

//
// Initialize
//
void BoneDetector::Initialize(G4HCofThisEvent*)
{
  //
  // Initialize our flag array
  //
  for (int i=0;i<4;i++){
        flag[i]=0;
        lateral_in[i]=0;
        horizontal_in[i]=0;
        lateral_out[i]=0;
        horizontal_out[i]=0;
        direction_in[i]=0;
        direction_out[i]=0;
  }
}

//
```

```
// EndofEvent
//
void BoneDetector::EndOfEvent( G4HCofThisEvent* )
{
  //
  // Pass information to EventAction
  //
  EventAction*     anEvent     =     (EventAction*)(G4EventManager::GetEventManager()-
>GetUserEventAction());
  anEvent-
>BoneDetectorEvent(lateral_in,horizontal_in,lateral_out,horizontal_out,direction_in,direction_out);
}

//
// Process hits
//
G4bool BoneDetector::ProcessHits( G4Step *step, G4TouchableHistory * )
{
  if (step->GetTrack()->GetTrackID() == 1){
    //
       // Fetch entrance point
       //
       const G4StepPoint *inPoint = step->GetPreStepPoint();

       //
       // Get the detector number
       //
       const G4VTouchable *touchable = inPoint->GetTouchable();
       G4int detector = touchable->GetCopyNumber();

       //
       // Check if 1st step in sensitive volume
       //
    if(flag[detector] == 0){
         //
         // Get position
         //
         lateral_in[detector] = inPoint->GetPosition().x() / mm;
         horizontal_in[detector] = inPoint->GetPosition().z() / mm;

         //
         // Get direction, w.r.t z
         //
         direction_in[detector]        =        inPoint->GetMomentumDirection().x()/inPoint-
>GetMomentumDirection().z();

         flag[detector]=1;
       }

       //
       // Fetch exit point
       //
       const G4StepPoint *outPoint = step->GetPostStepPoint();
```

```
        //
        // Get position
        //
        lateral_out[detector] = outPoint->GetPosition().x() / mm;
        horizontal_out[detector] = outPoint->GetPosition().z() / mm;

        //
        // Get direction, w.r.t z
        //
        direction_out[detector]        =        outPoint->GetMomentumDirection().x()/outPoint-
>GetMomentumDirection().z();

  }
  return true;
}
```

WaterDetector.cc

```
//
// WaterDetector
//
// Detector to measure the proton position and direction within a water cube.
//
#include "WaterDetector.hh"

#include "G4VTouchable.hh"
#include "G4Step.hh"
#include "G4StepPoint.hh"
#include "G4VPhysicalVolume.hh"

#include "G4VProcess.hh"
#include "G4String.hh"

#include "EventAction.hh"
#include "G4EventManager.hh"


//
// Constructor
//
WaterDetector::WaterDetector()
  : G4VSensitiveDetector( "WaterDetector" )
{;}

//
// Initialize
//
void WaterDetector::Initialize(G4HCofThisEvent*)
{
  //
  // Initialize our flag array
  //
```

```
   for (int i=0;i<23;i++){
            flag[i]=0;
            lateral[i]=0;
            horizontal[i]=0;
            direction[i]=0;
   }
}

//
// EndofEvent
//
void WaterDetector::EndOfEvent( G4HCofThisEvent* )
{
   //
   // Pass information to EventAction
   //
   EventAction* anEvent = (EventAction*)(G4EventManager::GetEventManager()-
>GetUserEventAction());
   anEvent->WaterDetectorEvent(lateral,horizontal,direction);
}

//
// Process hits
//
G4bool WaterDetector::ProcessHits( G4Step *step, G4TouchableHistory * )
{
   if (step->GetTrack()->GetTrackID() == 1){
      //
            // Fetch entrance point
            //
            const G4StepPoint *inPoint = step->GetPreStepPoint();

            //
            // Get the detector number
            //
            const G4VTouchable *touchable = inPoint->GetTouchable();
            G4int detector = touchable->GetCopyNumber();

            //
            // Check if 1st step in sensitive volume
            //
      if(flag[detector] == 0){
               //
               // Get position
               //
               lateral[detector] = inPoint->GetPosition().x() / mm;
               horizontal[detector] = inPoint->GetPosition().z() / mm;

               //
               // Get direction, w.r.t z
               //
               direction[detector] = inPoint->GetMomentumDirection().x()/inPoint-
>GetMomentumDirection().z();
```

```
            flag[detector]=1;
        }
    }
    return true;
}
```

DetectorConstruction.cc

```
//
// Detector Construction
//

#include "DetectorConstruction.hh"

#include "globals.hh"
#include "G4Element.hh"
#include "G4Material.hh"
#include "G4PVPlacement.hh"
#include "G4LogicalVolume.hh"
#include "G4Box.hh"
#include "G4Tubs.hh"
#include "G4SubtractionSolid.hh"
#include "G4IntersectionSolid.hh"
#include "G4VisAttributes.hh"

#include "G4SDManager.hh"
#include "WaterDetector.hh"
#include "ExternalDetector.hh"
#include "BoneDetector.hh"
#include "AirDetector.hh"

DetectorConstruction::DetectorConstruction()
{;}

DetectorConstruction::~DetectorConstruction()
{;}

G4VPhysicalVolume* DetectorConstruction::Construct()
{
    //
    // Define the elements that will be used in our materials
    //

    //
    // Define hydrogen
    //
    G4double A = 1.01 * g/mole;
    G4double Z = 1;
    G4Element* H = new G4Element ("Hydrogen", "H", Z, A);

    //
```

```
   // Define oxygen
   //
   A = 16.0 * g/mole;
   Z = 8;
   G4Element* O = new G4Element ("Oxygen", "O", Z, A);

   //
   // Define water
   //
   G4Material* water = new G4Material("water", 0.998 * g/cm3, 2);

   water->AddElement(H,2);
   water->AddElement(O,1);

   //
   // Define air (see novice example 6)
   //
   G4Element *N = new G4Element( "Nitrogen", "N",   7., 14.01*g/mole );

   G4Material *air = new G4Material( "Air", 1.29e-03*g/cm3, 2);
   air->AddElement(N, 0.7);
   air->AddElement(O, 0.3);

   //
   // Define bone
   //
   G4Element *Mg = new G4Element("T:Magnesium", "Mg", 12, 24.305*g/mole );
   G4Element *P  = new G4Element("T:Phosphorus","P",  15, 30.974*g/mole );
   G4Element *S  = new G4Element("T:Sulfur",    "S",  16, 32.06*g/mole  );
   G4Element *Ca = new G4Element("T:Calcium",   "Ca", 20, 40.08*g/mole  );
   G4Element *C = new G4Element( "Carbon", "C", 6, 12.011*g/mole );

   G4Material *bone = new G4Material( "T:Bone", 1.85*g/cm3, 8 );
   bone->AddElement( H,  0.063984 );
   bone->AddElement( C,  0.278    );
   bone->AddElement( N,  0.027    );
   bone->AddElement( O,  0.410016 );
   bone->AddElement( Mg, 0.002    );
   bone->AddElement( P,  0.07     );
   bone->AddElement( S,  0.002    );
   bone->AddElement( Ca, 0.147    );

   // Define vacuum
   G4Material *vacuum = new G4Material( "vacuum", 1.0, 1.01*g/mole, universe_mean_density,
kStateGas, 2.73*kelvin, 3.0E-18*pascal );

   //
   // Build the volumes
   //
   // Build the world volume (vacuum)
   //
   G4double worldx = 15 * cm;
   G4double worldy = 15 * cm;
   G4double worldz = 1 * m;
```

```
   G4Box* world = new G4Box("world_box", worldx, worldy, worldz);

   G4LogicalVolume* logical_world = new G4LogicalVolume(world, vacuum, "world_phys", 0,0,0);

   G4VPhysicalVolume* physical_world = new G4PVPlacement(0,G4ThreeVector(),logical_world,
"world_log", 0, false, 0);

   //
   // Build the water cube
   //
   G4double waterx = 10 * cm;
   G4double watery = 10 * cm;
   G4double waterz = 10 * cm;

   G4Box* water_box = new G4Box("water_box", waterx, watery, waterz);

   G4LogicalVolume* logical_water = new G4LogicalVolume(water_box, water, "water_log", 0,0,0);

   new G4PVPlacement(0, G4ThreeVector(0,0,50*cm), logical_water, "water_phys", logical_world,
false, 0);

   //
   // Make the box visible
   //
   G4VisAttributes *watervis = new G4VisAttributes( G4Color(1.0,0.0,1.0) ) ;
   watervis->SetForceSolid(true);
   logical_water->SetVisAttributes( watervis );

   //
   // Install the sensitive volumes in the water cube
   //
   G4Box *measure = new G4Box("measure", 10*cm, 10*cm, 0.05*mm);

   G4LogicalVolume *logical_measure = new G4LogicalVolume(measure, water, "measure_log",
0,0,0);

   G4int counter=0;

   for( int i=1;i<3;i++ ){
         new G4PVPlacement(0, G4ThreeVector(0,0,((i*0.5)-10)*cm), logical_measure,
"measure_phys", logical_water, false, counter);
         counter++;
   }

   for( int i=6;i<9;i++ ){
         new G4PVPlacement(0, G4ThreeVector(0,0,((i*0.5)-10)*cm), logical_measure,
"measure_phys", logical_water, false, counter);
         counter++;
   }

   for( int i=14;i<27;i++ ){
         new G4PVPlacement(0, G4ThreeVector(0,0,((i*0.5)-10)*cm), logical_measure,
"measure_phys", logical_water, false, counter);
```

```
          counter++;
   }

   for( int i=32;i<35;i++ ){
          new G4PVPlacement(0, G4ThreeVector(0,0,((i*0.5)-10)*cm), logical_measure,
"measure_phys", logical_water, false, counter);
          counter++;
   }

   for( int i=38;i<40;i++ ){
          new G4PVPlacement(0, G4ThreeVector(0,0,((i*0.5)-10)*cm), logical_measure,
"measure_phys", logical_water, false, counter);
          counter++;
   }

   //
   // Make the measurement volume sensitive
   //
   G4SDManager *sensitiveManager = G4SDManager::GetSDMpointer();

   G4VSensitiveDetector *measSens = new WaterDetector();
   sensitiveManager->AddNewDetector( measSens );
   logical_measure->SetSensitiveDetector( measSens );

   //
   // Install a vaccum sensitive volume before and after the cube
   // to determine true entry and exit conditions
   //
   const G4double vacuumZ[2] = { 39.9949*cm, 60.0051*cm };
   G4Box *endCheck = new G4Box("Check", 10*cm, 10*cm, 0.05*mm);

   G4LogicalVolume *logical_check = new G4LogicalVolume(endCheck, vacuum, "check_log", 0,0,0);

   for(int j=0;j<2;j++){
          new G4PVPlacement(0, G4ThreeVector(0,0,vacuumZ[j]), logical_check, "check_phys",
logical_world, false, j );
   }

   G4VSensitiveDetector *checkSens = new ExternalDetector();
   sensitiveManager->AddNewDetector( checkSens );
   logical_check->SetSensitiveDetector( checkSens );

   //
   // Install the bone structures
   //
   const G4double boneZ[4] = { -8*cm, -4*cm, 4*cm, 8*cm };
   G4Box *boneSlice = new G4Box("Bone", 10*cm, 10*cm, 0.5*cm);

   G4LogicalVolume *logical_bone = new G4LogicalVolume(boneSlice, bone, "bone_log", 0,0,0);

   for(int j=0;j<4;j++){
          new G4PVPlacement(0, G4ThreeVector(0,0,boneZ[j]), logical_bone, "bone_phys",
logical_water, false, j );
   }
```

```
   G4VSensitiveDetector *boneSens = new BoneDetector();
   sensitiveManager->AddNewDetector( boneSens );
   logical_bone->SetSensitiveDetector( boneSens );

   //
   // Install the air structures
   //
   const G4double airZ[4] = { -5*cm, 5*cm };
   G4Box *airSlice = new G4Box("Air", 10*cm, 10*cm, 0.5*cm);

   G4LogicalVolume *logical_air = new G4LogicalVolume(airSlice, air, "air_log", 0,0,0);

   for(int j=0;j<2;j++){
          new G4PVPlacement(0, G4ThreeVector(0,0,airZ[j]), logical_air, "air_phys", logical_water,
false, j );
   }

   G4VSensitiveDetector *airSens = new AirDetector();
   sensitiveManager->AddNewDetector( airSens );
   logical_air->SetSensitiveDetector( airSens );

   return physical_world;
}
```

APPENDIX C

AN EXAMPLE MATHEMATICA SOURCE CODE FOR COMPARING THE MLP WITH THE ACTUAL GEANT4 PROTON PATH IN HOMOGENEOUS WATER

```
Clear["Global`*"]
(* Input Data *)
dataEntryExit = ReadList[
   "c:\g4work\InhomogeneousMLP\OutputData\EntryAndExit_20thou_20cmcube@150_Fan_homogeneous
     _water_39.txt", Number, RecordLists → True];
dataInternal = ReadList[
   "c:\g4work\InhomogeneousMLP\OutputData\InternalPath_20thou_20cmcube@150_Fan_homogeneous
     _water_39.txt", Number, RecordLists → True];
Table[c[i], {i, 0, 5}] // Evaluate =
 {7.457*^-6, 4.548*^-7, -5.777*^-8, 1.301*^-8, -9.228*^-10, 2.687*^-11}
g[q_] := (k1 + k2 * Log[q]) (k1 + 2 * k2 + k2 * Log[q]) ;

(*Logarithmic correction*)
k1 = 1 - 0.038 Log[36.1];
k2 = 0.038;
(* x={xen,ten,xex,tex,z} *)
fac = 13.6 / Sqrt[36.1];
st[a_, b_] := fac Sqrt[NIntegrate[g[u] (b - u) ^2 Sum[c[i] u^i, {i, 0, 5}], {u, a, b}]]
stth[a_, b_] := fac Sqrt[NIntegrate[g[u] (b - u) Sum[c[i] u^i, {i, 0, 5}], {u, a, b}]]
sth[a_, b_] := fac Sqrt[NIntegrate[g[u] Sum[c[i] u^i, {i, 0, 5}], {u, a, b}]]

MLP[x_] := Module[{zend = 20, r0, r1, y0, y2, s1, s2, s1i, s2i, r1t, t1, t2 },
  r0 = {{1, x[[5]]}, {0, 1}}; r1 = {{1, zend - x[[5]]}, {0, 1}};
  s1 = {{st[0, x[[5]]]^2, stth[0, x[[5]]]^2}, {stth[0, x[[5]]]^2, sth[0, x[[5]]]^2}};
  s2 = {{st[x[[5]], zend]^2, stth[x[[5]], zend]^2},
    {stth[x[[5]], zend]^2, sth[x[[5]], zend]^2}}; y0 = {x[[1]], x[[2]]};
  y2 = {x[[3]], x[[4]]}; s1i = Inverse[s1]; s2i = Inverse[s2]; r1t = Transpose[r1];
  t1 = s1i + r1t.s2i.r1; t2 = s1i.r0.y0 + r1t.s2i.y2; Inverse[t1].t2]

err[z_] := Module[{ zend = 20, r1, s1, s2, s1i, s2i, r1t, t1}, r1 = {{1, zend - z}, {0, 1}};
  s1 = {{st[0, z]^2, stth[0, z]^2}, {stth[0, z]^2, sth[0, z]^2}};
  s2 = {{st[z, zend]^2, stth[z, zend]^2}, {stth[z, zend]^2, sth[z, zend]^2}};
  s1i = Inverse[s1]; s2i = Inverse[s2]; r1t = Transpose[r1]; t1 = s1i + r1t.s2i.r1; 2 Inverse[t1]]

(* pn = proton number *)
protons = Partition[dataInternal, 39];
DiffPlot[pn_] := Module[{zval, Xval, Diff}, zval = protons[[1, All, 1]];
  Xval = protons[[pn, All, 2]]; Diff = (Transpose[{zval, Xval}] / 10) -
     Table[{z, MLP[{dataEntryExit[[pn, 1]] / 10, dataEntryExit[[pn, 2]],
          dataEntryExit[[pn, 3]] / 10, dataEntryExit[[pn, 4]], z}][[1]]},
      {z, zval / 10}] // Chop ; Transpose[{zval / 10, 10 Diff[[All, 2]]}]]

Dev[pn_] :=
 Module[{maxdev, stdev, scr, av}, scr = DiffPlot[pn][[All, 2]]; maxdev = Sort[Abs[scr]][[-1]];
  av = Mean[scr]; stdev = StandardDeviation[scr]; {pn, av, stdev, maxdev}]

(*Fixed z values*)
(*scr Xval is in cm !!!*)
DevZ[z_, prsample_] :=
 Module[{maxdev, stdev, av, zval, Xval, scr, consz}, zval = protons[[1, All, 1]];
  consz = Table[Select[protons[[i]], #[[1]] == zval[[z]] &][[1]], {i, prsample}];
  Xval = consz[[All, 2]]; scr = (Xval / 10 - Table[
      MLP[{dataEntryExit[[pn, 1]] / 10, dataEntryExit[[pn, 2]], dataEntryExit[[pn, 3]] / 10,
         dataEntryExit[[pn, 4]], zval[[z]] / 10}][[1]], {pn, prsample}]) // Chop;
```

```
  maxdev = Sort[Abs[scr]][[-1]]; av = Mean[scr]; stdev = StandardDeviation[scr];
  {zval[[z]], av, stdev, maxdev}]
Length[protons]
(*1600 protons ~ 8 hrs  *)
prsample = RandomSample[Range[Length[protons]], 12 000]
results = Dev /@ prsample
Export["c:/results_homogeneous_water_39 with log 60% protons.txt", results, "Table"]
resultsfixedz = Table[DevZ[i, prsample], {i, 1, 39}]
Export["c:/resultsfixedz_homogeneous_water_39 with log 60% protons.txt",
 resultsfixedz, "Table"]
```

APPENDIX D

AN EXAMPLE MATHEMATICA CODE FOR THE HISTOGRAMS, MEAN MLP ERRORS AND RMS MLP ERRORS FOR HOMOGENEOUS WATER PHANTOM

```
Clear["Global`*"]

<< Histograms`

data = ReadList[
   "C:/results_homogeneous_water_39 with log 60% protons.txt", Number, RecordLists → True];

Histogram[data[[All, 2]], HistogramCategories → 100,
 HistogramRange → {-1.5, 1.5}, Frame → True,
 FrameLabel → {"Mean of Differences (mm)", "Number of Protons"}, LabelStyle → Medium]
Histogram[data[[All, 3]], HistogramCategories → 100, HistogramRange → {0, 0.8} ,
 Frame → True, FrameLabel → {"Standard Deviation of Differences (mm)", "Number of Protons"},
 LabelStyle → Medium]
Histogram[data[[All, 4]], HistogramCategories → 100, HistogramRange → {0, 2.5},
 Frame → True, FrameLabel → {"Maximum Deviation of Differences (mm)", "Number of Protons"},
 LabelStyle → Medium]

Mean[data[[All, 2]]]
StandardDeviation[data[[All, 2]]]

Mean[data[[All, 3]]]
StandardDeviation[data[[All, 3]]]

Mean[data[[All, 4]]]
StandardDeviation[data[[All, 4]]]

datafixedz = ReadList["C:/resultsfixedz_homogeneous_water_39 with log 60% protons.txt",
   Number, RecordLists → True];

Length[datafixedz]

ptMean = Transpose[{datafixedz[[All, 1]], 10 datafixedz[[All, 2]]}]
ListPlot[ptMean, Frame → True, Axes → False, Joined → True,
 FrameLabel → {"u values (mm)", "Mean of Differences (mm)"}, LabelStyle → Medium]

ptStDev = Transpose[{datafixedz[[All, 1]], 10 datafixedz[[All, 3]]}]
ListPlot[ptStDev, Frame → True, Axes → False, Joined → True, FrameLabel →
  {"u values (mm)", "Standard Deviation of Differences (mm)"}, LabelStyle → Medium]


ptMaxDev = Transpose[{datafixedz[[All, 1]], 10 datafixedz[[All, 4]]}]
ListPlot[ptMaxDev, Frame → True, Axes → False, Joined → True, FrameLabel →
  {"u values (mm)", "Maximum Deviation of Differences (mm)"}, LabelStyle → Medium]

ptConfidenceLimitsPlus = Transpose[{datafixedz[[All, 1]],
   10 datafixedz[[All, 2]] + 1.96 * 10 datafixedz[[All, 3]] / Sqrt[12 000]}]
ptConfidenceLimitsMinus = Transpose[{datafixedz[[All, 1]],
   10 datafixedz[[All, 2]] - 1.96 * 10 datafixedz[[All, 3]] / Sqrt[12 000]}]

ListPlot[{ptMean, ptStDev, ptConfidenceLimitsPlus, ptConfidenceLimitsMinus}, Frame → True,
 Axes → False, Joined → True, PlotStyle → {Automatic, Automatic, Dashed, Dashed}, FrameLabel →
  {"u values (mm)", "Mean and Standard Deviation of MLP (mm)"}, LabelStyle → Medium]

f = Interpolation[ptStDev]
NMaximize[{f[x], 0 ≤ x ≤ 200}, x]

g = Interpolation[ptConfidenceLimitsPlus]
NMaximize[{g[x], 0 ≤ x ≤ 200}, x]
```

```
gMinus = Interpolation[ptConfidenceLimitsMinus]
NMinimize[{gMinus[x], 0 ≤ x ≤ 200}, x]

diff1 = (ptConfidenceLimitsPlus - ptMean)[[All, 2]]

Max[diff1]

diff2 = (ptMean - ptConfidenceLimitsMinus)
Max[diff2]
```

APPENDIX E

AN EXAMPLE MATHEMATICA CODE FOR THE LATERAL, ANGULAR, AND ENERGY DISTRIBUTION FOR HOMOGENEOUS WATER PHANTOM

```
Clear["Global`*"]
Needs["Histograms`"]
(* ReadList [
 "c:/g4work/InhomogeneousMLP/OutputData/InternalPath_20thou_20cmcube@150_Fan_homogeneous
   _water_39.txt", Number,RecordLists→ True] *)
data = ReadList [
   "c:\g4work\InhomogeneousMLP\OutputData\EntryAndExit_20thou_20cmcube@150_Fan_homogeneous
     _water_39.txt", Number, RecordLists → True];
traj = ReadList [
   "c:\g4work\InhomogeneousMLP\OutputData\InternalPath_20thou_20cmcube@150_Fan_homogeneous
     _water_39.txt", Number, RecordLists → True];
protons = Partition[traj, 39];
Length[protons]
Gauss = (200 * Tan[data[[All, 2]]] + data[[All, 1]]) - data[[All, 3]];
data[[1]]
data[[-1]]
col[i_] := data[[All, i]];
Table[Histogram[col[i]], {i, 1, 5}]
Histogram[col[1], HistogramRange → Automatic, Frame → True,
 FrameLabel → {"Entry Lateral (mm)", "Number of Protons"}, LabelStyle → Medium]

Histogram[col[2], HistogramRange → Automatic, Frame → True,
 FrameLabel → {"Entry Direction (rads)", "Number of Protons"}, LabelStyle → Medium]
Histogram[col[3], HistogramRange → Automatic, Frame → True,
 FrameLabel → {"Exit Lateral (mm)", "Number of Protons"}, LabelStyle → Medium]
Histogram[col[4], HistogramRange → Automatic, Frame → True,
 FrameLabel → {"Exit Direction (rads)", "Number of Protons"}, LabelStyle → Medium]
Histogram[col[5], HistogramRange → Automatic, Frame → True,
 FrameLabel → {"Exit Kinetic Energy (MeV)", "Number of Protons"}, LabelStyle → Medium]
Histogram[col[3] - col[1], HistogramRange → {-30, 30}, Frame → True, FrameLabel →
  {"Difference of Exit and Entry Laterals (mm)", "Number of Protons"}, LabelStyle → Medium]
Histogram[col[4] - col[2], HistogramRange → {-0.2, 0.2}, Frame → True,
 FrameLabel → {"Difference of Exit and Entry Directions (rads)", "Number of Protons"},
 LabelStyle → Medium]
Histogram[Gauss, HistogramRange → {-20, 20}, Frame → True,
 FrameLabel → {"Difference of the Projected Exit Laterals and Actual Exit Laterals (mm)",
   "Number of Protons"}, LabelStyle → Medium]
Table[Sort[col[i]][[{1, -1}]], {i, 1, 5}] // MatrixForm
protons[[1, All]]
z = protons[[1, All, 1]]
x[i_Integer] := protons[[i, All, 2]]
allpt = Table[Transpose[{z, x[i]}], {i, 1, Length[protons]}];
ListPlot[Take[allpt, 1000], PlotJoined → True, Frame → True, Axes → False]
```